# Surface Photochemistry
of
Physisorbed Molecules

Hans G. Jenniskens

Surface Photochemistry
of
Physisorbed Molecules

Academisch Proefschrift

ter verkrijging van de graad van doctor aan de Universiteit van Amsterdam,
op gezag van de Rector Magnificus prof. dr. J. J. M. Franse,
ten overstaan van een door het college van dekanen ingestelde commissie
in het openbaar te verdedigen in de Aula der Universiteit
op woensdag 19 november 1997 te 13.00 uur

door

Hans Gerard Jenniskens

geboren te Best

Promotiecommisie

Promotor   Prof. dr. A. W. Kleyn

Overige leden   Prof. dr. M. Glasbeek
                  Prof. dr. A. Lagendijk
                  Prof. dr. S. Stolte
                  Prof. dr. M. J. A. de Voigt
                  Prof. dr. J. T. M. Walraven
                  Prof. dr. W. J. van der Zande

To Natasha

This thesis is based upon the following papers:

Contents

Chapter 1

Introduction

1.1 General introduction

The field of surface photochemistry is concerned with the chemical modification of molecules at surfaces. This includes for example desorption from the surface (breaking of molecule-surface bond), isomerization (activated rotation of a bond) and of course dissociation. The modification of matter by light plays an important role in our world. The chip fabrication and material processing industries heavily rely on the modification of matter by light. Some of the techniques used in these industries have a clear surface photochemical basis. A variety of processes in nature are also driven by the interaction with light. Photosynthesis and atmospheric photochemistry are two well know examples. A very nice example of the application of surface photochemistry is the use of TiO_2 films[1]. These films can photooxidize considerable amounts of organic material when exposed to normal daylight. A Japanese company produces ceramic tiles with a TiO_2 coating for hospitals and bathrooms. The UV light of fluorescent strip lighting is already sufficient to photocatalytically clean the tiles from organic contamination. Also self-cleaning paints and windows on the basis of TiO_2 are now being developed around the world[1,2].

Reactions at surfaces (without the presence of light) are very common. In industry, heterogeneous catalysis is used to transform large amounts of chemical compounds via surface reactions into a desired product. Corrosion of metals also proceeds via a surface reaction and the car catalysts only works because of surface reactions. Even in atmospheric chemistry surface reactions are present. Polar stratospheric clouds are known to have a destructive effect on the thickness of the ozone layer. Surface photochemical reactions on ice crystals are believed to be the cause of this effect.

That surfaces play an important role in chemistry is due to several reasons. First, surfaces can lower reaction barriers and therefore enhance reaction rates. The energy needed to overcome a reaction barrier is supplied from the thermal energy of the substrate. Secondly, depending on what kind of substrate is used, certain chemical intermediates are stabilized by the substrate and control of the direction of the reaction is obtained. In the oxidation of methanol (CH_3OH),

a silver substrate is known to partially oxidize the methanol to formaldehyde (CH_2O)[3–5], whereas platinum oxidized the methanol to CO and H_2[6].

In surface photochemistry the energy needed to overcome the reaction barrier is supplied by the photon. In principle, this allows one to put energy into a specific bond by tuning the wavelength without putting energy in other bonds. This is in contrast to thermal surface reactions where all bonds experience the same amount of thermal activation. This feature is especially important for the semiconductor industry where the trend to smaller dimensions dictates the necessity to work at lower temperature. Another major advantage of the use of photons is the ability to obtain lateral resolution in the order of the wavelength. In this way patterns with sub-micron resolution can easily be made. Fundamental research also benefits from surface photochemistry. By using femtosecond lasers the start of a reaction can be controlled in time and therefore the time evolution can be monitored. For gas phase reactions this is already shown[7] and for surface reactions this research is in progress[8]. The combination of light and surfaces also opens the way for novel spectroscopic techniques that allow us to investigate the molecule-surface interaction in much more detail.

1.2 Principles of surface photochemistry

Several mechanisms are conceivable along which a photochemical reaction at a surface might proceed[9–11]. The three most common experimentally observed mechanisms are: thermal, direct excitation and substrate mediated. First, we will introduce these three mechanisms in terms of a simplified scheme. Subsequently, the later two mechanisms will be dealt with in more detail.

In figure 1.1 is shown schematically how these three processes can induce desorption or dissociation of a molecule. The molecule is denoted by AB, where A and B can be either a atom or part of a molecule. So, B can be nitrogen in the case of NO or CH_3 in the case of methyl chloride (CH_3Cl). In the thermal mechanism photons are absorbed by the substrate or molecule and transferred into heat. This causes an elevation of the substrate temperature and thermal desorption or dissociation can occur. In this case the photons are used as a source of heat and have the advantage over conventional substrate heating that some degree of lateral resolution can be obtained. In a direct excitation process the photon is absorbed by the adsorbate. This causes the adsorbate to be electronically excited (AB^*). This excess energy can be used for desorption or dissociation. In the substrate mediated mechanism the photon is absorbed by the substrate and excitation of an electron near the Fermi level of the substrate to the adsorbate occurs. Since the lifetime of negative ion states near the substrate is short, rapid deexcitation will occur. After deexcitation still some energy is retained in the molecule which can be used for desorption or dissociation.

After this schematic picture of the possible photochemical mechanisms, the direct and the substrate mediated mechanism will be explained in more detail. In this explanation we will concentrate on the time scales and energetics. In
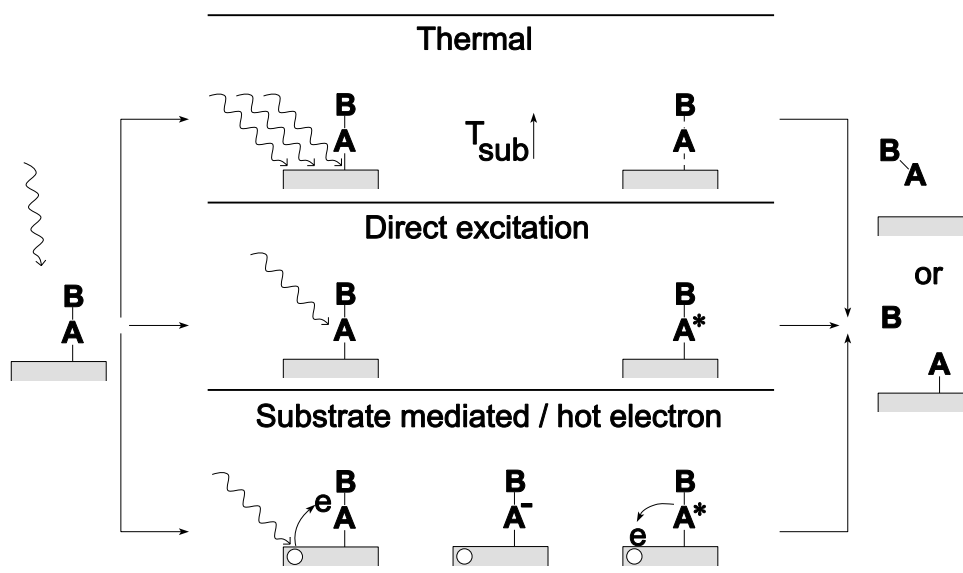
Figure 1.1: *Schematic representation of three commonly observed photochemical mechanisms. On the left an adsorbate is depicted that via the three depicted mechanisms is able to desorb or dissociate.*

figure 1.2 the energy diagram of a direct photochemical process is given. The figure contains a ground state and an excited state potential energy curve as a function of the so-called reaction coordinate. The reaction coordinate is a space coordinate along which the reaction occurs, i.e. for desorption the reaction coordinate can be seen as the molecule-surface distance and for dissociation this is the distance between the two dissociation products. The reaction coordinates for these two situations are pictured in figure 1.2 as well. In practice the reaction coordinate will be a multi-dimensional variable, for instance a combination of distance to the surface and angle of the molecule with the surface. The ground state exhibits a well close to the surface, which causes bonding of the molecule to the surface. The adsorption of a photon by the molecule results in a Franck-Condon electronic transition to an excited state. In this example the excited state is assumed to be repulsive, but this is not essential. Because of the gradient of the excited state, the molecule will move along the reaction coordinate gaining kinetic energy. After some time the excitation will be quenched by the substrate and a transition to the ground state occurs. If the kinetic energy obtained in the excited state is larger then the remaining potential energy towards a reaction coordinate of infinity, photochemical dissociation/desorption occurs. The deexcitation of the excited state is a statistical process and the probability for a photochemical event depends critically on the excited state lifetime. Also the exact shapes of the excited and ground state influence the photochemical probability to a large
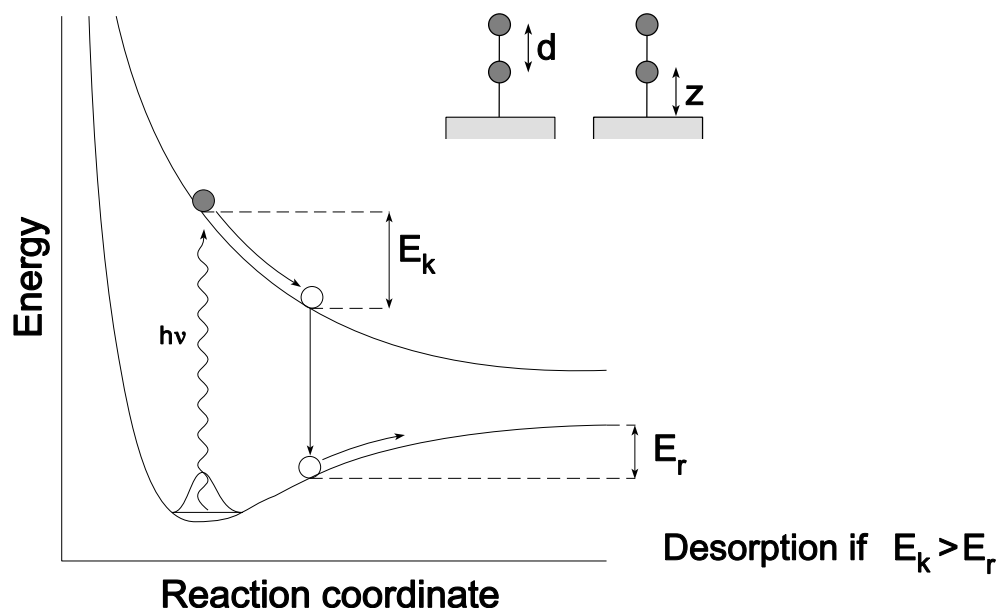
Figure 1.2: *Energy diagram of a direct excitation process. If the kinetic energy gained on the upper curve, E_k, is larger than the energy remaining towards desorption/dissociation, E_r, a photochemical event will take place.*

extend. The lifetimes are expected to be in the subpicosecond region.

For the substrate-mediated mechanism a similar picture applies, although the initial excitation is more complex. In figure 1.3 on the left side the initial excitation to the negative ion state is depicted and on the right side the subsequent nuclear motion is shown. The initial excitation is depicted in terms of an energy diagram of the adsorbate-metal complex. The electron distribution in the metal is represented by rectangles on the left and the adsorbate by the schematic Coulomb potential. The conduction band of the metal is filled up to the Fermi level. Absorption of a photon by the substrate causes excitation of a conduction band electron above the Fermi level to a surface bound unoccupied state. Because of electron-electron scattering in the metal the energy will be distributed over several electrons and a hot secondary electron distribution is obtained. The electron-electron scattering processes occur on a 10 fs time scale. On a picosecond timescale the hot electrons will transfer their energy to phonons in the substrate. Because of the generation of these hot electrons this mechanism is also referred to as hot electron mediated. Excitation of the adsorbate proceeds via the attachment of a hot electron via tunnelling into an affinity level. This excitation into a negative ion state is depicted by the straight arrow from the ground state to the excited state in the right part of figure 1.3. After this excitation into the negative ion state a process similar as in the direct excitation mechanism proceeds. Due
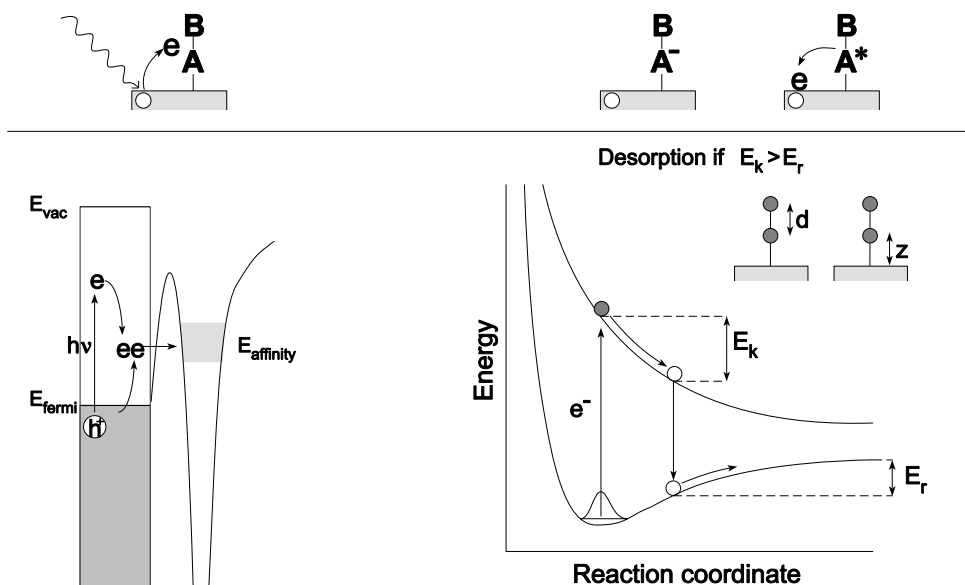
Figure 1.3: *Energy diagram of a substrate mediated excitation. On the left the substrate-adsorbate complex is depicted and on the right the nuclear motion after excitation of the adsorbate is shown.*

to the curvature of the upper state motion of the molecule will occur. If after quenching of the excited state enough kinetic energy is obtained in the excited state, dissociation/desorption will occur. The lifetime of the negative ion state is typically in the order of 1–10 fs. Because this lifetime is very short, only a minute fraction of the excited molecules will actually undergo a photochemical event. That the cross section for substrate mediated photochemistry is still appreciable compared to direct excitation is due to the high absorption of the metal (typically larger than 25%) relative to the absorption of an adsorbed molecule.

As an excited state in figure 1.2 and 1.3 a repulsive potential is pictured without any well. Therefore such an upper state is called a direct dissociative state. Dissociation via tunneling from a bonding part of the excited state to the repulsive part is referred to as a predissociative mechanism. This mechanism is depicted in figure 1.4. An excited state with stronger bonding character can also result in a photochemical event (also shown in figure 1.4). After deexcitation, the molecule can return on the highly repulsive part of the ground state above the dissociation/desorption barrier.

Several differences exist between the direct excitation and substrate-mediated mechanism. In the direct excitation the absorbed photon has to match the energy difference of the two levels. Due to level broadening by the substrate the resonance will be less sharp compared to the gas phase and may be shifted as well due to substrate interactions. In a substrate mediated mechanism no reso-
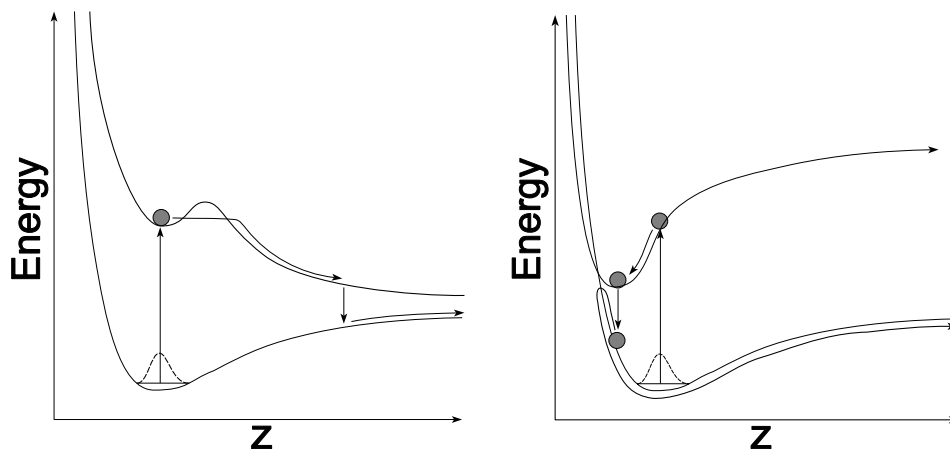
Figure 1.4: *Other excited states that can lead to desorption or dissociation. On the left a predissociative potential is plotted. If an excited molecule in the well tunnels through the barrier before it is deexcited, desorption or dissociation can take place. On the right a stronger bonding excited state is depicted. After deexcitation, the molecule can return on the repulsive part of the ground state and again a desorption or dissociation event can take place.*

nance exists. Due to the electron-electron scattering, an increase of the photon energy will result in more and hotter secondary electrons. This yields a higher excitation probability and therefore a higher dissociation/desorption cross section with increasing photon energy. Another difference is the nature of the excited state. In the direct excitation the electronically excited state is neutral and in the substrate-mediated process the excited state is negatively charged.

1.3   This thesis

This thesis is concerned with the interaction between adsorbed molecules and visible and UV photons. Because no suitable instrument was available in the institute to study this interaction, a new ultra-high vacuum (UHV) apparatus was designed. **Chapter 2** describes this system that is able to study the interaction between photons and adsorbates in general. The unique features of the apparatus are: storage of three crystals in the vacuum, liquid nitrogen cooled sample that can be exchanged under UHV conditions, variety of analytical tools among which infrared spectroscopy and a high-pressure cell that allows for dosing and experiments into the mbar pressure range. In this chapter also some result are shown to illustrate the capabilities of the apparatus.

   Chapter 3 reports the adsorption of methanol on the (111) face of silver. Both the monolayer and multilayer regimes are explored. This adsorption study served both as a test case for the newly build system and as an introduction for

a photochemical study on methanol adsorbed on Ag(111). Using thermal desorption spectroscopy (TDS) two different crystallographic phases could be distinguished in the multilayer adsorption regime for the first time. When experiments showed that methanol on Ag(111) exhibited no photochemistry at wavelengths longer than 266 nm, even not for intensities exceeding $1 \, \mathrm{GWcm}^{-1}$, research moved on to the alkyl nitrites (RONO).

In **chapter 4** the adsorption behavior of tert-butyl nitrite, $(CH_3)_3CONO$, on Ag(111) is examined. The adsorption is studied with both thermal desorption spectroscopy (TDS) and X-ray photoelectron spectroscopy (XPS). The findings are typical for a physisorbed molecule on a non-reactive substrate. This study forms the basis of the photochemical study reported in chapter 5 and 6.

Chapter 5 is concerned with the photochemistry of tert-butyl nitrite on Ag(111) at 355 nm. This wavelength is chosen because at this wavelength in the gas phase photodissociation occurs via a predissociative state. We were interested if dissociation on a metal substrate would occur and whether the same mechanism as in the gas phase would apply. While exploring the photochemistry of tert-butyl nitrite at this wavelength, several interesting phenomena were observed, such as thermalization of photoproducts and caging due to surrounding molecules.

In **chapter 6** the surface photochemistry of tert-butyl nitrite is explored at other wavelengths (532 and 266 nm). At both wavelengths dissociation of the molecule is found and thermalization of NO photoproducts and caging was present as well. Especially the existence of dissociation at 532 nm is interesting, since at this wavelength dissociation is believed to be absent in the gas phase.

Chapter 2

An ultra-high vacuum (UHV) apparatus to study the interaction between adsorbates and photons

Abstract   *An UHV apparatus has been designed and constructed for studying the interaction between adsorbates and photons. Since a variety of light sources and experimental geometries will be used in these studies, the system was designed to be as flexible as possible. The system is put on a single frame so that it can be transported from one photon source to another. A compact, exchangeable, high-pressure cell is designed to provide easy access for photons to the crystal. To allow the study of small polyatomics the following combination of detection techniques are installed: thermal desorption spectroscopy (TDS), X-ray photoelectron spectroscopy (XPS), Auger electron spectroscopy (AES), low energy electron diffraction (LEED) and reflection adsorption infrared spectroscopy (RAIRS). Furthermore a sample exchange system in combination with liquid nitrogen sample cooling is incorporated. The exchange system allows for the storage of three samples in the main chamber. The sample exchange capability does not restrict the cooling capabilities, 85 K within an hour after turning on the liquid nitrogen flow and 85 K within minutes after flashing to 800 K.*

2.1   Introduction

The interaction of light with adsorbates on single crystal surfaces in UHV has gained a lot of interest over the last decade[10–13]. This interest is both from a fundamental as from a applicational point of view. The fundamental interest

is driven by the desire to understand chemical and photochemical reactions on surfaces in more detail. Since chemical reactions take place on a very short time scale (typically 100 fs or less) fast detection techniques are needed to observe the reaction in real time. This makes femtosecond lasers the ideal tool to investigate the reaction on a real time basis. For gas phase molecules it has been shown that it is possible to observe a reaction in real time[7]. For adsorbates this has not yet been demonstrated. However, the first step of an adsorbate reaction, the electronic excitation of the substrate, can now be monitored in real time[8].

Another advantage of the use of light to initiate chemical reactions is that photons provide energy for the reaction in a non-thermal way. This allows for the study of reactions that have large activation energies. And by changing the wavelength it is possible to selectively excite a certain molecular state in order to control the reaction path. Furthermore spectroscopy and more specific non-linear spectroscopy can give very valuable information about the adsorbates, because of its surface sensitivity. Photochemical reactions on surfaces are also studied because they can be applied in material processing steps like photoetching and metal deposition.

From the paragraphs above it is clear that photons can both probe and invoke surface reactions. These photons can be UV photons but also visible, infrared or X-ray photons. Furthermore the light source can be a lamp, laser, free electron laser or synchrotron. Because of this variety of sources and experiments it is necessary to have a flexible UHV machine to study the interaction of light with adsorbates. In the literature several brief descriptions can be found of UHV systems with which surface photochemical experiments are conducted[14–19]. Most of these systems are standard large radius UHV machines with the following detection techniques: low energy electron diffraction (LEED), Auger electron spectroscopy (AES), thermal programmed desorption (TPD). Only occasionally time of flight (TOF) is used and the use of vibrational sensitive detection techniques like electron energy loss spectroscopy (EELS) and reflection absorption infrared spectroscopy (RAIRS) is even more rare.

In the next section the choice of the design of a flexible UHV apparatus will be discussed. In section 2.3 the system will be described in detail. In the section 2.4 some results on the surface photochemistry of tert-butyl nitrite, $(CH_3)_3CONO$, will be shown to illustrate the capabilities of the apparatus.

2.2   Choice of design

In order to design a flexible UHV apparatus the following design criteria were formulated.

1. The system should be transportable so different photon sources can be used.

2. A exchangeable UHV compatible cell should be mounted on the system. This cell should both be used for high-pressure dosing and for irradiating the crystal with photons. The high-pressure dosing system extends the

number adsorbates that can be studied and the exchangeability of the cell allows for easy switching of the experimental geometry. The cell should be designed in such a way that experiments can both be performed at UHV and at high-pressures

3. It should hold enough surface analytical tools to analyze adsorbed, small polyatomics molecules.

4. It should be possible to change crystals without breaking the vacuum. This demand guarantees that more experiments can be performed in the same period without breaking the vacuum. It also allows the use of an alignment tool in the vacuum, such as a pinhole or doubling crystal.

5. Because most polyatomics molecules do not stick at room temperature, sample cooling was an other demand. We have chosen to use liquid nitrogen cooling because this gives sufficient low temperatures to stick most polyatomics.

6. And finally, the viewports on the vacuum system had to be on laser table optics height (approximately 1 m above floor level) for easy access of laser light.

In the following paragraphs the design of the system will be discussed. First the system size and shape will be described. Subsequently the choice of the analytical tools will be explained. And finally the crystal cooling, changing and manipulation will be reported.

The machine should be UHV compatible to keep the surface free of contaminants during the experiment. The UHV system is designed as a cylinder with the axis in the horizontal plane. This shape enabled us to accommodate several analytical tools on the system (demand 3) while still keeping two dimension (width and height) of the system small. The necessity to keep these dimensions small was given by the demand of transportability (demand 1). In this way the system could be moved through doors and in a truck or train. Another advantage of this shape is that all viewports can easily be mounted at laser table optics height. The vacuum system with most of the electronics is put on one single frame with wheels for convenient transportation.

In order to meet the exchangeability of requirement 2, the high-pressure cell is bolted to one end of the cylindrical vessel instead of welded. Thus the cell can be replaced easily by another if a new experiment would dictate this. The cell is equipped with several viewports sealed by copper gaskets. We have refrained from the use of differentially pumped windows in order to keep the cell compact and easily exchangeable. By keeping the cell compact, the distance between the crystal and the viewport is very small (approximately 6 cm). The advantage of a compact cell is twofold. First, the solid angle of the viewports as is seen by the crystal is very large, which allows for a wider range of incidence angles and thus experimental geometries. This is particularly useful for sum frequency generation (SFG). The second advantage is that light can be focused better onto

the crystal since the focal distance is small. For high-pressure dosing in the cell a construction similar to the cell of Yamada et al.[20] is chosen, rather than the construction already available at our laboratory[21,22]. A separate high-pressure cell (like the one used by Raval et al.[23]) is not chosen since the sample cannot be transferred to this cell with the cooling on . The present design allows for a better accessibility of the crystal for photons during high-pressure dosing and there is no need to transfer the crystal. The details of its design will be discussed later on.

To identify the adsorbed species a combination of surface characterization tools is needed as one technique will only provide a limited amount of information. Thermal desorption spectroscopy (TDS) is a good tool to determine the mass of desorbing molecules, but will not show if a molecule is dissociated upon adsorption or during heating the sample. Furthermore, if the masses monitored in TDS are different from the mass of the desorbing molecule, the desorption process is not detected in TDS. So generally it will take some trial TDS runs to determine the masses of all the desorbing molecules. Secondary ion mass spectroscopy (SIMS) does not require heating of the substrate, but the technique is still destructive. Other techniques, like Auger electron spectroscopy (AES) or X-ray photo-electron spectroscopy (XPS), do generally not suffer from these two problems (invisibility and destruction of the adsorbate). The disadvantage of these techniques is that they are not sensitive for hydrogen, so they will generally not show the difference between for instance adsorbed CO, CH_2O, CH_3O and CH_3OH. In discriminating between the species mentioned above, XPS performs better than AES because of the shifts of photoelectron peaks due to different chemical environments (the so-called chemical shift). To be sensitive to hydrogen and to be non-destructive a vibrational sensitive technique should be used like reflection absorption infrared spectroscopy (RAIRS) or electron energy loss spectroscopy (EELS). But the vibrational spectra obtained by these techniques are usually difficult to interpret, because certain vibrations may not be visible in the spectra due to the dipole selection rules at metal surfaces or due to unexpected shifts or appearances of vibrational modes.

Taking into account the considerations made above, we have chosen for the following combination: TDS, XPS, AES and RAIRS. TDS to study the masses and adsorption/desorption energetics of the adsorbates, XPS and AES for the elemental composition of the overlayer and RAIRS for the vibrational information. Because a mass spectrometer is very useful for residual gas analysis and time of flight (TOF) measurements, the choice for TDS is very obvious. XPS will show all elements present on the surface, it is quantitative and due to the chemical shifts of peaks it yields a limited amount of chemical information. Generally it has a good signal to noise ratio but has a poor sensitivity for elements with small masses. AES is easy to combine with XPS because it only requires an additional electron gun. RAIRS will show the vibrational structure of the adsorbate and, in combination with XPS, allows for identification of the adsorbate. The advantage of RAIRS over EELS is that RAIRS put less constraints on the vacuum system and that the resolution is better. RAIRS is also capable in measuring adsorbates

surrounded by an ambient gas, where EELS is restricted to UHV conditions.

The fourth demand concerned the possibility to change the crystal without breaking the vacuum of the UHV chamber. One possibility would be to mount a sample exchange chamber. Such a chamber should be separated from the main chamber by a valve so it can be vented independent of the main chamber to insert samples. Samples should be transferred through this valve to the main chamber. This option requires a separate chamber, turbo pump, valve and a exchange mechanism, which all occupy a significant amount of space on the system. Because of the transportability requirement this space is limited, however we have chosen for another solution: three crystals can be mounted in the main chamber and can be inserted in the target head when required. This exchange system must be combined with a cooling system as was one of the demands. The details of this combination will be described in the next section.

2.3   Description of the UHV system

In figure 2.1 a schematic overview of the system is shown with all the components. At the left the manipulator is drawn and at the right the high-pressure/infrared cell is depicted. The mid part is the vacuum vessel with the different components.

The UHV system and most of the electronics are put on one single frame with wheels. This frame measures 1 by 3.5 m long and 1.7 m high. The lower part of the frame is used for the electronics. The axis of the vacuum system is at laser table optics height (approximately 1 m). The space above the vacuum vessel is used for mounting large components like the electron energy analyzer and the infrared spectrometer. Figure 2.2 shows the positioning of the vessel and electronics on the frame.

The two PCs that control the experiment are not put on the frame for ergonomic reasons. Apart from the PCs also one rack of electronics is not mounted on the frame because it did not fit on the frame. This rack is also on wheels and has very few connections to its environment allowing easy transport.

The base pressure of the system should be in the order of the 10^{-10} mbar. To this end a Balzers TPU 450H turbo-drag pump in combination with a Balzers MD4TC diaphragm pump is mounted. The turbo-drag pump has a capacity of 450 ls^{-1}. Both the turbo-drag and the diaphragm pump are halogen proof versions. The system is also equipped with a titanium sublimation pump (Balzers USP 035). A second turbo-drag pump from Balzers (TPU 180H) is used for pumping the high-pressure cell during high-pressure dosing. This pump is backed by the same diaphragm pump as the big turbo-drag pump (the TPU 450H). The small turbo-drag pump is also used to pump the dosing line and is chemical resistant as well. The main turbo can be sealed from the vessel by a pneumatically actuated valve (VAT SVV-160-PF) and the smaller turbo can be sealed from the vacuum by a manually actuated all metal valve (VG CR97). The rotational feedthrough of the manipulator is differentially pumped using a drag pump (Balzers TPD020) backed with a diaphragm pump (Balzers MD4T).
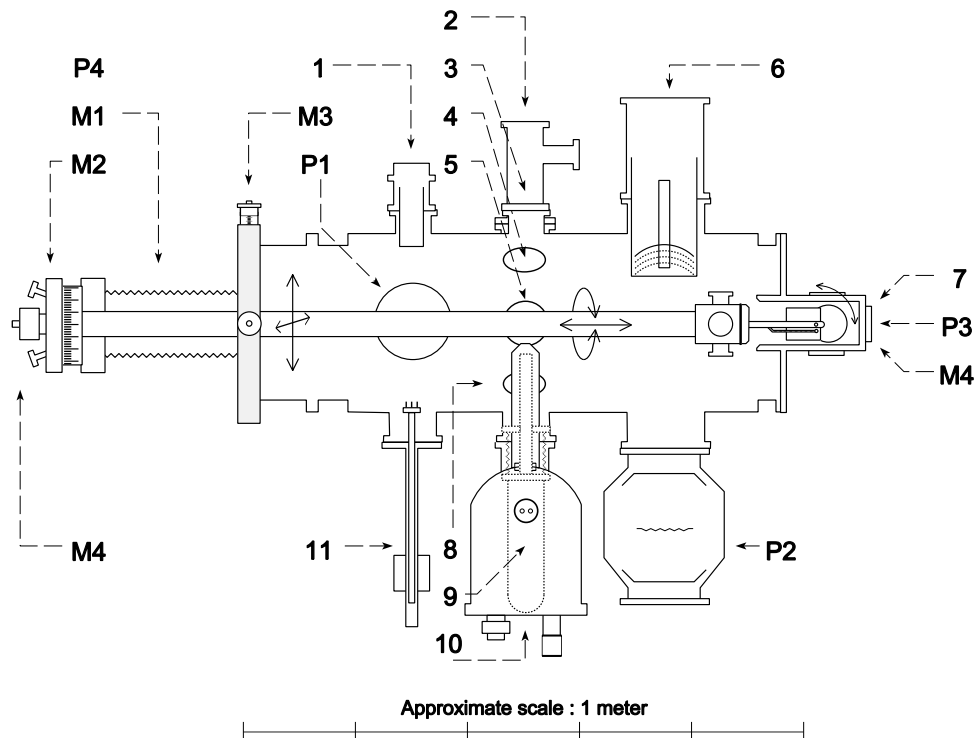
Figure 2.1: *Schematic top view of the system. The circles in the vessel denote the vacuum ports located at the bottom part. The following components are indicated in the figure. P1: main turbo-drag pump, P2: Titanium sublimation pump, P3: turbo-drag for high-pressure dosing, P4: drag pump (not drawn) for differential pumping of rotational feedthrough, M1: manipulator translation stage (only bellow is shown), M2: rotational feedthrough for 360° rotation of sample, M3: x-y translation stage, M4: linear motion drive for tilting the crystal, 1: sputter gun, 2: Quadrupole mass spectrometer, 3+4: UV grade fused quarts viewport, 5: halogen lamp on feedthrough flange, 6: LEED, 7: high-pressure/infrared cell 8: ionization pressure gauge, 9: X-ray source, 10: electron energy analyzer, 11: magnetic rod for crystal exchange*
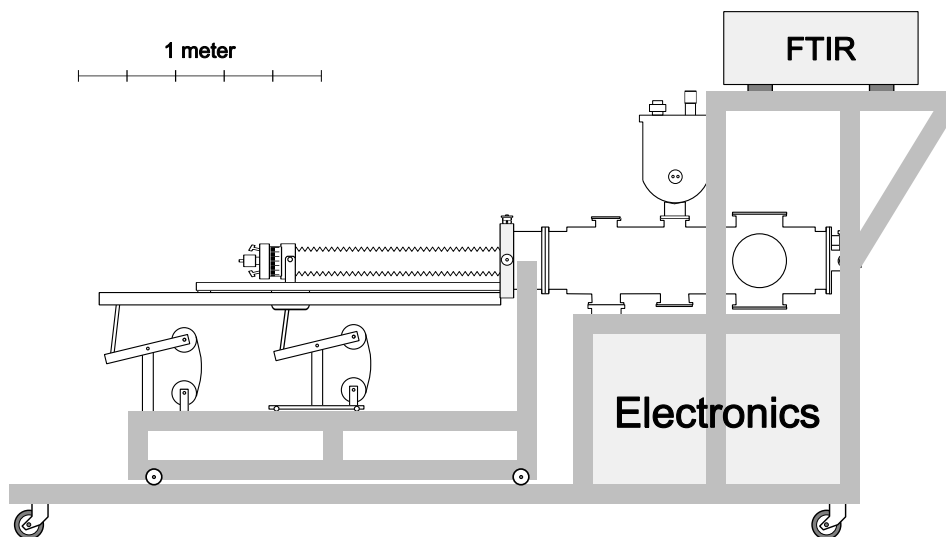
Figure 2.2: *Drawing of the system showing the positioning of the vessel, manipulator, hemispherical electron energy analyzer, Fourier transform infrared (FTIR) spectrometer and electronics. On the right side part of the high-pressure/infrared cell can be seen. The complete system is mounted on a frame with wheels for easy transportation.*

Residual gas analysis and TDS is performed with a Balzers 420 quadrupole mass spectrometer (QMS), which can measure masses up to 200 AMU. The mass spectrometer has a faraday cup and a 90° off axis channeltron. A crossbeam ionizer is used to ionize the molecules. This mass spectrometer is also used for time of flight (TOF) measurements. In that case the Balzers pre-amplifier is replaced by a fast current amplifier to magnify the pulses from the channeltron. These magnified pulses are subsequently height selected by a discriminator and fed to a multi-channel scaler (MCS) from EG&G (Turbo MCS), which has a 5 ns resolution.

To irradiate the crystal with photons during TOF measurements, two UV grade fuse quarts viewports are mounted under and above the QMS port (figure 2.1). The incident light impinges at an angle of 52.5° with respect to the surface normal and the desorbing molecules are detected almost along the surface normal (7.5° with respect to the surface normal). If the angle of incidence is varied for a particular experiment, the laser beam that reflects from the crystal will hit the inside wall of the vessel and will not exit the vessel through a viewport. In this situation much care should be taken to ensure that the measured TOF signal is not due to molecules desorbing from the chamber wall. The QMS can be mounted on the high-pressure cell if an experiment over a complete range of angles of incidence should be performed. Due to the compactness of the cell a

range of angles of incidence can obtained.

The XPS equipment is supplied by VG and consists of a twin anode XR3E2 X-ray source and a Clam2 hemispherical electron energy analyzer. The X-ray source is capable of producing both Al and Mg K_α radiation and it is mounted on a 75 mm translation stage (VG, ZLTM 75) to move the source in front of the crystal. The analyzer is usually operated at a pass energy of 20 eV, was calibrated to the Silver $3d_{5/3}$ line at 367.9 eV and measured a width of 1.1 eV when operated at 20 eV pass energy.

To obtain a surface free of contaminants at the start of an experiment, a Riber CI-10 sputter gun is used. A VG RV900 rear view low energy electron diffraction (LEED) apparatus with home build electronics is used to study the surface and overlayer structure. A halogen lamp on a feedthrough flange is mounted to illuminate the interior of the vessel. Dosing is performed by means of a VG all metal valve (MD6) at the high-pressure cell end. This way of dosing is both used for low and high-pressure dosing. A Balzers hot cathode ionization pressure gauge (IMR132) is used for measuring the pressure.

The crystal is exposed to the gas via backfilling the chamber during typically a few minutes. During dosing the QMS is set to measure the partial pressure of this gas as a function of time. This trace is integrated over time and converted to an exposure expressed in mbar s by calibration of the QMS against the pressure gauge. The advantage of this procedure is that the dose is corrected for variations in pressure during dosing. In addition it takes into account the exposure during opening and closing of the valve.

During bake out the system is heated by means of silicon heating foils (Watlow 110-240V). The overall baking temperature is maintained at an average temperature of 150 °C by Clickson temperature switches (RS, 150 deg C/NC). However, near the heating foils the baking temperature may be up to 200 °C.

A large manipulator can be seen in figure 2.1. The degrees of freedom of the manipulator are schematically drawn. This manipulator is able to translate the sample along the axis of the cylindrical vessel (z-axis) over a distance of 80 cm (VG Omniax MX800). The sample is connected to the Omniax by a long rod as depicted in figure 2.1. The manipulator allows for a 360° rotation around the axis of the vessel by a rotational feedthrough (VG DPRF 55) mounted behind the Omniax. These two movements are motorized by DC motors from Maxon with incremental encoders to ensure high accuracy and reproducibility. The two motors can be controlled manually or by computer. When they are controlled by the computer a home written program controls the movement to a user defined position while taking care that the manipulator does not hit any of the equipment inside the vacuum. This is achieved by the definition of forbidden areas in the two dimensional space set up by the translation and rotation.

Furthermore, the manipulator is equipped with the possibility to translate the sample perpendicular to the z-axis in two directions (x and y direction). The translation range is 2.5 cm and is used for the final adjustment of the crystal position. This translation stage from VG is mounted in between the Omniax and the vacuum system. Because of the xy-translation stage the support of the
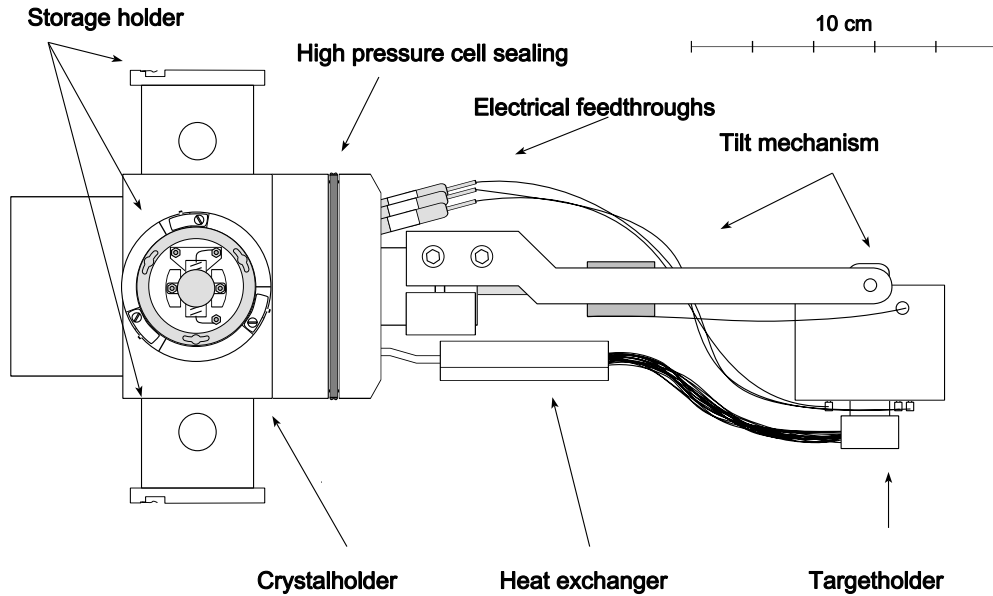
Figure 2.3: *Target side of the manipulator rod. On the left side the end of the rod can be seen. On the left side as well, the three storage holders with a crystal holder (top view) is depicted. On the right side the target holder in tilted position is shown. By actuating the linear transfer mechanism (not drawn) at the back of the manipulator, the tilt mechanism is retracted. This retraction in combination with the excentrically placed joint (marked by right arrow of tilt mechanism) causes the crystal to tilt back.*

manipulator had to allow for some movement. The manipulator is therefore supported by a spring construction where the force exerted by the springs is almost independent of the displacement. The support is depicted in figure 2.2. The last degree of freedom is a home built 90° tilt of the crystal away from the z-axis. This allows the crystal to face either the wall of the vessel or along the axis of the vessel. This degree of freedom is needed to enter the high-pressure cell. The tilt is actuated by a linear motion drive (VG LMD 25) at the end of the manipulator. A bar through the center of the manipulator rod transfers the translation to the target head where the translation is converted into a tilt. This tilting mechanism is schematically depicted in figure 2.3 and described in more detail elsewhere[24]. These five degrees of freedom allow flexible positioning of the crystal.

The system is equipped with a sample exchange system, which allows storage of the sample holders in the vacuum chamber. In total three crystals can be stored in the vacuum system. The storage holders are located on the manipulator rod directly behind the target head. This is depicted in figure 2.3 where the target head is shown with storage holders and part of the cooling system. The crystal holders can be transferred from the storage holders to the target head by means of
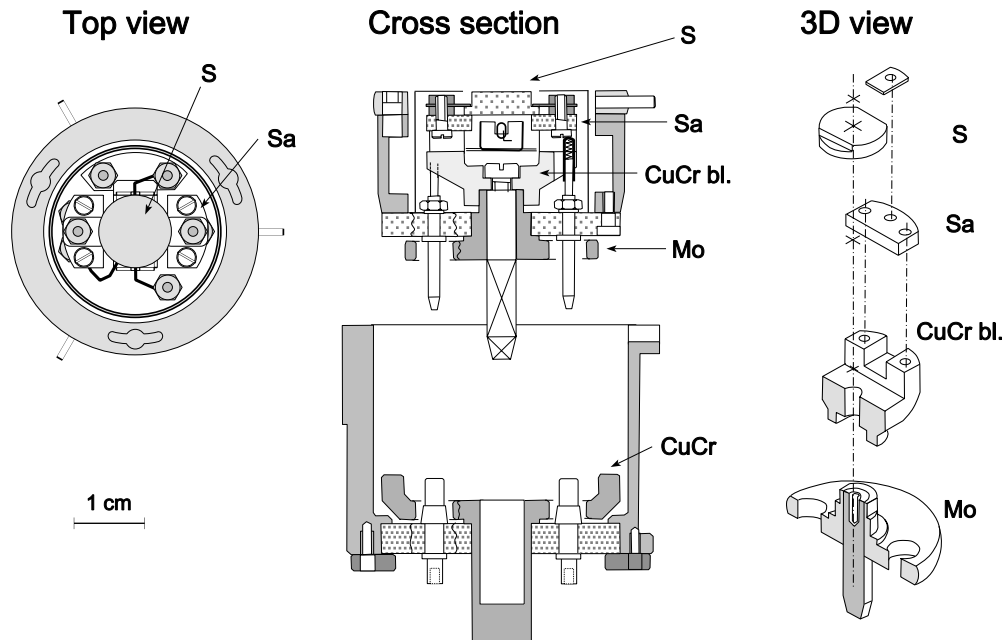
Figure 2.4: *Design of the crystal holder. Both top view, cross section and 3D view are depicted. 3D view shows the elements via which the sample (S) is cooled: sapphire (Sa), CuCr block (CuCr bl.) and Molybdenum disk (Mo). The top view shows the bayonet locking slots, filament, thermocouple and clamping of the crystal. The cross section shows both the crystal holder and the target head. The CuCr ring in the target head (CuCr) and Mo disk at the bottom of the crystal holder make a tight connection during cooling. The cross section also shows how electrical contact is made to the crystal holder by pins.*

a magnetically coupled transfer rod (VG MLRM03). This rod is equipped with a three-pin bayonet connection for locking to the crystal. To lock the crystal holders in the storage holder, the crystal holder is designed with three pins at the side of the holder, which lock under blade springs in the storage holder. The target head is equipped with the same locking mechanism. Both this locking mechanism and the bayonet slots can be seen in figure 2.3 and 2.4.

The exchange mechanism described above had to be combined with the crystal cooling. This required a loose connection when the crystal holder is removed from the target head and a tight connection during cooling. This is achieved by designing the crystal holder with a Molybdenum (Mo) base plate and the target holder with a CuCr ring. At room temperature the Mo base plate fits loosely into the CuCr ring, but if the CuCr ring is cooled the connection becomes tight because of the difference in thermal expansion coefficients of the two materials. The design can be viewed in figure 2.4. The Mo base plate is connected by a CuCr block to the sapphire support of the crystal. The sapphire is used to

electrically isolate the crystal from the holder. In this way the crystal current can be measured by connecting a wire to the clips by which the crystal is being clamped to the sapphire. The ability to measure a crystal current is very useful during alignment procedures for XPS, LEED and sputtering. Beside its isolating properties sapphire is also chosen because of its good thermal conductivity at low temperatures and its poor conductivity at high temperatures. In this way there is a good thermal contact during cooling and a good thermal isolation when the crystal is heated. The crystals used are cylindrical with a 10 mm diameter and a thickness of 3 mm. The crystal heating is achieved by a tungsten filament behind the crystal. To enhance the heating power a voltage of 400 V can be applied between the filament and the crystal causing electrons to be extracted from the hot filament and accelerated towards the crystal. In the side of the cylindrical crystal a little hole is made by spark erosion in which a Chromel Alumel thermocouple in a electrically isolated metal tube from Thermocoax is inserted. The total diameter measures only 0.5 mm. Due to the isolation the temperature of the crystal can be measured without making any electrical contact to it and therefore an accurate measurement of the crystal current can be performed. An Eurotherm 905S temperature controle unit regulates the temperature of the crystal by adjusting the current through the filament. This design necessitates a total of 5 electrical connections at the base plate of the crystal holder (two for the filament, two for the thermocouple and one for measuring the crystal current). These connections are made by pins and are connected to feedthroughs at the end of the manipulator where they exit the vacuum. The crystal holder design is described in somewhat more detail elsewhere[24].

After having described the crystal holder the remainder of figure 2.3 will be discussed now. The CuCr ring in which the Mo crystal holder base plate fits is connected by means of two flat copper braids to a liquid nitrogen heat exchanger. The braids allow for a tilt of the target head of 90° without loosing the ability to cool the sample. The copper braid is constructed with a copper block on each end. These copper blocks are clamped to the heat exchanger on one side and to the CuCr ring on the target head side. The braids themselves are electron-beam welded in these copper blocks to maximize the thermal contact. Through the copper heat exchanger a flow of liquid nitrogen is maintained. The liquid nitrogen is supplied to the heat exchanger via stainless steel tubes, which run from the back of the manipulator in the manipulator rod. To ensure a good heat exchange between the liquid nitrogen and the heat exchanger, the exchanger is filled with copper wires. This system is capable of cooling the crystal to 85 K within an hour after turning on the cooling and capable of cooling the crystal back to 85 K within minutes after flashing the crystal to 800 K. The crystal can be heated to at least 1250 K and maintain a heating rate of 15 K s^{-1} up to 800 K. This all demonstrates that due to the design exchangeability of the crystal holder can be very well be combined with good cooling and heating capabilities.

Figure 2.3 also shown how the sealing for high-pressure dosing is achieved. A quad viton ring between the target head and the storage holders seals the crystal from the rest of the vacuum system when it is inserted in the cylindrical high-

pressure cell. Insertion of the crystal in the high-pressure cell is simply performed by translating the manipulator along the z-axis with the crystal tilted towards the high-pressure cell and centered in front of the cell by the x-y translation stage. The sealing of the five electrical connections to the crystal holder are achieved by electrical feedthroughs. The bar, which transfers the motion for the tilting of the crystal, is sealed by viton. At this position also a bearing for the bar is mounted. The two tubes, by which the liquid nitrogen circulation through the heat exchanger is maintained, are sealed by welding. The liquid nitrogen feedthroughs are made in such a way that the thermal contact to the environment is minimal.

The high-pressure cell is also used for reflection adsorption infrared spectroscopy (RAIRS). Therefore the cell is equipped with two Zinc Selenide windows in between which the crystal can be positioned (figure 2.5). In this position the crystal is facing a third window which can be used for photochemistry experiments. The Zinc Selenide viewports are chosen for their commercial availability and for the absence of required differential pumping. This enables a simpler design and a easier exchangeability of the cell. The transmission range of the viewport is 0.6–20 μm, this correspond to 500–16666 cm^{-1}. The cell can be pumped by a turbodrag pump as described above. An all-metal valve connects the high-pressure cell to the main vessel and can be used to bleed gas from the high-pressure cell into the main chamber for gas analysis.

The RAIRS is performed with a Biorad FTS175 Fourier transform infrared (FTIR) spectrometer. The spectrometer is equipped with an air-cooled Permaglow high energy source and a 60° Michelson interferometer. The interferometer is used with a multilayer KBr beamsplitter for better signal in the 3000–6000 cm^{-1} regime. The maximum resolution is 0.5 cm^{-1}. A computer controlled internal mirror switches the beam from the internal beam to the parallel external beam option. The external beam path of the infrared beam has been designed using a standard ray tracing program. A flat mirror reflects the beam from the spectrometer down to the infrared cell level. Here a custom made 90° off axis parabolic mirror (by Janos Technology Inc.) makes a tight focus on the crystal through a Zinc Selenide viewport. This geometry is depicted in figure 2.5. The mirror is gold coated and has a focal distance of 7.5 inch. On the viewport, outside the vacuum, a KRS-5 wire grid polarizer is mounted to enhance the signal to noise of the measurements. This enhancement is achieved by filtering the s-polarization, which does not interact with the oscillators on the surface, out of the beam. The focused infrared beam is incident on the crystal at an angle of approximately 4° with the surface. In this geometry adsorbates on metal substrates give the highest signal to noise ratio. After reflection from the crystal, the beam exits the chamber through the second Zinc Selenide viewport. The exiting light is collected by a identical parabolic mirror and is transformed into a parallel beam. A third parabolic mirror is used to focus the light onto a linearized narrow band Mercury Cadmium Telluride (MCT) infrared detector. This detector has a high signal to noise in expense of the excessable wavelength range (700–10000 cm^{-1}). Since we are primarily interested in hydrocarbons this does not really cause limitations.

Front view
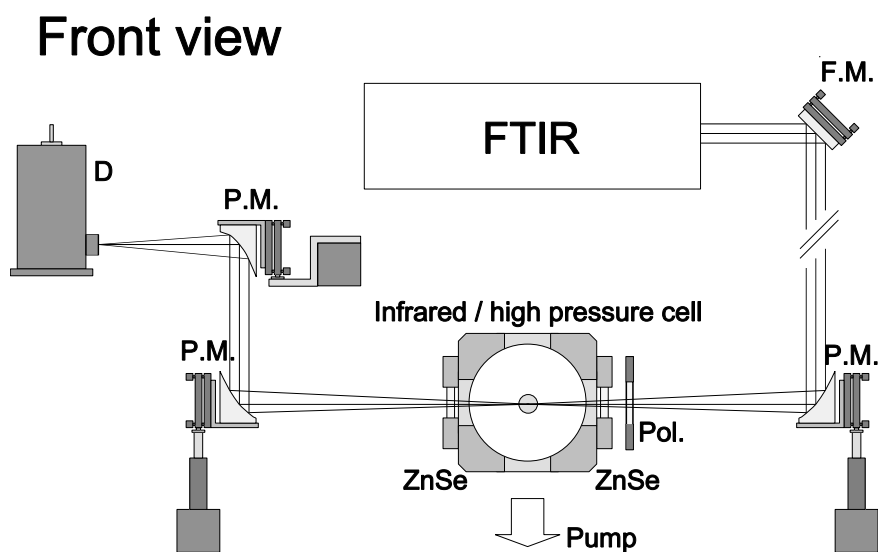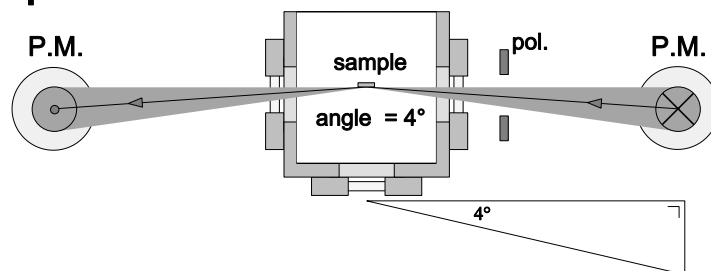
Top view

Figure 2.5: *Optical geometry to focus the infrared beam onto the crystal. Both front and top view are depicted. The high-pressure/infrared cell is shown as a section. FTIR: the spectrometer, F.M.: flat mirror, P.M.: 90° off axis parabolic mirror with gold coating, Pol.: KRS-5 wire grid polarizer, ZnSe: 23 mm diameter Zinc Selenide viewport, D: narrow band linearized MCT detector.*
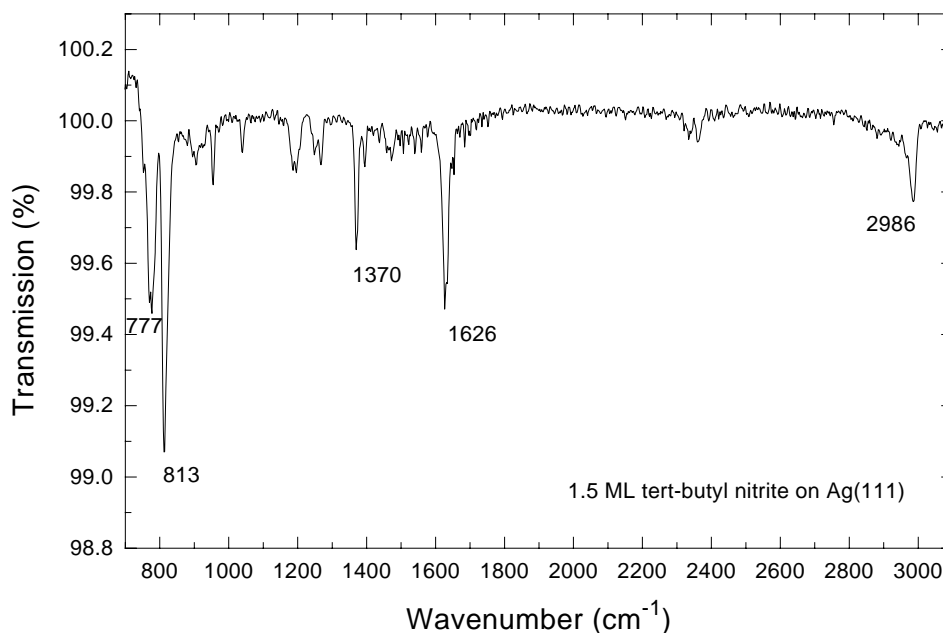
Figure 2.6: *RAIRS spectrum of 1.5 monolayer of tert-butyl nitrite adsorbed on Ag(111). Spectrum shows good signal to noise throughout the whole wavelength range.*

In the chosen set-up the angle of incidence on the crystal can easily be changed without the need for other parabolic mirrors. This changing would be necessary if experiments would be performed on other substrates like semiconductors. The complete beam path is purged with dry nitrogen to prevent absorption of the infrared light due to water vapor and CO_2 molecules. After the initial alignment of all the optical components, the repositioning of the crystal in the infrared cell turned out to be very facile, resulting is reproducible infrared spectra. During a 5 minute scan at 4 cm^{-1} resolution a signal to noise of 10^4–10^5 was achieved routinely. The installation of the spectrometer and optimization of the optics turned out to be very facile making the technique extremely useful. It can therefore be regarded as a standard surface sensitive technique.

2.4   Some results

A first study on the adsorption of methanol (CH_3OH) on Ag(111) on this system has already been published elsewhere[25]. In this study TDS and XPS is combined to study the adsorption energies, sticking coefficients and desorption products of methanol. TDS revealed desorption from three phases. These phases were identified as monolayer, amorphous multilayer and crystalline multilayer. This study clearly shows the capabilities of TDS.

To demonstrate the capabilities of RAIRS a spectrum of 1.5 monolayer of
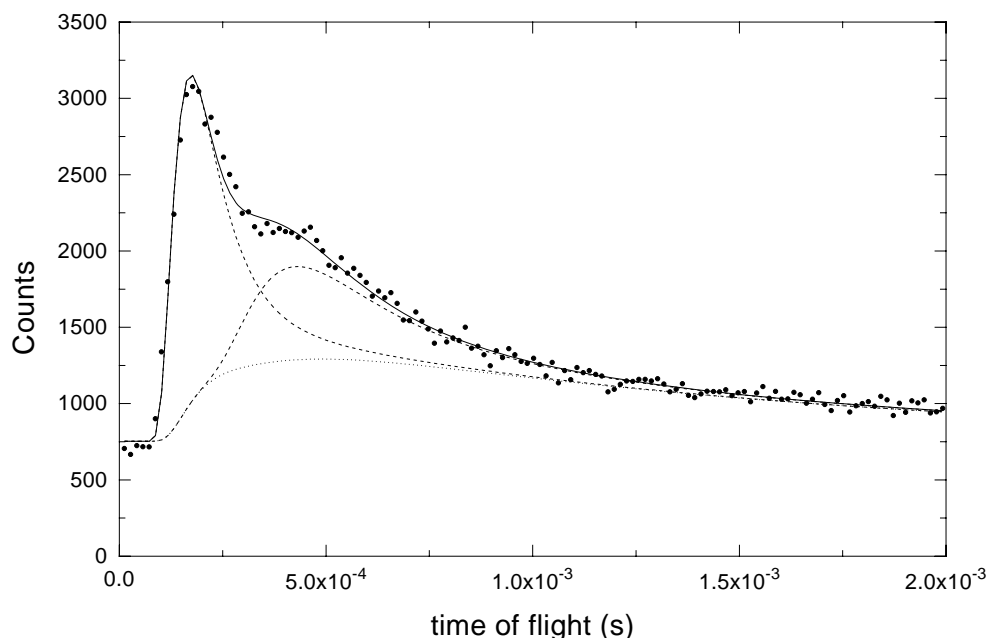
Figure 2.7: *TOF spectrum of NO produced by the photodissociation of one monolayer of tert-butyl nitrite, $(CH_3)_3CONO$, adsorbed on Ag(111) by 266 nm photons. Clearly two velocity components can be observed, indicating two desorption channels of the NO product. The figure also shows the decomposition of the data into two Maxwell-Boltzmann distributions and a pump tail caused by the two distributions (lowest curve).*

tert-butyl nitrite, $(CH_3)_3CONO$, adsorbed on Ag(111) is shown in figure 2.6. The presence of the CH stretch modes around 3000 cm^{-1} clearly shows the high sensitivity of the RAIRS setup. The signal to noise is about 10^4. The peak at 1626 cm^{-1} is due to the N=O stretch mode, the peak at 2986 cm^{-1} is the assymetric CH_3 stretch mode and the shoulder on the low wavenumber side is due to the symmetric CH_3 stretches. At 813 cm^{-1} the N-O stretch appears. The remainder of the peaks between 700 and 1600 cm^{-1} are all sceletal modes of the molecule. The two little peaks around 2350 cm^{-1} are due to fluctuations of the CO_2 concentration in the purged infrared beam path outside the vacuum system. The background subtraction did not completely correct for these absorptions due to these fluctuations.

If this layer is irradiated with 266 nm photons, the tert-butyl nitrite dissociates and NO desorption occurs. This process is monitored by TOF measurements with the mass spectrometer and the spectrum is shown in figure 2.7. In this figure a bimodal velocity distributions for NO can be observed. In the gas phase, where the photodissociation of tert-butyl nitrite is studied extensively, one velocity distribution is observed. This leads to the conclusion that since the dissociation occurs at a metal surface, a new reaction path is present. This new path is only observed, because of the capability of the apparatus to perform time

of flight measurements. The details of the surface photochemistry are discussed
elsewhere[26].

2.5   Conclusion

This apparatus is due to its flexibility very well suited to studying the interaction
between photons and adsorbates. It also shows that sample exchange and cooling
can very well be combined and that for sample exchangement not a lot of space is
required. By the choice of surface analytical equipment (TDS, XPS and RAIRS)
very detailed information about reaction pathways of adsorbates can be obtained.
Especially the RAIRS has a high added value in determining reactions of small
polyatomics.

Chapter 3

The adsorption of methanol on Ag(111) studied with TDS and XPS

Abstract *The adsorption of methanol on Ag(111) is studied using thermal desorption spectroscopy (TDS) and x-ray photoelectron spectroscopy (XPS). It is found that methanol adsorbs reversibly. The TDS spectra reveal three different states. These states can be assigned to molecules desorbing from the monolayer, the crystallized multilayers and the two amorphous multilayers that are located between the two other phases. This is the first time that these three states are seen by means of TDS. This multilayer behavior of methanol most likely also applies to other metals. The sticking coefficient is found to be coverage independent from the submonolayer into the multilayer regime. The desorption energy is found to be 0.41 eV. XPS shows for both the oxygen and carbon a small shift to higher binding energies with increasing exposure.*

3.1   Introduction

The interaction of methanol with metal surfaces has been studied on a variety of substrates like Ag(110)[3,27,28], Ag(111)[4], Cu(100)[29], Cu(110)[30,31], Cu(111)[32], all the faces of Pt[6,29,33–35], Pd(100)[36], Ni(110)[37], Ru(100)[38] and others. Most investigations are concerned with the decomposition of methanol on metal surfaces with or without the presence of preadsorbed oxygen. In the presence of preadsorbed oxygen methanol decomposes on almost all substrates. In the absence of preadsorbed oxygen there is always some degree of dissociation on all substrates but not on copper or silver. On copper and silver methanol adsorbs reversible. A number of articles have been published on the adsorption of methanol on copper because of the industrial importance of copper catalysts

in the methanol synthesis, but only a few articles are concerned with methanol on silver (Ag(110)[3,27,28],Ag(111)[4]).

Felter and coworkers[4] studied the adsorption of methanol on Ag(111) and its reaction with preadsorbed oxygen by means of ultraviolet and x-ray photoelectron spectroscopy (UPS and XPS). Since this study was not primarily concerned with the adsorption on the clean Ag(111) and since no thermal desorption data was present on this system, a new study had to be carried to investigate the adsorption behavior.

This adsorption behavior serves as a basis of future studies where methanol will be used on Ag(111). Especially the presence of thermal dissociation and the desorption temperature are essential. From experiments with methanol on copper it was know that methanol showed no dissociation. The general similarities in catalytic behavior of copper and silver suggested that thermal dissociation would be absent, but this had to be investigated.

3.2   Experimental

The experiments were performed in a newly built UHV system with a base pressure of 2×10^{-10} mbar. This system is described in detail elsewhere[39], but a brief description will be given below. The system is equipped with X-ray photoelectron spectroscopy (XPS), low energy electron diffraction (LEED) and a quadrupole mass spectrometer (QMS) for thermal desorption spectroscopy (TDS), time of flight mass spectrometry (TOF-MS) and residual gas analysis. The system is also equipped with a high-pressure cell for dosing up into the mbar regime.

The sample can be cooled down to approximately 100 K by liquid nitrogen and heated up to 1250 K by a tungsten filament behind the crystal. The temperature of the crystal is measured with a Chromel Alumel thermocouple and mastered with a temperature controller (Eurotherm 905S). The crystal current can be measured with a picoampère meter (Keithley 485). The crystal is mounted on a high precision manipulator with five degrees of freedom (three translational and two rotational degrees of freedom).

The Ag(111) crystal was cut by spark erosion and mechanically polished to give a misalignment of less than 0.1° as determined by Von Laue diffraction. The crystal was cleaned by Ar^+ bombardment at 600 K with Argon ions of 600 eV (20 minutes, 2.5 μA crystal current), followed by annealing for 15 minutes at 800 K. This procedure was repeated until no carbon and oxygen were detected by XPS and a sharp (1×1) LEED pattern was obtained.

The methanol (Merck, dried methanol >99.5%, water <0.005%) was transferred into a stainless steel container under a nitrogen environment to prevent water contamination and freeze-pump-thawed several times to remove high vapor pressure contaminants. The crystal was exposed to methanol via backfilling the chamber during a few minutes.

During dosing and TDS the mass spectrometer was set to monitor mass 31, since that is the most abundant fragment of methanol and there is no overlap

with residual oxygen. The exposures were calculated from the integrated partial pressure of methanol in the chamber during dosing and are expressed in Langmuir (1 L equals 1.33×10^{-6} mbar s). In this way exposures were reproducible within 10%. The exposures are not corrected for pressure gauge sensitivity. The TDS spectra were taken in line of sight with the mass spectrometer with a ramp rate of 15 K s^{-1}.

All XPS spectra were taken with x-rays from an Al K$_\alpha$ line and analyzed with a concentric hemispherical energy analyzer (CLAM 2, VG) with a pass energy of 20 eV and 4 mm slits. Multiple scans over an XPS-peak were taken to filter out possible instabilities of the instrument during the measurement. The clean Ag(111) spectrum showed a Ag$_{3d}$ doublet with binding energies of 367.9 and 373.9 eV and a FWHM of 1.1 eV. Carbon and oxygen were detected by scanning over the carbon 1s and oxygen 1s region. All energies quoted are binding energies.

3.3   TDS results

After adsorption of methanol at 110 K TDS spectra were taken with a ramp rate of 15 K s^{-1}. The results for increasing exposures are shown in figure 3.1. The TDS spectra reveal three different peaks, which are labeled as α_1, α_2 and β with increasing desorption temperature. For exposures below 4 L only the β peak appears in the TDS spectra. This peak increases with increasing exposure and saturates at an exposure of 4 L. The maximum of the β peak shifts from 167 K for small exposures to 163 K for an exposure of 4 L. This peak corresponds to the saturation of the monolayer. For exposures above 4 L a second peak appears in the spectrum at 143 K (the α_2 peak). This peak shifts to higher temperatures for increasing exposures. At 12 L exposure the α_1 peak appears and the α_2 peak does not increase anymore with increasing exposure. This α_1 peak continues to increase with increasing exposure. It was even possible to condense methanol ice on the substrate in such a way that the crystal turned completely white and that the corrugation of the condensed methanol could be seen by eye. The exposure used was about 10^6 L and was achieved by using the high pressure cell of the system.

If the area under the TDS curves is plotted against exposure, an uptake curve is obtained as shown in the inset of figure 3.1. Since the uptake curve is a straight line, it can be concluded that the sticking coefficient is independent of coverage throughout the whole exposure range. This observation combined with the fact that first the monolayer is completed before multilayers absorb, implies that an extrinsic precursor is involved in the completion of the monolayer. Since an exposure of 4 L (not ion gauge sensitivity corrected) is enough to form a monolayer and since the sticking coefficient is constant with coverage it is most likely that the sticking coefficient is unity. From the TDS data it can also be concluded that the α_2 phase is approximately two layers thick.

The occurrence of three peaks in the TDS can be explained as follows. At low exposures the β peak is the only peak present and saturates at an exposure
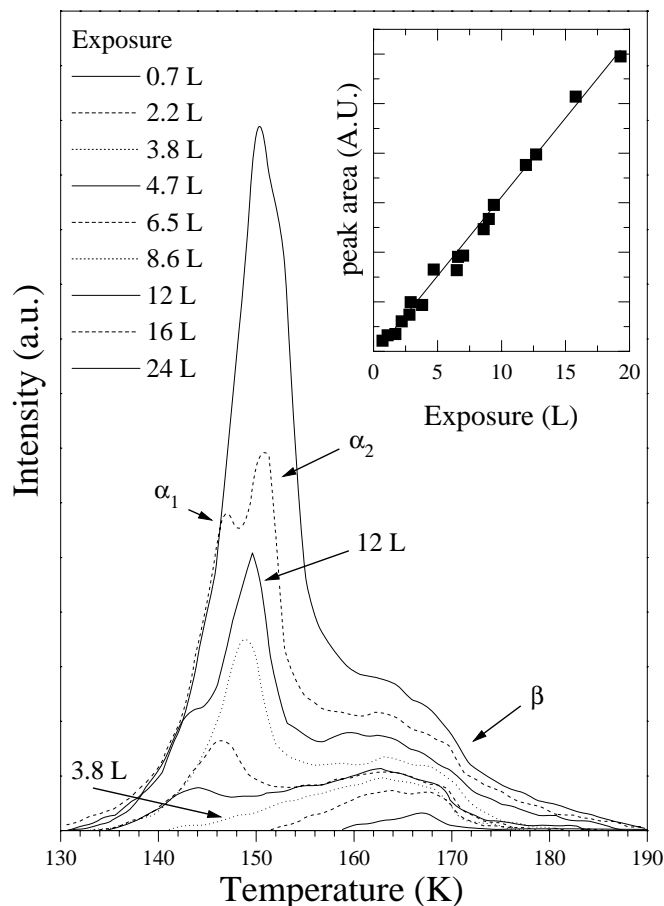
Figure 3.1: *TDS spectra for methanol adsorbed on Ag(111) for increasing exposures. Exposures are expressed in Langmuir (1 L equals 1.33×10^{-6} mbar s). For high exposures the spectra reveal three peaks. The peak with the highest desorption temperature corresponds with methanol desorbing from the monolayer. The other two peaks correspond with methanol desorbing from multilayers with an amorphous or crystalline structure. The spectra were taken with a ramp rate of 15 Ks^{-1}. The inset shows an uptake curve derived from the TDS spectra. This uptake curve shows that the sticking coefficient is independent of coverage.*

of 4 L. This peak can therefore be associated with the saturation of a monolayer of methanol. The next peak that appears in the TDS curves with increasing exposures (the α_2 peak) can then be associated with methanol molecules desorbing from multilayers. The third peak (the α_1 peak) appears when the α_2 peak saturates, so most likely this state can be associated with multilayers adsorbed on top of the α_2 state but with a different structure. Evidence for the difference in structure between the α_1 and α_2 phase can be found in work carried out by

Ehlers and coworkers on the adsorption of methanol on Pt(111)[40]. Ehlers and coworkers studied the adsorption behavior of methanol on Pt(111) by means of UV photoelectron spectroscopy (UPS) and reflection adsorption infrared spectroscopy (RAIRS). If methanol is condensed on Pt(111) on top of a monolayer below 125 K the multilayers will have a amorphous structure. Upon annealing to 125 K this amorphous phase will be partially converted into a crystalline α-ice phase leaving a few amorphous layers between the monolayer and the crystalline phase. Since it is not likely that the multilayer behavior of methanol depends greatly on the substrate, the α_1 phase on Ag(111) may then be attributed to a crystalline α-ice phase and the α_2 phase to an amorphous phase. The reason that the α_2 phase remains amorphous upon annealing is because of the lattice mismatch of the monolayer and the crystalline α_1 phase.

The crystallization of the methanol multilayers has also been observed with RAIRS for methanol on Cu(110)[31] and polycrystalline platinum[41]. After adsorption of methanol multilayers at 90 K the OH stretch band was split upon annealing to 123 K for 2 minutes, which was interpreted as crystallization of the multilayers into a α-ice structure. This splitting was only observed when more than three layers of methanol were dosed. In the experiment on Cu(110) it was not ruled out that at lower coverage also crystallization occurred but that this could not be detected because of resolution arguments. For the experiment on platinum it was concluded that only layer number four and higher had the ability to crystallize. This number of 4 agrees very well with the data presented here. Also TDS spectra of methanol on Ag(110)[27] show evidence for two different phases on top of the monolayer. The TDS peak for the multilayers seems to consist out of two peaks. But because of the slow temperature ramp in this experiment (5 K s^{-1}), the two phases are not well resolved.

So crystallization of methanol multilayers adsorbed on metal surfaces has been observed before with RAIRS but it was not completely certain whether some layers remained amorphous upon annealing. But because of the TDS data presented here it can be concluded that the two layers above the monolayer remain amorphous. The crystallization temperature is most probably the same for all metal surfaces (between 120 and 125 K), since for both Cu(110), Pt(111) and polycrystalline platinum this temperature is in that range. In this TDS study the crystallization of the multilayer will occur during the temperature ramp of the TDS.

In figure 3.1 can be seen that the monolayer peak exhibits an asymmetry, indicating a first order desorption process. By using the Redhead analysis[42], a desorption energy can be calculated from the peak maxima by using the following formula $E_d/kT_p^2 = \nu/\beta \exp(-E_d/kT_p)$. By assuming a pre-exponential factor ν of 10^{13} s^{-1} a desorption energy E_d of 0.41 eV is found, which agrees very well with values found on other faces of similar substrates like copper and silver. A selection of these values and desorption temperatures are shown in table 3.1. In this table also values for platinum and palladium are quoted to show the difference with other metals.

Table 3.1: *Thermal desorption parameters for methanol on various substrates. The multilayer desorption temperature is stated for the first multilayer and the monolayer desorption temperature is stated for a saturated layer. The desorption temperatures are extracted from TDS spectra with ramping rates varying from 2–15 $K s^{-1}$, so these values should only be used as a reference. The desorption energies are derived from the peak positions by assuming a pre-exponential factor of 10^{13} s^{-1}.*

Substrate	Multilayer desorption temperature (K)	Monolayer desorption temperature (K)	Desorption energy E_d (eV)	monolayer density cm^{-2}
Ag(111) (this work)	143	163	0.41	
Ag(110)[27]	140	165	0.42	5×10^{14}
Cu(111)[32]		210	0.56	
Cu(110)[31]	140	185	0.48	6×10^{14}
Cu(100)[29]	150	168	0.43	
Pt(111)[29,6,33,34]	145	190	0.49	
Pt(110)[35]	147	160–220	0.40–0.56	8.37×10^{14}
Pd(100)[36]	145	170,210	0.47	6×10^{14}

3.4   XPS results

The adsorption of methanol at 110 K was monitored by XPS, with spectra recorded over the O(1s) and C(1s) regions for a range of exposures (figure 3.2). Our XPS data is in good agreement with previous XPS measurements of the adsorption of methanol on silver and copper surfaces[4,27,30]. These studies have shown that methanol molecularly adsorbs on clean copper and silver surfaces. Spectra plotted in figure 2 show that at monolayer coverage that the C(1s) and O(1s) peaks have binding energies of 286.4 and 532.8 eV respectively. With increasing exposure of methanol the C(1s) and O(1s) peaks shift to higher binding energies. At exposures higher than 12 L the oxygen signal is attenuated because of the inelastic mean free path of the photoelectrons and thus changing the ratio of the carbon to oxygen peak area. From both the oxygen and carbon XPS data similar uptake curves as shown in the inset of figure 3.1 can be obtained, showing a coverage independent sticking coefficient. Thus our XPS results are in full agreement with our findings by TDS.

3.5   Conclusions

The methanol adsorption on Ag(111) at 110 K can be described in terms of three phases (α_1, α_2, β). After completion of the monolayer (β phase) methanol condenses as multilayers on the substrate with an amorphous structure (α_2 phase).
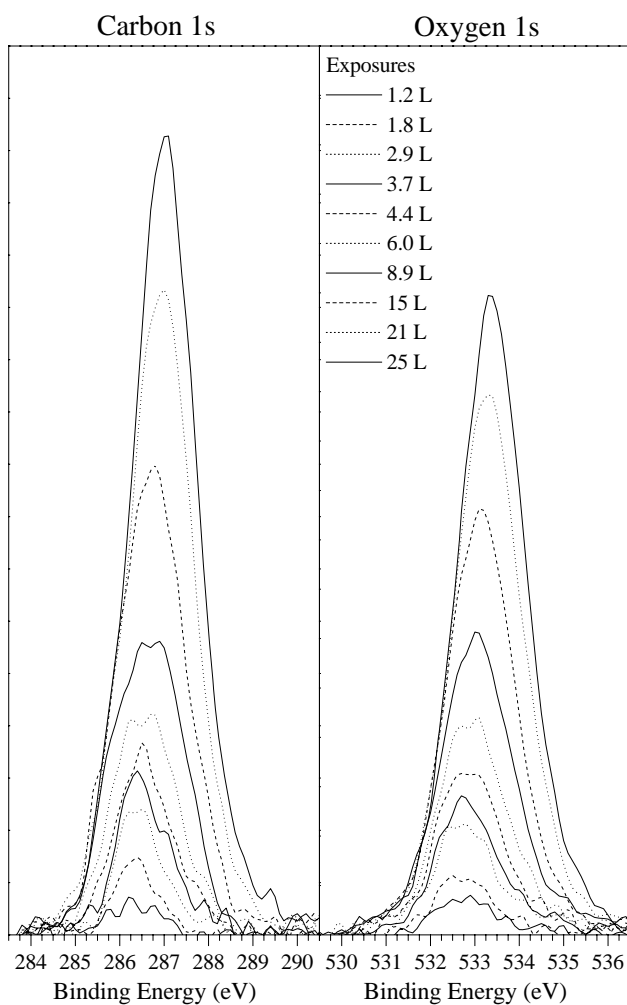
Figure 3.2: *XPS curves for C1s and O1s regions for increasing exposures of methanol. Both carbon and oxygen peaks show a gradual shift to higher binding energies.*

Upon annealing this α_2 phase will partially be converted into an crystalline phase with a α-ice structure (the α_1 phase). Only the first two layers above the mono-layer will remain in the α_2 phase to compensate for the difference in structure between the β and α_1 phase. The same multilayer behavior applies probably also to other metals. From both the TDS and XPS it can be concluded that the sticking coefficient is coverage independent. The monolayer has an desorption energy of 0.41 eV.

Chapter 4

The adsorption of tert-butyl nitrite on Ag(111)

Abstract *The adsorption of tert-butyl nitrite, $(CH_3)_3CONO$, on Ag(111) at 85 K is studied by thermal desorption spectroscopy (TDS) and X-ray photoelectron spectroscopy (XPS). Tert-butyl nitrite was found to adsorb reversibly and with increasing exposure first the saturation of the monolayer occurred and subsequently multilayers were formed. The sticking coefficient was found to be coverage independent. The desorption energies are around 0.42 eV in both the monolayer and multilayer regime.*

4.1 Introduction

The adsorption behavior of a molecule serves as a basis of many studies in surface science. Scattering, photochemistry and co-adsorption experiments build their results on the adsorption behavior of the individual molecule. We studied the photochemistry of tert-butyl nitrite, $(CH_3)_3CONO$, absorbed on Ag(111). The silver substrate was chosen because thermal dissociation is uncommon at this surface. To check this and to study the adsorption behavior in general, thermal desorption spectroscopy (TDS) and X-ray photoelectron spectroscopy (XPS) experiments were conducted. The photochemistry results and some reflection absorption infrared spectroscopy (RAIRS) on tert-butyl nitrite are reported elsewhere[26,43]. Alkyl nitrites are known to exhibit both a *cis* and a *trans* form. Methyl nitrite consists of a mixture of the two forms whereas tert-butyl nitrite mainly consists of the *trans* form[44–47].

When we started the study, no report was available on the adsorption of any alkyl nitrite on any metal substrate. Only during the course of the study an article by Pressley, Pylant and White was published on the adsorption of methyl nitrite, CH_3ONO, on Ag(111)[19] for coverages up to two layers. No thermal dissociation was found and with increasing exposure first the saturation of the monolayer and subsequently the formation of a multilayer was observed. They

did not report any data on the sticking coefficient

4.2   Experimental

The apparatus has been described in more detail elsewhere[25,26,39], but a brief description will be given below. The ultra-high vacuum chamber has a base pressure of about 2×10^{-10} mbar and is equipped with the following surface analytical tools: thermal desorption spectroscopy (TDS), X-ray photoelectron spectroscopy (XPS), Auger electron spectroscopy (AES), reflection adsorption infrared spectroscopy (RAIRS) and low energy electron diffraction (LEED). Besides for TDS, the quadrupole mass spectrometer (QMS) can also be used for time of flight (TOF) measurements.

The tert-butyl nitrite, $(CH_3)_3CONO$, was obtained from Aldrich with a specified purity of 96%. It was subjected to several freeze-pump-thaw cycles prior to use. The complete dosing manifold was made of stainless steel to minimize possible dissociation. The crystal was exposed to tert-butyl nitrite via backfilling the chamber for typically a few minutes during which the partial pressure was monitored by the QMS. From the QMS signal an accurate exposure could be extracted as described in more detail elsewhere[25,39]. The crystal was not allowed to face any electron or light source during dosing to minimize dissociation of the adsorbate.

The Ag(111) crystal was cleaned by cycles of sputtering with 800 eV Ar^+ ions at 650 K and annealing at 800 K. Cleanliness of the crystal was checked by XPS and LEED. The crystal could be cooled to 85 K by liquid nitrogen and heated to 800 K by a tungsten filament behind the crystal. The heating is controlled by an Eurotherm 905S temperature control unit, resulting in constant heating rates during TDS of 1 Ks^{-1}. The TDS spectra were taken in line-of-sight with the quadrupole mass spectrometer.

The XPS system consists of a VG Clam2 hemispherical electron energy analyzer and a VG XR3E2 twin anode x-ray source. The spectra were taken with Al K_α X-rays. For the carbon 1s and oxygen 1s regions a pass energy of 20 eV was used. For the nitrogen 1s a pass energy of 50 eV was used to obtain a higher signal to noise at the cost of the resolution. The two Ag 3d peaks were located at a binding energy (BE) of 367,9 and 373,9 eV. The full width at half maximum (FWHM) measured 1.1 eV at a pass energy of 20 eV and 1.7 eV at a pass energy of 50 eV.

4.3   Results and discussion

For a range of exposures with tert-butyl nitrite at 85 K, thermal desorption spectroscopy (TDS) spectra were taken at a heating rate of 1 Ks^{-1} (figure 4.1). The curves shown in the figure are recorded at mass 30, which is the strongest cracking fragment of the tert-butyl nitrite. By performing TDS for a variety
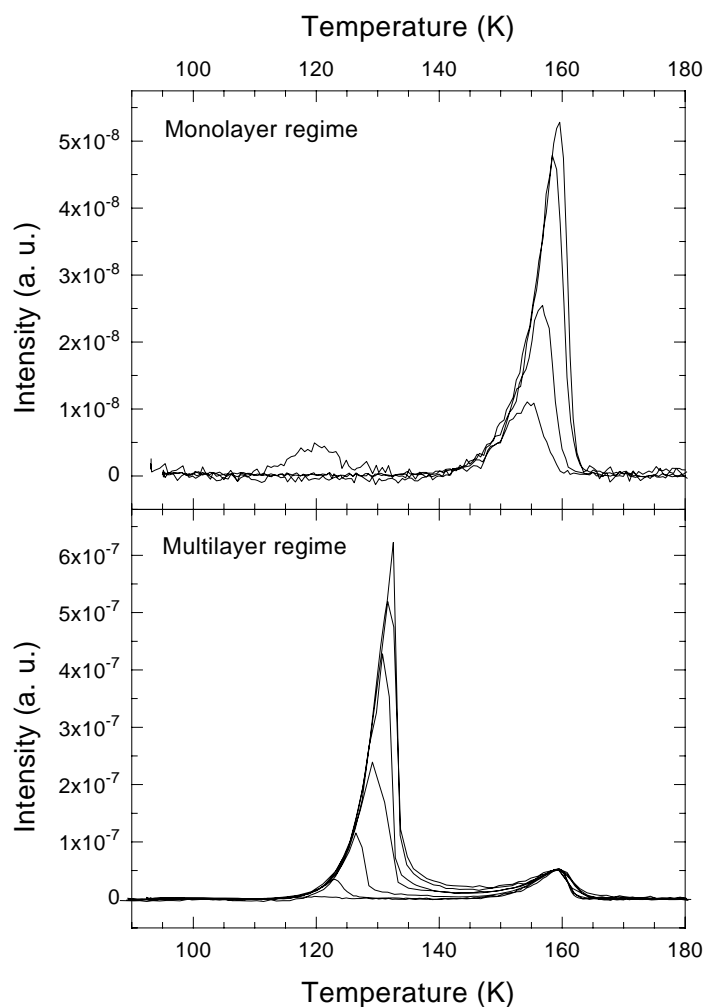
Figure 4.1: *TDS curves for exposures ranging from 2.3×10^{-6} mbars to 40×10^{-6} mbars at 85 K. In upper panel exposures are shown up to the saturation of the monolayer peak. In the lower panel exposures are shown that result in multilayer formation. The monolayer saturated at an exposure of 8×10^{-6} mbars.*

of masses and comparing these results with the cracking pattern of tert-butyl nitrite, it was concluded that the peaks shown in figure 4.1 are due to desorption of the intact molecule. XPS spectra taken after ramping a monolayer to 180 K showed that at most 10% of the initially adsorbed carbon was left on the surface. This small amount of carbon can originate both from a small amount of thermal dissociation of the tert-butyl nitrite and from the adsorption of impurities in the supplied nitrite (96% purity). TDS spectra could not reveal the identity of the carbon containing species. Flashing the crystal to 800 K resulted in a clean surface.

For small exposures, one peak is observed at 155 K. With increasing exposure the peak gradually shifts to 160 K. For exposures larger than 8×10^{-6} mbars this

peak does not increase anymore and a second peak is observed at 120 K. This second peak does not saturate, even not for exposures as high as 110×10^{-6} mbar s. This behavior is interpreted as, first the completion of the monolayer and subsequently the formation of multilayers. This adsorption behavior is common for a large range of organic molecules[25,48]. The asymmetric shape of the monolayer peak indicates a first order desorption process, which is common for physisorbed systems. By using the Redhead analysis[42], a desorption energy can be calculated from the peak position. Taking a pre-exponential factor of 10^{13} s^{-1}, which is a common value, a desorption energy of 0.43 eV is found. The overlap of the leading edges of the monolayer peak could also be interpreted as evidence for zero-order desorption, but this yields unphysical low values. For the multilayer peak all rising edges overlap. This indicates a desorption rate that only depends on temperature and not on coverage. This is characteristic for a zero order desorption process. From the leading edge of the multilayer desorption peak a sublimation energy per molecule of 0.42 eV is calculated[42,48,49].

By integration of the TDS curves in figure 4.1, the uptake curve shown in figure 4.2 is obtained. The figure shows a constant sticking coefficient for coverages ranging from 0 to 5 ML. A coverage independent sticking coefficient is measured for a variety of physisorbed molecules[25,50–52]. For exposures higher than 5×10^{-5} mbar s, all the data points were above the straight line shown in the uptake figure. The origin of this behavior is not known and no effort was made to study this in detail.

Our results agree with the findings of Pressley and coworkers[19]. Both methyl and tert-butyl nitrite adsorb reversibly and with increasing exposure first saturation of the monolayer occurs. For methyl nitrite lower peak desorption temperatures are found (131 K for the monolayer and 115 K for the first multilayer).

XPS experiments showed that X-rays caused dissociation of the nitrite. This was evident from the loss of NO and the appearance of a new oxygen peak. The dissociation is most likely due to the electrons formed in X-ray scattering and absorption events. Dissociation by X-rays was also observed for methyl nitrite on Ag(111) by Pressley and coworkers[19]. Flashing the crystal to 800 K was sufficient to clean the surface from dissociation products.

The nitrogen, oxygen and carbon 1s signals from a monolayer of tert-butyl nitrite were recorded in three separate experiments (figure 4.3). For each region a newly dosed surface was used and scan times were limited to six minutes. This was done to restrict the amount of X-ray induced dissociation to less than 20%. The structure in the nitrogen background is due to the silver XPS signal. Taking into account the atomic sensitivity, the different pass energies and a little amount of X-ray induced dissociation a C:O:N ratio of 4 : 1.8 : 1.0 is obtained from the spectra. This ratio matches very nicely the expected stoichiometry of tert-butyl nitrite.

After background subtraction, the nitrogen, oxygen and carbon peaks in figure 4.3 were fitted with Gaussians to deduce peak positions and peak widths (FWHM). The nitrogen peak, taken at a pass energy of 50 eV, was fitted with a single Gaussian centered at a BE of 404.1 eV and a FWHM of 1.7 eV. The oxygen
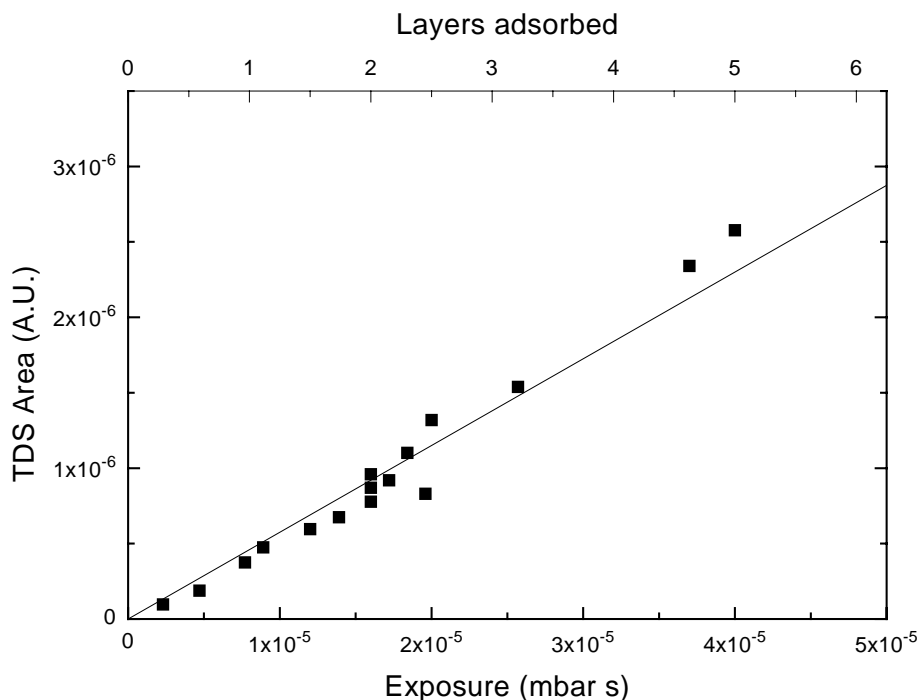
Figure 4.2: *Uptake curve obtained by integration of TDS peaks. For exposures ranging up to 40×10^{-6} mbar s a linear relation is found, indication a coverage independent sticking coefficient. The top axis shows a coverage scale deduced from the saturation of the monolayer peak.*

peak was fitted with the sum of two Gaussians with equal areas to account for the two oxygen molecules in the nitrite. This resulted in two peaks at a BE of 533.2 eV and 534.6 eV and a FWHM of 2.0 and 2.1 eV respectively. Allowing for different areas resulted only in slightly different values. The two carbon peaks are associated with the carbon of the methyl groups and the central carbon. Fitting the data to two Gaussians and assuming a ratio of 1:3 for the areas, resulted in binding energies of 284.9 and 286.9 eV and a FWHM of 1.6 and 1.4 eV respectively. All peak positions and width given above have a standard error of about 0.1 eV. Only the peak position of the oxygen peak at 534.6 eV has a uncertainty of 0.5 eV.

Pressley and coworkers[19] have performed XPS measurements on methyl nitrite. A comparison of their monolayer results with the results of this study are summarized in table 4.1. The BE of the ONO group match very nicely. Although slightly higher BE are found for the two oxygen species in this work, the deviations are within experimental error. Different BE are found for carbon due to the different hydrocarbon end groups.

The FWHM for the nitrogen and carbon peaks are essentially equal to the detector resolution. For oxygen, however, a FWHM of 2.0 eV is found whereas the detector resolution measures 1.1 eV. The reason for this broadening is most likely due to the fact that the tert-butyl nitrite is bonded via the two oxygen
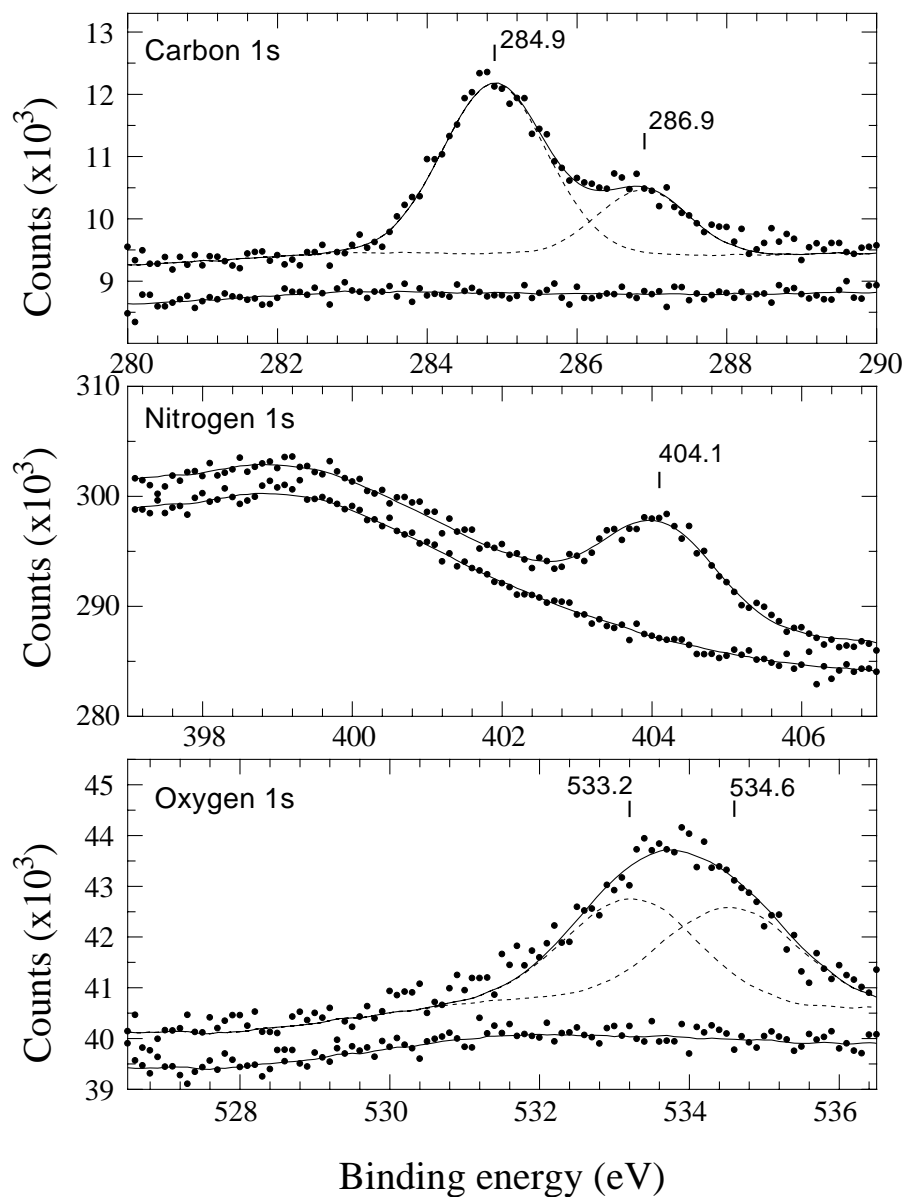
Figure 4.3: *XPS scans of the carbon, nitrogen and oxygen 1s region of a monolayer of tert-butyl nitrite. The spectra of the clean Ag(111) surface are also shown for comparison and are down-shifted for clarity. The oxygen and carbon regions are taken with 20 eV pass energy and the nitrogen with 50 eV pass energy. The fits are described in the text.*

Table 4.1: *Binding energies in eV of the carbon, oxygen and nitrogen 1s peaks for a monolayer tert-butyl nitrite, $(CH_3)_3CONO$, methyl nitrite, CH_3ONO[19], and methanol[25] adsorbed on Ag(111). The atom of interest is emphasized in the chemical formula.*

System	R**C**ONO	(**C**H$_3$)$_3$CONO	R**O**NO	RON**O**	RO**N**O
(CH$_3$)$_3$CONO	286.9	284.9	533.2	534.6	404.1
CH$_3$ONO	286.0		533.1	534.1	404.1
Methanol	286.4		532.8		

atoms to the substrate. Bonding to the surface via the lone-pair electrons of oxygen is common for a range of oxygen containing organic molecules like alcohols, ethers, acetone, and water[31,48]. Pressley and coworkers proposed bonding via the internal oxygen and possibly the nitrogen for both the *cis* and *trans*-methyl nitrite. Reflection adsorption infrared spectroscopy (RAIRS) on one monolayer of tert-butyl nitrite on Ag(111)[39,43], showed both a strong *trans* N=O and N–O stretch. This excludes an adsorption geometry with the N–O or the N=O parallel to the surface. We propose that tert-butyl nitrite is bonded to the surface in the *trans* form via both oxygen atoms. The ONO plane of the molecule will be more or less perpendicular to the surface. An ongoing NEXAFS study will provide us with more detail on the bonding geometry.

Chapter 5

Tert-butyl nitrite surface photochemistry, the transition from submonolayer to multilayer behavior

Abstract   *The photochemistry of tert-butyl nitrite, $(CH_3)_3CONO$, adsorbed on Ag(111) at 355 nm has been studied using time of flight (TOF) and reflection adsorption infrared spectroscopy (RAIRS) for coverages ranging from 0.1–50 ML. For all coverages a thermal and hyperthermal NO desorption distribution is observed due to photodissociation. The thermal component originates from hyperthermal NO molecules from the first and second layer, which were trapped by the silver substrate. The cross section for photodissociation is independent of coverage and matches the gas phase value. This is consistent with a direct excitation into the S_1 state. For coverages exceeding 5 ML the outermost layers still dissociate, but RAIRS shows that in the more inward layers caging is preventing dissociation. Due to caging only isomerization of tert-butyl nitrite is allowed as is evident from the RAIRS.*

5.1   Introduction

The surface photochemistry of physisorbed molecules is of interest, because it offers the possibility to study the photochemical behavior of a single adsorbate as well as the behavior of that molecule adsorbed in a thick film (glassy state). Especially interesting is the fact that this can be done in a single experiment under well-defined conditions and that the transition between these two extreme situations can be measured. Polyatomic molecules are very well suited for these studies, because they generally form multilayers at liquid nitrogen temperatures

and they adsorb photons in the wavelength region that is easy accessible with lasers. From an applicational point of view, it is also interesting to study the photochemical behavior of polyatomic molecules, because polyatomic molecules can be designed or chosen to exhibit a certain functionality. But often with the increasing number of atoms in the molecule also the complexity increases. The initial studies on the surface photochemistry were therefore basically conducted on diatomics like NO[14,53], CO[54–56], and O_2[57]. Lately, since more knowledge was gained about the surface photochemistry of diatomics, research moved towards polyatomics[19,26,58–65]. This trend as well as others is nicely reviewed in the following references[10,11,13,66].

The study of physisorbed molecules provides a link between matrix isolation, gas phase cluster and surface photochemistry. This link can provide valuable information to any of the fields mentioned above. For example the behavior of the photochemistry on a substrate as a function of coverage can yield important information for gas phase cluster dissociation, since there it is difficult to control the cluster size to the same extend as layer thickness on a substrate. Changing the substrate can provide insight in its role in the photochemical process as well.

Because of the complexity of polyatomics it is often very useful to study an adsorbate of which the photochemistry has been studied extensively in the gas phase. Alkyl nitrites (RONO) are an example of such a class of polyatomics. Alkyl nitrites are also interesting, because one of the gas phase photoproducts (the alkoxy) is an important intermediate in many catalytic reactions. As a substrate we chose to use silver. Silver is an ideal substrate to investigate the surface photochemistry of adsorbates, because thermal dissociation of the adsorbate is in most cases absent. This allows for the detailed study of non-thermal dissociation processes. Another advantage of the combination of silver and alkyl nitrites is that the NO photoproduct is likely to desorb, because of the low desorption energy. This enables us to monitor energetics of the reaction by time of flight (TOF) techniques.

The gas phase photochemistry of alkyl nitrites has been studied extensively[67–83]. All alkyl nitrites exhibit an excitation band between 300 and 400 nm. This band shows a vibrational progression due to the simultaneous excitation of the NO stretch mode in the alkyl nitrite[79]. After excitation into the responsible predissociative S_1 state, an alkyl and a NO fragment is formed. The lifetime of this S_1 state is measured to be 125 fs[79]. After dissociation of methyl nitrite, CH_3ONO, at 350 nm the NO fragment has an average translational energy of 0.5 eV[69,81]. For wavelengths shorter than 300 nm excitation into the direct dissociative S_2 state occurs. The S_2 state results in the same dissociation products as the S_1 state (NO and alkoxy). The translational energy of the NO fragment formed via the S_2 state is 0.8–1 eV[69].

The group of Huber[81–83] also studied the gas phase dissociation of methyl and tert-butyl nitrite, $(CH_3)_3CONO$, clusters via the S_1 state. Beside the highly excited Gaussian rotational NO product distribution observed in gas phase for isolated molecules, they found a Boltzmann rotational distribution with a rotational temperature of 250 K. The thermalized Boltzmann rotational distribution

was assumed to originate from molecules with NO solvated in the cluster and the Gaussian distribution from NO pointing outside the cluster. For large clusters of methyl nitrite also H_2CO (formaldehyde) and HNO (nitroxyl) were detected in the gas phase. These products originate from the reassociation of NO and CH_3O due to caging in the cluster. This process was optimal for cluster of about 60 molecules. Preliminary results on ethyl nitrite clusters[83] also showed the disproportionation reaction of the photoproducts towards HNO.

Matrix isolation studies on the photolysis of alkyl nitrite[46,47,84,85] show various caging phenomena in the S_1 wavelength regime. Both disproportionation of the photoproducts and isomerization is observed for both solid argon[46,47,85] and perfluordimethylcyclohexane[84] matrices. In argon matrices disproportionation was reported for both methyl nitrite[47,85] and tert-butyl nitrite[46]. The disproportionation reaction of methyl nitrite in argon yielded H_2CO (formaldehyde) and HNO (nitroxyl), tert-butyl nitrite in argon yielded $(CH_3)_2CO$ (acetone) and CH_3NO (nitrosomethane). Caging of methyl nitrite by perfluordimethylcyclohexane[84] showed the same disproportionation reaction as in argon. But matrix isolation of tert-butyl nitrite in perfluordimethylcyclohexane[84] did not show any disproportionation. For all systems photochemical *cis-trans* isomerization was observed[46,47,84].

Concerning the photochemistry of adsorbed alkyl nitrites only a few studies have been performed. Simpson and coworkers[61,62] studied the rotational, vibrational and translational distributions of NO after photodissociation of tert- and iso-butyl nitrite adsorbed on MgF_2. In this study a bimodal rotational distribution was measured. The highly excited Gaussian rotational distribution consisted of molecules with high translational energy and the thermalized Boltzmann rotational distribution consisted of molecules with low translational energy. Pressley, Pylant and White[19] studied the dissociation of methyl nitrite adsorbed on Ag(111) by electrons, X-rays and UV-photons. The UV-photon dissociation was studied on a monolayer of methyl nitrite. The TOF spectrum for the monolayer showed a bimodal translational distribution. In the discussion section we will deal with the surface photochemical experiments in more detail.

Thermal desorption and XPS spectra show that tert-butyl nitrite adsorbed and desorbs intact without any dissociation on Ag(111)[86]. The monolayer desorbs at 160 K and the multilayer of the first overlayer desorbs at 125 K. This behavior is very similar to the behavior of methyl nitrite as found by Pressley and coworkers[19]. They did not observe any thermal dissociation and the monolayer of methyl nitrite desorbed at 131 K.

5.2   Experimental

The ultra high vacuum (UHV) apparatus used has a base pressure of 2×10^{-10} mbar. The system has been described in more detail elsewhere[25,26,39], but a brief description will be given below. The ultra-high vacuum chamber is pumped by turbo-drag pumps backed with diaphragm pumps to minimize oil contamination

of the vacuum system. The following surface analytical tools are available: thermal desorption spectroscopy (TDS), X-ray photoelectron spectroscopy (XPS), Auger electron spectroscopy (AES), low energy electron diffraction (LEED) and reflection adsorption infrared spectroscopy (RAIRS). The quadrupole mass spectrometer (QMS) can also be used for time of flight (TOF) measurements.

The silver crystal was cut by spark erosion and polished to give a misalignment of less then $0.1°$. The crystal had a diameter of 10 mm and was cleaned by cycles of sputtering with 800 eV Ar^+ ions at 650 K and annealing at 800 K. Cleanliness was checked by XPS and LEED. The temperature of the crystal was measured with a chromel-alumel thermocouple. The crystal can be cooled to 85 K by liquid nitrogen and heated to 800 K by a tungsten filament behind the crystal.

The tert-butyl nitrite, $(CH_3)_3CONO$, was obtained from Aldrich with a specified purity of 96%. The tert-butyl nitrite was freeze-pump-thawed several times prior to use. The complete dosing system, including the tert-butyl nitrite container, was made of stainless steel to minimize dissociation of the molecule. The crystal was exposed to tert-butyl nitrite via backfilling the chamber during which the partial pressure was monitored by the QMS. From the integrated QMS signal an accurate exposure was extracted as described in detail elsewhere for methanol[25]. Because alkyl nitrites are photosensitive, the crystal was not allowed to face any light or electron source during dosing. TDS spectra taken from the adsorbed molecules revealed mono- and multilayer peaks. The uptake curve extracted from the TDS spectra indicates a coverage independent sticking probability. This allowed for the determination of a coverage scale from the observed saturation of the monolayer peak. The exposure needed to saturate the monolayer was 8×10^{-6} mbar s.

The RAIRS spectra were taken with a Biorad FTS 175 Fourier transform infrared (FTIR) spectrometer. The spectrometer is equipped with an air-cooled mid-infrared source, a multilayer KBr beamsplitter, a $60°$ Michelson interferometer and a linearized narrow band Mercury Cadmium Teluride (MCT) detector. In this study a CaF_2 viewport as entrance port and MgF_2 viewport as exit port for the vacuum system was used. This combination causes the transmission range to be cut off at 1200 cm^{-1} at the lower side. A KRS-5 wire grid polarizer was mounted on the entrance viewport to filter the s-polarized part out of the infrared beam. This causes a higher signal to noise, since the s-polarized part does not interact with adsorbates on the metal surface. The RAIRS spectra were taken in a compact cell that can also be used for high pressure dosing into the mbar regime. A detailed description of the optical geometry and cell are given elsewhere[39].

For the photochemical experiments a ps Nd:YAG laser from Quantel was used to illuminate the surface. The fundamental of the laser (1064 nm, 30 ps) was first doubled with a BBO crystal, subsequently the third harmonic (355 nm) was obtained in a KD*P crystal via sum frequency generation (SFG) of the second harmonic and the remaining fundamental. The third harmonic light was separated from the second harmonic and fundamental by a harmonic separator. By using a pinhole the central part of the third harmonic beam was used to irradiate the crystal. This resulted in a uniform beam with a diameter of 5 mm and

a typical pulse energy of 1.5 mJ. For time of flight (TOF) measurements, due to the positioning of the UV grade fused quarts viewports, the laser beam was incident at an angle of 52.5° with respect to the surface normal. Light impinging on the substrate was composed of equal amounts of S and P polarized light and the fluence per pulse at the surface was 4.6 mJcm^{-2}.

If RAIRS was used as a post-irradiation detection technique, illumination of the crystal was performed in the RAIRS/high pressure cell. In this situation the beam is incident normal to the surface and expanded to a diameter of 15 mm by means of a telescope in order to illuminate the whole crystal.

The TOF spectra were recorded using the Balzers 420 quadrupole mass spectrometer with a 90° off axis channeltron. The pulses from the channeltron were amplified using a fast current amplifier and subsequently detected by a multi-channel scaler (EG&G, turbo MCS). The MCS has a resolution of 5 ns, but the spectra shown in this article are recorded using a resolution of 15 μs. The mass spectrometer detected molecules desorbing almost along the surface normal (7.5° with respect to the surface normal). The flight distance between the crystal and the ionizer of the QMS was 13.5 cm.

A typical TOF measurement proceeded along the following way. After the crystal has been exposed to tert-butyl nitrite the base pressure was allowed to return to its normal value. This reduced the background level in the TOF spectrum. After optimization of the laser power a TOF spectrum was recorded during the first 400 laser shots. Subsequently spectra were recorded for the next 400, 400, 800, 1600, 3200 shots. In this way the exponentially decaying yield can be monitored and by summing all the separate files an accurate fit of the velocity distribution can be obtained.

Each peak in the TOF spectra was described using the Maxwell-Boltzmann velocity distribution of gas exiting a thermal source. Although most photochemical processes are non-thermal, the velocity distributions observed in such processes can often be very well described by a non-shifted thermal Maxwell-Boltzmann form[87]. Such a velocity distribution as measured by the MCS is described by the following form and is explained in more detail in the appendix of this chapter:

$$s(t_{\mathrm{MCS}}) = y_0 + \sum_{i=1}^{N} \left(\frac{c_i}{t_{\mathrm{MCS}} - t_0}\right)^4 \exp\left(-\left(\frac{t_i}{t_{\mathrm{MCS}} - t_0}\right)^2\right) + BG(t_{\mathrm{MCS}} - t_0) \quad (5.1)$$

In this equation t_{MCS} is the time between the laser shot and the detection by the MCS. The parameter t_0 is used to correct t_{MCS} for the flight time of the ion through the mass spectrometer to yield the true time of flight from the crystal to the ionizer of the mass spectrometer. The parameter t_0 was calculated to be 17 μs and was kept constant in the fitting procedure. Parameter c_i is a normalization parameter that determines the height of peak i, t_i determines the peak position of peak i, y_0 is the offset of the signal due the constant background of residual gas. The term $BG(t_{\mathrm{MCS}} - t_0)$ represents the background caused by pump tails of the desorbing molecules (see appendix for more detail). This term was introduced because the TOF signal had a very long tail that only returned to the normal background level after a few ms, whereas the TOF peaks occurred in the first

half ms. This tailing could not be explained by an extra desorption distribution, because this would yield an unrealistic heavy or slow molecule. Furthermore, the fitted time constant by which the background decays yields the same value for all experiments, which also supports the existence of a pump tail. And finally, the pump tail was also present at coverages of 1 ML or less which excludes the possibility that the pump tail is caused by slow diffusion out of the adsorbed film.

The fitting of equation 5.1 to the data was performed by a user written computer code based on a non-linear least square fitting routine. This routine gave estimations of the standard errors in the fit parameters. These errors are used throughout the article as a basis for error estimation for a variety of quantities.

From the parameter t_i the flux-weighted mean translational energy $\langle E_{\text{trans}} \rangle$ and the characteristic translational temperature $\langle E_{\text{trans}}/2k \rangle$ can be calculated.

$$\langle E_{\text{trans}}/2k \rangle = \frac{\langle E_{\text{trans}} \rangle}{2k} = \frac{ml^2}{2kt_i^2} \tag{5.2}$$

In this equation k is Boltzmann's constant, m the mass of the desorbing molecule and l the distance from the crystal to the ionizer of the QMS.

As is derived in the appendix, from the parameters c_i and t_i a measure for the total number of molecules, Y, in a desorption distribution and desorbing into the direction of the mass spectrometer can be extracted in the following way.

$$Y = \left(\frac{c_i}{t_i} \right)^4 \tag{5.3}$$

This quantity is only dependent on the experimental configuration so it can be used to compare yields under a variety of experimental conditions provided that the geometry is kept the same.

The cross section of a photochemical process can be determined by plotting the photochemical rate as a function the accumulated number of photons incident on the surface per unit of area of the substrate. If one assumes that the dissociation probability of a molecule is not influenced by the neighboring molecules, the cross section σ can be determined by fitting this plot with a single exponential decay of the following form.

$$Ae^{-\sigma F} \tag{5.4}$$

F is the fluence, which denotes the number of photons per unit of area. A is a normalization constant. This cross section σ is an experimental cross section because it yields the probability for a photochemical process per photon that is incident on the substrate at a certain angle. From the six successive TOF spectra taken for increasing amounts of irradiation time (see description of the TOF measurement above) this cross section can be extracted. From each spectrum an average desorption rate during the acquisition of the TOF spectrum can be extracted. But in order to determine the cross section via equation 5.4 one needs the desorption rate at a certain fluence and not an average rate during a fluence interval. An approximation could be made but a more elegant solution will be used here. From each TOF spectrum a yield can be extracted by means

of equation 5.3. The yield of the first spectrum is plotted at the accumulated fluence of the first spectrum, then the sum of the yield of the first and second spectrum is plotted against the sum of the accumulated fluence of the first and second spectrum and so on. In total six data points are obtained which represent the accumulated yield versus the accumulated fluence. This plot is described by the integral of equation 5.4.

$$\int_0^F A e^{-\sigma \tilde{F}} \, d\tilde{F} = \frac{A}{\sigma} \left(1 - e^{-\sigma F} \right) \tag{5.5}$$

Fitting this equation to the data will yield the experimental cross section.

5.3 Results

A NO desorption distribution was observed in TOF upon irradiation with 355 nm photons of a tert-butyl nitrite layer on Ag(111). No other desorbing molecules were detected in TOF. Figure 5.1 shows the recorded TOF spectra for different doses upon irradiation together with the fitted Maxwell-Boltzmann distributions as described in the experimental section. The inset shows the enlargement of the TOF spectrum for the monolayer dose. This reveals the existence of two components in the TOF spectrum for all exposures. For the two lowest exposures the two components are well separated and for the other exposures the slow peak appears as a shoulder of the fast peak. That at 50 ML still a thermal component is present is also evident from figure 5.2 where the TOF spectrum is fitted with both one and two velocity distributions. Clearly the two component distribution fits the shoulder behind the fast component much better. The two component distribution also mimics the fast peak better than the single component distribution. At coverages as low as 15% of a monolayer the two components were present in the TOF spectra with the same relative intensities as for the monolayer exposure.

Annealing the monolayer exposure to temperatures just below the monolayer desorption temperature had no effect on the TOF spectrum. This proves that the slow and fast peak cannot be attributed to desorption from the mono and multilayer respectively, because the annealing would have desorbed the multilayer or removed any clusters on the surface.

As can be seen from figure 5.1 the fast component gains intensity with increasing dose and it also shifts to shorter times. The slow component however does not seem to change drastically when the dose is increased and it saturates at approximately 2 ML. It is also quite evident that the TOF curves do not change if more than approximately 5 layers are adsorbed.

The behavior of the TOF peaks as a function of coverage can clearly be seen if the fit parameters from equation 5.1 are plotted. In figure 5.3 the fitted mean translational energies $\langle E_{\text{trans}} \rangle / 2k$ expressed in K are plotted for both the fast and slow component. The shift of the fast peak between 1 and 5 ML coverage in figure 5.1 can clearly be seen in the top panel of figure 5.3. For submonolayer coverage no major change in translational temperature is observed for the fast
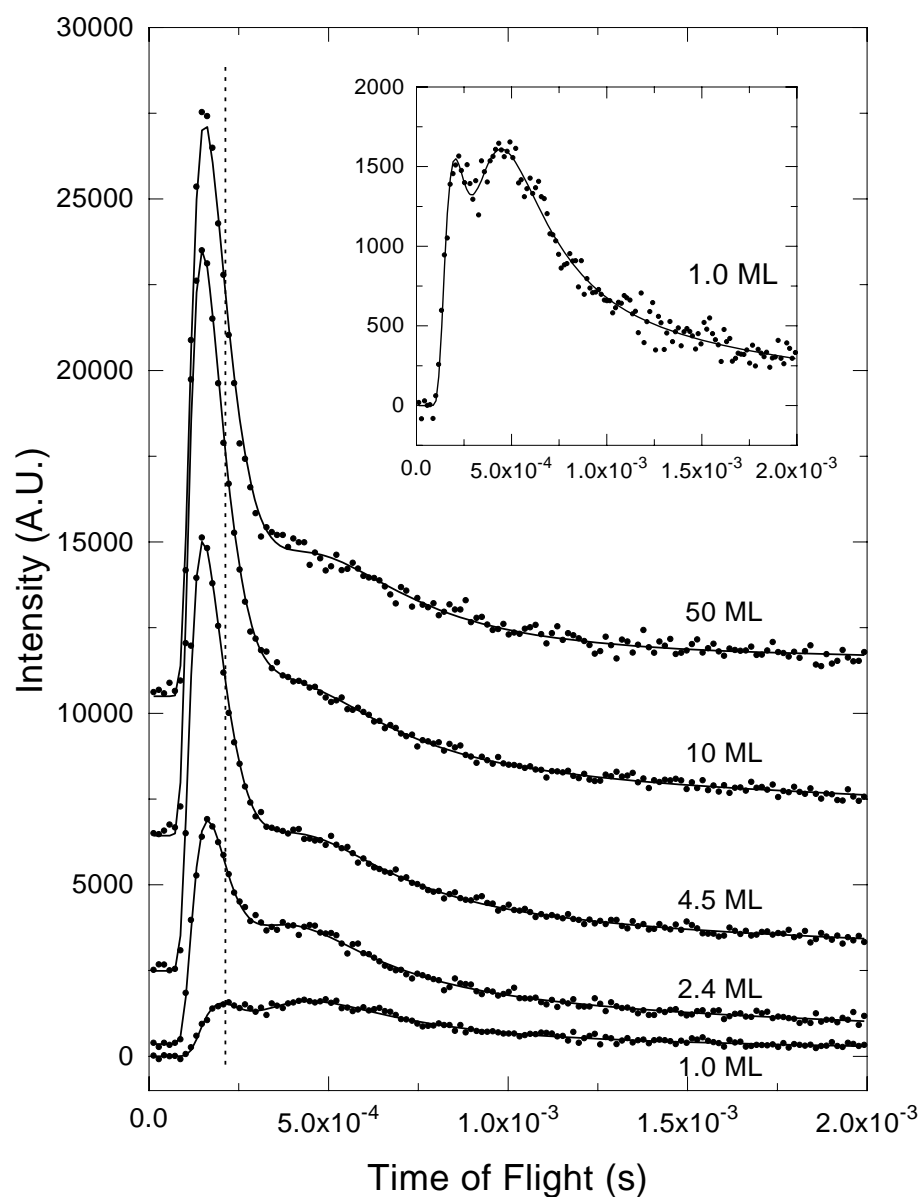
Figure 5.1: *TOF spectra for different exposures upon irradiation with 355 nm photons. The mass spectrometer was set to monitor mass 30 in order to detect desorbing NO, at other masses no peaks were observed. During dosing and irradiation the substrate temperature was kept at 85 K. Solid lines are fits to the data by using equation 5.1. The inset shows the enlargement of the 1 ML exposure.*
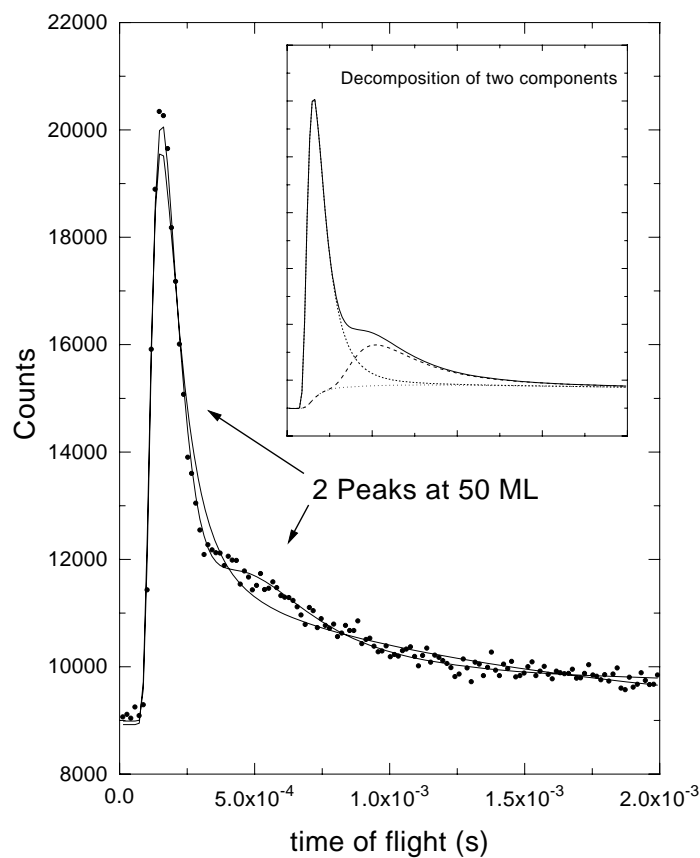
Figure 5.2: *TOF spectrum for a coverage of 50 ML fitted with one and two desorption distributions. The figure clearly shows the presence of the thermal component as a shoulder of the main peak. The inset shows the fit with two desorption distributions and the decomposition into a fast and slow velocity distribution together with the time dependent background contribution.*
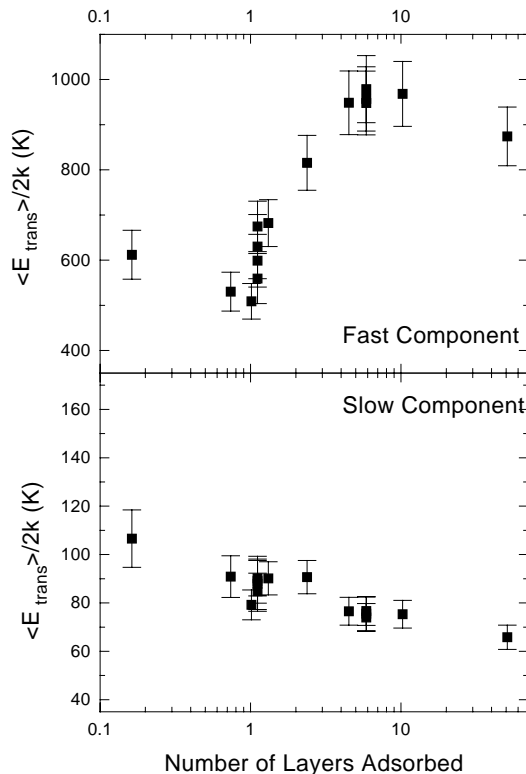
Figure 5.3: *Translational temperatures of both TOF components plotted against exposure on a log scale. These temperatures are obtained by fitting the TOF data.*

component. For coverages exceeding 5 ML also no change is observed. The slow component shows a decrease in translational energy with increasing coverage. The mean translational energies of the two distributions for the monolayer exposure expressed in K correspond to 550 ± 60 K for the fast component and 90 ± 10 K for the slow component (accuracies quoted are standard errors).

More insight in the slow component can be obtained if the translational temperature is plotted versus the substrate temperature during irradiation. This is shown in figure 5.4. Here the correlation between the substrate temperature and the translational temperature can clearly be seen, indicating that the slow component contains desorbing NO which has equilibrated to the substrate temperature. The slight deviation in the two temperature scales can be due to the uncertainty in the flight path or in the fitting procedure.

For coverages between 0.1 to 50 layers a set of TOF curves is measured as described in section 5.2. The sum of this set was fitted by equation 5.1 and via equation 5.3 a measure for the yield in each velocity component is extracted from the fitting parameters. The yield Y after 6800 laser shots as a function of coverage is plotted in figure 5.5. The yield of the thermal component is linear between 0 and 1 ML. At 1 ML saturation sets in and at a coverage of 2 ML saturation is complete. The linearity within the monolayer is also observed for the hyper-
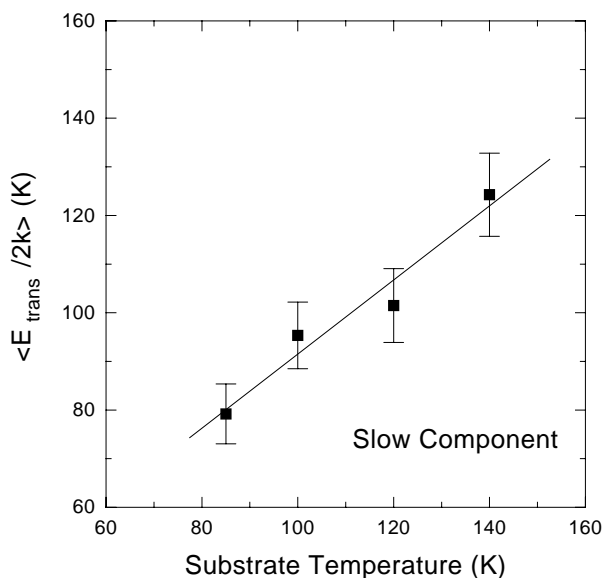
Figure 5.4: *The translational temperature of the slow NO desorption component as a function of the substrate temperature during irradiation. Clearly the correlation between the two can be observed. This translational temperature was not influenced by changing the dosing temperature or by annealing the adsorbed layer.*

thermal component. Beside the monolayer regime the yield of the hyperthermal component is also linear between 1 and 2 ML and between 2 and 4 ML. Kinks are observed at 1 and 2 ML coverage. At a coverage of 5 layers the yield of the hyperthermal component saturates. Even at coverages as high as 50 layers the same amount of thermal and hyperthermal NO is measured in TOF as at a coverage of 5 layers.

Using the procedure described in section 5.2, fitting function 5.5 to the data will yield the experimental cross section. That the yield does vary with coverage (see figure 5.5) does not influence the determination of the cross section. The cross section is only determined by the fluence (photons per unit area) needed to decrease the initial yield to $1/e$ times the initial value and does not contain any information about the absolute value of the initial yield. An example of a cross section determination is shown in figure 5.6. The plot of the integral TOF intensity versus fluence shows a very nice agreement between the model and the data. Subsequently, for a range of coverages the cross section was determined for both components (figure 5.7). The plot shows basically no dependence of the cross section on the coverage for both components. Only between coverages of 1 and 2 ML a slight enhancement may be present, but due to the experimental errors in the cross section this cannot be decided. The cross sections for the fast and slow component are very comparable. This becomes even more clear if instead of the absolute value of the two, the ratio is plotted (figure 5.8). This plot clearly shows
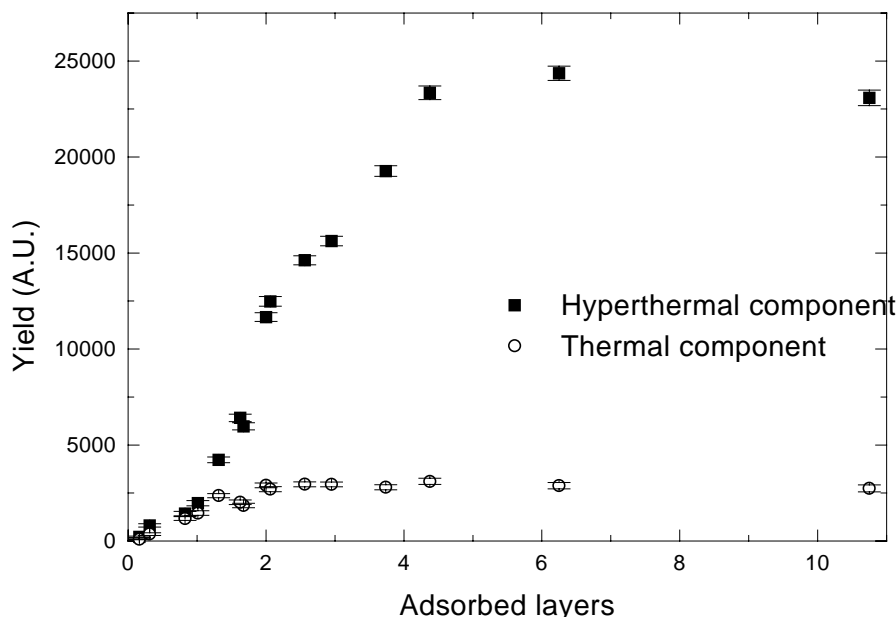
Figure 5.5: *Yield of the thermal and hyperthermal NO desorption components as a function of coverage. The yield is measured for 6800 laser shots of 1.5 mJ per pulse of 355 nm photons. Error bars are standard errors based on the uncertainty of the fit parameters as estimated by the fitting routine.*

that the two cross sections are within error equal to each other. The average value of the cross section of the fast component is 3.2×10^{-20} cm^2 and 3.3×10^{-20} cm^2 for the slow component. The average value of the ratio is 1.06 ± 0.13. Another data set taken in the early stages of the investigation on a different Ag(111) crystal yielded only slightly higher values for the cross section. This proves that even though absolute cross section measurements are difficult, reproducible results are obtained on different crystals and under different conditions.

To check whether an intensity dependence exists in the photochemistry, measurements where performed for different intensities for coverages of 1 and 6 ML. For these experiments the beam was compressed to 3 mm diameter and TOF spectra were recorded during 1600 laser shots. From these spectra both the yield and the translational temperature are extracted for both the thermal and hyperthermal component (figure 5.9). No intensity dependence was observed for the velocity of the two desorption distributions and the yield was linear with intensity. Despite of the few points in the graph it is clear that no quadratic or higher power relation is present. This indicates that dissociation is governed by a one-photon excitation.

Experiments with spacer layers allow for an investigation of the processes occurring in the top part of the adsorbed tert-butyl nitrite film. The presence of the spacer layer excludes photodissociation of the tert-butyl nitrite near the sub-
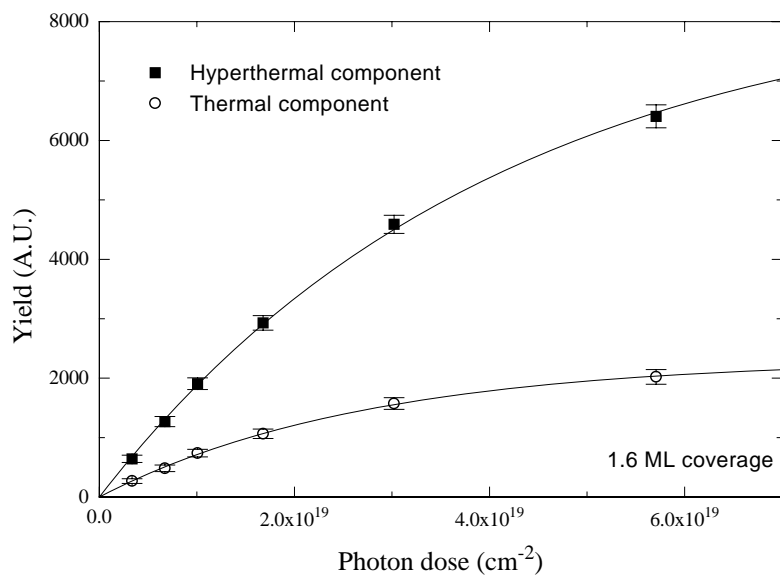
Figure 5.6: *Determination of the cross section by plotting the integral yield versus the accumulated photon dose. By using equation 5.5 and the fitting procedure described in section 5.2, the cross section is extracted. The figure shows data for a coverage of 1.6 ML. The fluence per laser pulse was 4.7 mJcm^{-2}.*
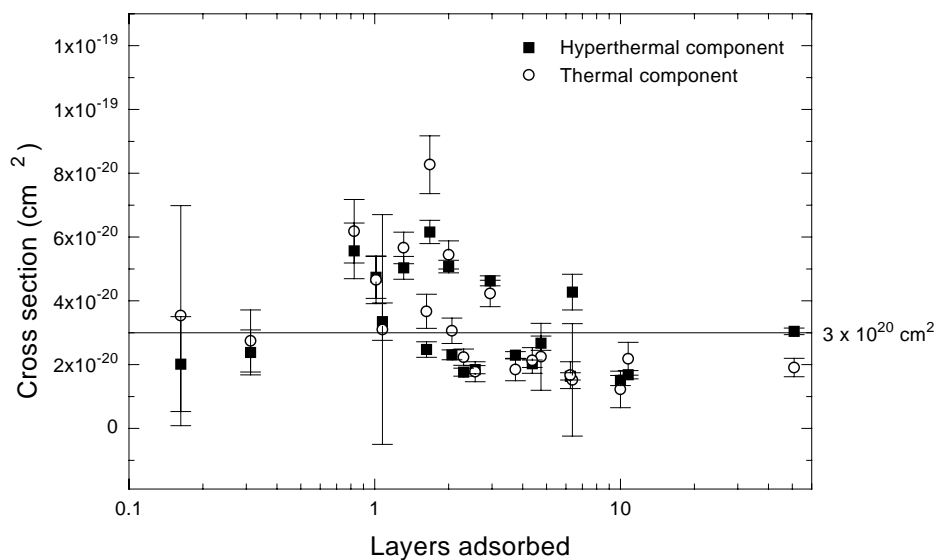
Figure 5.7: *Experimental cross sections for coverages ranging from 0.1 to 50 adsorbed layers of tert-butyl nitrite. The standard errors are deduced from the fitting procedure. The figure basically shows no dependence for the cross section on coverage.*
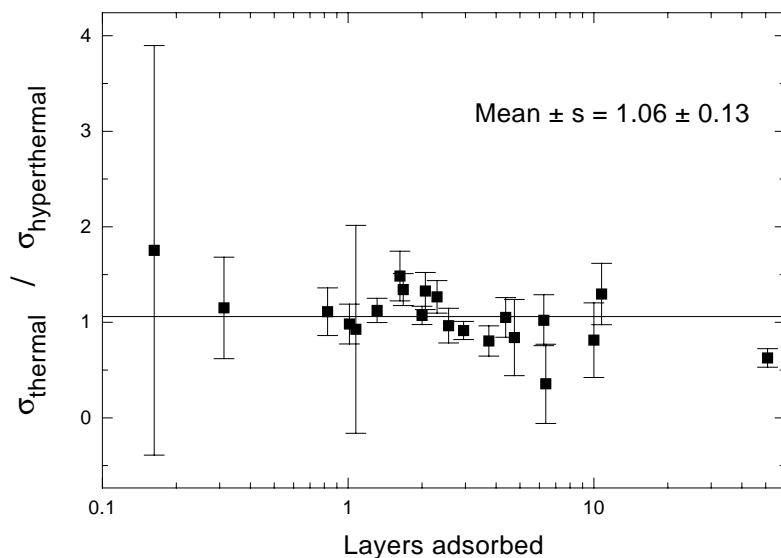
Figure 5.8: *Ratio of the cross section of the slow and fast component as a function of the coverage. The ratios indicate that the cross sections for the thermal and hyperthermal components are the same.*
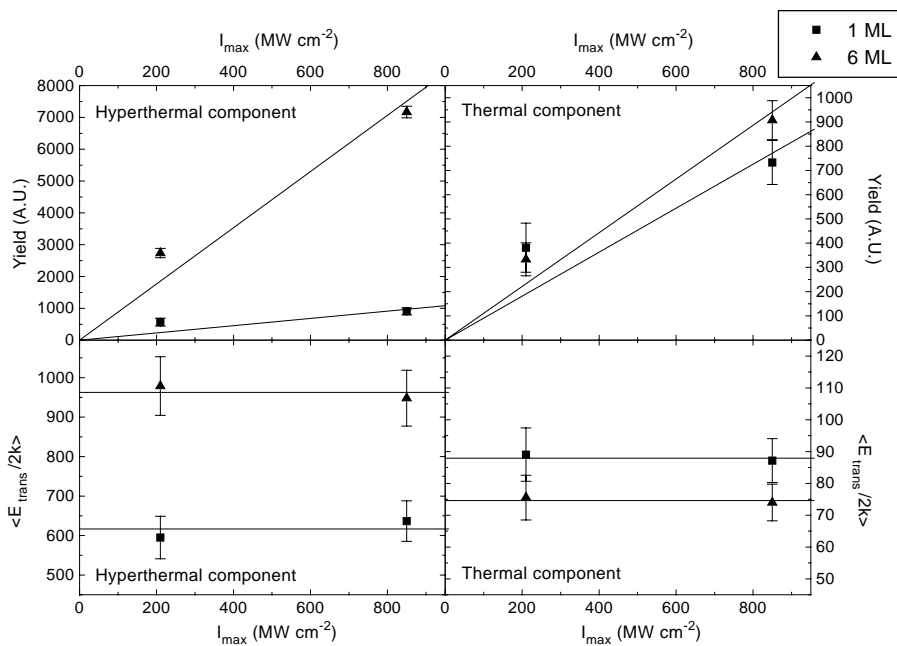
Figure 5.9: *TOF results for different intensities show no intensity effect. In every panel data is plotted for both 1 ML and 6 ML coverage. The left two panels show data for the hyperthermal component and the right two panels show the data for the thermal component. The top panels nicely show a linear relation between yield and intensity and no quadratic or power 4 relation. The bottom panels show that the translational temperature is independent of intensity.*
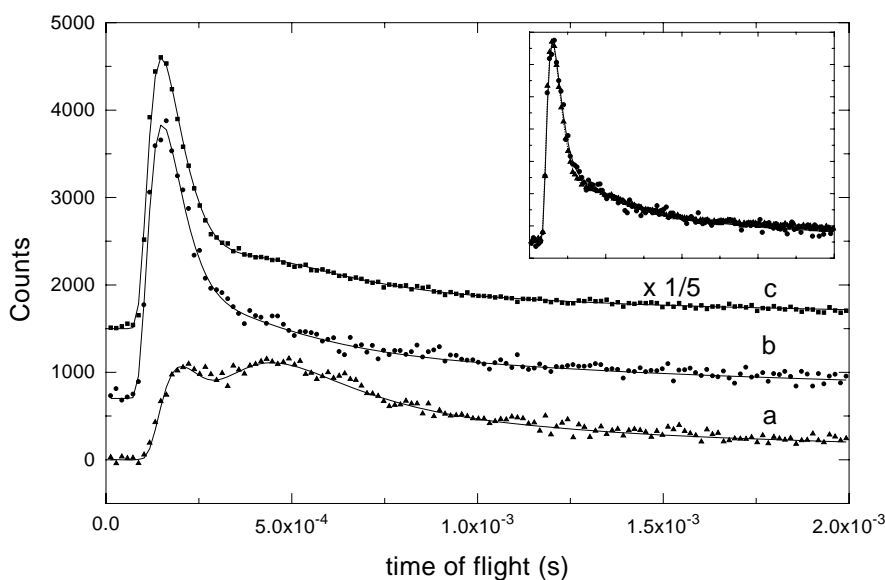
Figure 5.10: *TOF spectrum of 1 layer of tert-butyl nitrite on top of a 20 layer thick methanol spacer layer (curve b). For comparison the TOF spectra from 1 and 10 adsorbed layers of tert-butyl nitrite without spacer layer are shown (respectively curve a and c). The spacer layer TOF resembles the fast peak of the 10 layers thick film. The inset shows this match even more clearly.*

strate, simply because the tert-butyl nitrite molecule is replaced by the spacer layer molecule. If a thick spacer layer is required, methanol is a good candidate as spacer layer molecule. From our study on the adsorption of methanol on Ag(111)[25] it is know that methanol forms multilayers with a thermal desorption peak temperature of 145 K. At 85 K the methanol film will therefore be stable against thermal desorption. It is also known that if methanol multilayers are adsorbed at low temperatures an amorphous film is formed that becomes crystalline upon annealing the overlayer[25,31,40,41]. We have performed infrared measurements that show that annealing at 120 K for two minutes is more than enough to transform the amorphous overlayer into a crystalline one. Also is methanol inert under irradiation with 355 nm photons[66].

The methanol spacer layer was prepared in the following way. First 20 layers of methanol were adsorbed at 85 K and annealed for two minutes at 120 K to get a 20 layer thick crystalline spacer layer. The crystallinity of the spacer layer should hamper the diffusion of tert-butyl nitrite into the methanol film. Subsequently 1 layer of tert-butyl nitrite was adsorbed on the spacer layer. The time of flight spectrum obtained from this overlayer due to irradiation with 355 nm photons is shown in figure 5.10. In this figure the TOF spectra for 1 and 10 layers of tert-butyl nitrite without spacer layer are plotted for comparison. The spacer layer TOF is clearly different from the 1 layer experiment, so the displacement of the tert-butyl nitrite molecules away from the substrate has a pronounced effect. On the other hand if the 10 layer TOF is divided by a factor 5 than this curve is

almost identical to the spacer layer TOF. Both the yield and the position of the hyperthermal peak match perfectly. The inset of figure 5.10 shows this perfect match of the fast component very well. In section 5.4 this experiment will be discussed in more detail.

The time of flight measurements yield a lot of information on the desorbing molecules and therefore on the photochemistry. But no information is obtained about what is left on the substrate. This information is valuable as well when it comes to elucidating the photochemical process. Therefore RAIRS spectra were take of the adsorbed molecules before and after irradiation of the substrate.

For coverages of 1, 3 and 15 ML IR spectra were take before and after irradiation with 355 nm photons (figure 5.11). The peak around 1622 cm^{-1} is the N=O stretch mode of the O–N=O group. This peak is therefore a signature of the undissociated parent molecule. The strong peak at 2986 cm^{-1} is the asymmetric CH$_3$ stretch and the somewhat weaker peaks at 2942, 2911 and 2882 cm^{-1} are the symmetric CH$_3$ stretches. The peaks below 1450 cm^{-1} are all CH$_3$ deformation and rocking modes. The spectrum after irradiation for a coverage of 1 ML contains somewhat more noise due to incomplete cancelling of water vapor in the spectrometer after background correction. For a coverage of 1 and 3 ML the N=O stretch peak has completely disappeared after irradiation with 355 nm photons, indicating complete conversion of the adsorbed layer. There are no new peaks observed after irradiation. This indicates the absence of a new NO containing specie at the substrate and hence that all the NO is removed from the surface. Furthermore, the little change in the RAIRS spectrum indicates that the photoproducts that do remain on the surface have very similar vibrational spectra as the parent molecule. This is totally consistent with the picture that tert-butyl nitrite dissociates into NO and tert-butoxy. For a coverage of 15 ML however, only a reduction of 1/3 is measured. This reduction nicely corresponds to the observed saturation of desorbing NO at a coverage of 5 ML. The little change in the IR spectra before and after irradiation at a coverage of 15 ML indicates that most of the overlayer is unperturbed by the UV photons. Only one new feature is observed after irradiation of the 15 layer thick film. This feature is located at 1586 cm^{-1}. If the overlayer is heated after irradiation, between 120 and 140 K this feature disappears together with the NO stretch at 1622 cm^{-1}.

5.4   Discussion

In this section we want to discus 4 topics. First we will determine where in the film the hyperthermal component is produced. Subsequently, the origin of the thermal component will be discussed. This will open the way into the discussion of the excitation mechanism. And finally, the mechanism behind the saturation of the hyperthermal component will be discussed.
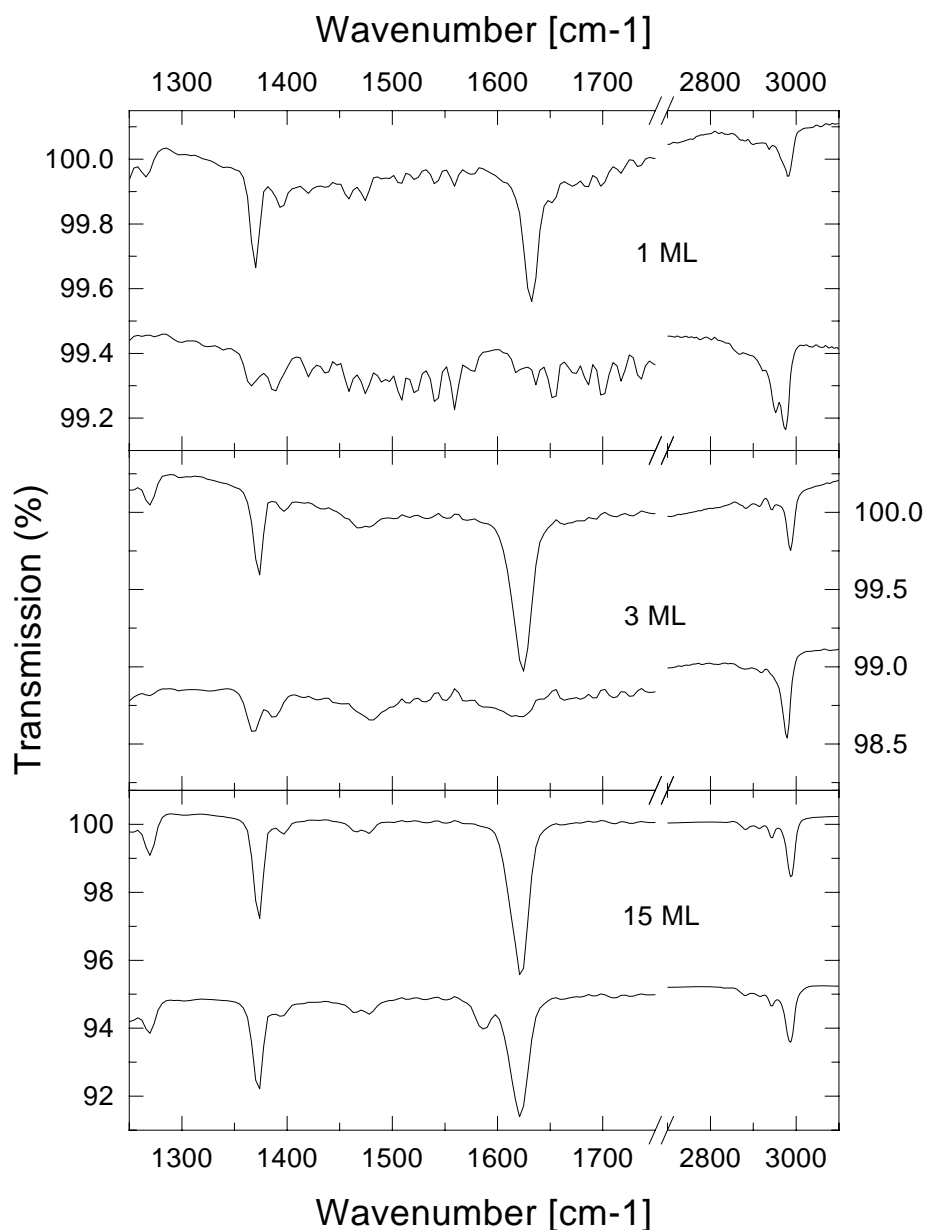
Figure 5.11: *RAIRS spectra before and after irradiation with 355 nm photons for coverages of tert-butyl nitrite of 1, 3 and 15 ML. Top curve in panel show RAIRS spectrum of adsorbed tert-butyl nitrite at 85 K and lower curve shows spectrum after irradiation. For coverages of 1 and 3 ML complete consumption of the 1622 cm^{-1} peak is observed. For a coverage of 15 ML only a reduction of 1/3 is observed. A new peak is observed for a coverage of 15 ML at 1586 cm^{-1}*

5.4.1 Origin of the hyperthermal component

The infrared spectra in figure 5.11 show complete conversion of the adsorbed layer for coverages of 1 and 3 ML. At these coverages there is no indication of new NO containing species at the surface. Therefore we conclude that all tert-butyl nitrite molecules at these coverages are photodissociated to form either fast or slow desorbing NO. At a coverage of 5 ML saturation of the yield of the hyperthermal component is observed (figure 5.5). At a coverage of 15 ML incomplete tert-butyl nitrite conversion is shown by the RAIRS spectra, supporting the observed saturation of the hyperthermal component in the TOF. For coverages higher than 5 ML, the velocity of the hyperthermal component remains high (figure 5.1 and 5.3). From this we can conclude that only the five outermost layers of the film are effective in producing hyperthermal NO upon irradiation with 355 nm photons. The hyperthermal NO can not be formed near the substrate because then at a coverage of 50 ML definitely all NO molecules would have been thermalized while scattering out of the film.

The observed saturation of the hyperthermal component at a coverage of 5 ML does imply that NO molecules can be transmitted through several layers without loosing most of their energy. The group of Madey[88–90] has shown that ions with a few electronvolt kinetic energy can be transmitted through several layers of rare gasses or water without loosing a large portion of their translational energy. Therefore it is not unlikely that neutral hyperthermal NO molecules can be transmitted through a few layers without significant loss of translational energy. If it is assumed that the top layer exhibits some roughness, only transmission through 2–3 layers is necessary to explain the results. Some degree of energy absorption by the film is conceivable, because the translational energy of the hyperthermal NO for large coverages (0.17 eV) is lower than would be expected from the gas phase results (0.5 eV for the dissociation of methyl nitrite).

The spacer layer experiment (figure 5.10) also supports the picture that for large coverages the hyperthermal NO molecules are formed in the outermost layers. Because, if a monolayer of tert-butyl nitrite is displaced from the substrate by a methanol spacer layer mainly hyperthermal NO is formed. The velocity of this hyperthermal NO also matches very nicely with the velocity of the hyperthermal NO formed for large coverages of tert-butyl nitrite (inset of figure 5.10). Even the expected ratio of 1:5 of the yields of hyperthermal NO of the spacer layer experiment and the 10 ML coverage TOF is found. This shows that the photochemistry of the tert-butyl nitrite is not influenced by adsorption on a methanol spacer layer.

5.4.2 Origin of thermal component

We have shown that the slow component consisted of NO molecules that had equilibrated to the substrate temperature (figure 5.4). But to make any firm conclusion about the origin of this thermal component more data was needed. In this article we have shown that the cross section for the thermal and hyperthermal

component are identical. This suggests that the dissociation pathways are very similar. That the similarity in the cross section is just a coincidence is very unlikely, because the scatter in the ratio of the two cross sections is much smaller than the scatter of the actual values. This indicates that this ratio of one is very fundamental in the dissociation process. From this we conclude that the thermal and hyperthermal component are formed by the same excitation process and that the transition states for the two reaction paths are identical. Only the reaction paths after the transition state determine whether a NO molecule desorbs thermally or hyperthermally. In section 5.4.3 we will show that the dissociation process is governed by a direct excitation.

Now we have deduced that the thermal and hyperthermal component are produced by the same excitation process, the question still remains where in the film is the thermal component produced. The onset of the saturation of the yield of the thermal component at a coverage of 1 ML and the actual saturation at 2 ML (figure 5.5) suggests that the thermal component is formed near the substrate. The fact that at a coverage of 50 ML still thermal NO is measured in the same amount as for a coverage of 2 ML (figure 5.5 and 5.2) then implies that thermal NO is able to diffuse through 50 layers on a time scale which is short compared to the time of flight (approximately $500\mu s$). However, another explanation of the observed saturation would be that the molecules which lead to thermally desorbing NO will float on top of the film and therefore show the observed saturation at a coverage of two layers. To check which of these two cases is true, the spacer layer experiment reported in figure 5.10 was conducted. If one monolayer of tert-butyl nitrite is displaced from the surface by a methanol spacer layer mainly a hyperthermal component is observed (curve b). If this one monolayer of tert-butyl nitrite is adsorbed directly on the silver substrate a much more efficient thermalization process is present causing a pronounced thermal component in the TOF spectrum (curve a). This clearly shows that only near the substrate an efficient thermalization process is present. Off course, this conclusion is allowed only if the photochemical behavior of the tert-butyl nitrite layer is not perturbed by the methanol spacer layer. That this is true is shown by the very nice match between the spacer layer experiment and the 10 ML nitrite film discussed in section 5.4.1.

The conclusion that the thermal component is produced near the substrate implies that thermal NO must be able to diffuse through 50 layers of tert-butyl nitrite on a time scale much shorter than 500 μs. A simple diffusion time calculation based on the Stokes-Einstein relation ($D = kT/6\pi\eta a$ with η=1 × 10^{-2} Pa s and a=1.5 × 10^{-10} m) and Brownian motion ($\langle z^2 \rangle = Dt/3$) resulted in a 15 μs diffusion time at 85 K, showing that diffusion of thermal NO through 50 layers is very well possible on that time scale.

We have concluded that NO is thermalized near the substrate. The question remains what interaction causes NO to thermalize. The two possibilities are interaction with the substrate and interaction with the adsorbates. If interaction with the adsorbates would lead to thermalized NO, then adsorbing more layers would lead to more thermalization. The yield of the thermal component already

starts to saturate at 1 ML and completely saturates at 2 ML. Increasing the coverage from 2 to 5 ML does not have any effect on the thermal component, whereas the amount of hyperthermal NO, which is in principle able to thermalize, does increase. So clearly, adsorbing more layers does not cause enhancement of the thermal NO component. Therefore we conclude that thermalization is caused by interaction with the silver substrate.

Scattering experiments[91] have shown that NO has a large trapping probability at an Ag(111) surface. For NO molecules with a translational energy of 100 meV a trapping probability of 40% was measured. The trapping probability did not change with the angle of incidence. This translational energy of 100 meV corresponds to a translational temperature of 600 K, which is the average translational energy in the hyperthermal component for coverages of 1 to 2 ML. So clearly, NO in the hyperthermal TOF component can be trapped by the Ag(111) surface with high probability.

The two conclusions made above (hyperthermal and thermal NO are formed by the same excitation step and NO is thermalized due to interactions with the substrate) lead to the following picture. There is one initial excitation step for both the thermal and hyperthermal component. But only near the substrate NO has a chance to be trapped by the surface and to become thermalized. NO formed by dissociation in the second layer has a finite probability (but smaller than in the first layer) to be thermalized by the substrate. For the third layer this thermalization probability is essentially zero, because of the distance to the substrate. In addition, NO formed in the third layer has a higher translational energy and therefore a smaller trapping probability as is shown by the NO scattering experiments[91]. For large coverages it is expected that all NO formed in the monolayer desorbs thermally, either due to thermalization by the substrate or due to multiple collisions in the film.

That the formation of thermal NO is governed by a branching ratio is also clear from figure 5.5. At the same point as where the thermal component starts to saturate (1 ML) the hyperthermal component takes off. At a coverage of 2 ML, where the thermal component completely saturates, an additional increase of the hyperthermal component is expected. However, this additional increase is not observed, presumably due to blocking of hyperthermal NO formed in the first two layers by molecules in the third layer.

If an alkyl nitrite molecule is dissociated in gas phase, only a hyperthermal translational, vibrational or rotational distribution is observed for the NO fragment. For gas phase clusters, however, Kades and coworkers[81–83] found a bimodal rotational distribution. Beside the Gaussian gas phase rotational distribution with high kinetic energy also a thermalized rotational distribution with low kinetic energy was found. The vibrational distribution of the slow rotational component was not significantly altered compared to the high rotational component. Thus, although the translational and rotational distributions can be thermalized in clusters, vibrational distributions are not. Simpson and coworkers found very similar results for iso- and tert-butyl nitrite on MgF_2[61,62]. The rotational distribution of desorbing $NO(\nu'' = 2)$ shows a Gaussian distribution for molecules

Table 5.1: *Mean energies of the observed translational and rotational distributions for the different systems. Mean energies are either expressed in K or in cm^{-1}. The low energy distributions are denoted as cold and the high energy distribution as hot. If no distribution is observed no value is given, if no measurements are performed on the existence of a distribution a question mark is placed.*

System	$\langle E_{\text{trans}} \rangle$		$\langle E_{\text{rot}} \rangle$	
	hot	cold	hot	cold
	(K)	(K)	(cm^{-1})	(K)
Gas phase:				
CH_3ONO 364 nm[81]	2900	–	2000	–
$(CH_3)_3CONO$ 364 nm[82]	high	–	1500	–
$[(CH_3)_3CONO]_n$ 364 nm[81,82]	high	low	1500	250
$(CH_3)_3CONO/MgF_2$ 351 nm[61,62]	2400–2000	400–700	1200	400–700
$CH_3ONO/Ag(111)$ 351 nm[19]	846	108	?	?
$(CH_3)_3CONO/Ag(111)$ 355 nm, this work	600	90	?	?

with a high translational energy similar to the gas phase and a Boltzmann distribution for molecules with a low translational energy. But although the rotational distributions are clearly bimodal and velocity dependent, the translational distributions do not show a clear bimodal distribution in contrast to our results. That NO does not bind to MgF_2 and does bind to silver is very likely the origin of the difference in the degree of translational thermalization. The vibrational distribution found by Simpson and coworkers does mimic the gas phase results for isolated molecules. The hyperthermal translational distributions should intuitively yield the same average velocity for large coverages. This is clearly not the case, for 2-4 ML of tert-butyl nitrite on MgF_2 a translational temperature of 2000-2400 K is measured and for 50 ML of tert-butyl nitrite on Ag(111) 1000 K is measured in this work (also the spacer layer experiment yielded the same temperature). A difference in condensed phase structure induced by the two substrates is to our knowledge the only conceivable explanation for this. That substrates can have pronounced effects on the structure of ultra thin films has been shown for water on various substrates[92,93].

Clear bimodal translational distributions are only found for alkyl nitrite on a silver substrate (Pressley and coworkers and this work). For silver no rotational distributions are measured, but we infer that bimodal rotational distributions would be found. The translational distributions reported in this study nicely agree with the distribution found by Pressley and coworkers even though different alkyl nitrites are used. That different alkyl nitrites give very similar results was already known from gas phase studies, but it is interesting to see that this also applies to surfaces. In the work of Pressley and coworkers the slow component is also thermalized to the substrate temperature (115 K), in agreement with our findings. In table 5.1 the energy of the translation and rotational distributions found in the studies mentioned above are summarized. All experiments are carried out with approximately 3.5 eV photons and all alkyl nitrites have a dissociation

energy of 1.8 eV[74] which leaves 1.7 eV to be divided over the different degrees of freedom of the system (including neighboring atoms).

Since the thermal NO is trapped by the substrate and since the substrate temperature is low, the residence time of the thermal NO is likely to be at least in the order of the laser pulse length (20 ps). Therefore, in principle, subsequent photochemistry on the trapped NO could be performed. So, Franchy and Ho[94] studied the photochemistry of NO adsorbed on Ag(111) at 340 nm. They found photodesorption of NO with a cross section of about 3×10^{-18} cm^2. Assuming that the thermal NO formed from tert-butyl nitrite is trapped longer than the laser pulse length and taking into account the laser intensity, a photodesorption probability of photochemically produced NO of only 2–3% is found. However, if a higher intensity is used or perhaps another wavelength, subsequent transient photochemistry is possible.

5.4.3 Excitation mechanism

Figure 5.2 shows that for coverages as high as 50 ML still hyperthermal NO is produced. This hyperthermal NO can only originate from the outermost layers, as is discussed in section 5.4.1. Therefore we can conclude that the photodissociation is caused by a direct excitation mechanism. And since the cross sections in the mono and multilayer are the same, the direct excitation process is apparently not quenched by the substrate, even not if excitation occurs in close proximity of the substrate. For low coverages there might be a parallel substrate mediated dissociation channel, but the present data does not suggest this. Perhaps the change in energy of the hyperthermal component with coverage could be due to the admixture of a substrate-mediated process. Another explanation for the change in translational energy could be the shorter residence time in the excited state close to the substrate. Future experiments on the wavelength dependence will shed more light on this subject.

At the wavelength used in our study, dissociation via the long-lived (125 fs), predissociative S_1 state is dominant in the gas phase[79]. This transition is out of the O–N=O plane, localized in the O–N=O group and the excited state has nπ^* character[95]. An excited state lifetime of 125 fs near the substrate seems unlikely at first sight. Most excited states in a substrate mediated dissociation process exhibit lifetimes in the order of (1–10 fs)[10,13,96]. That dissociation via the S_1 state is still possible near the metal substrate is due to three reasons. First, the excited state involved in a substrate-mediated mechanism is a negative ion state with an electron distribution far from equilibrium, whereas the S_1 state is an excited neutral state. Likely, this will already cause a difference in the quenching probability by the substrate. Secondly, the potential surface of the S_1 state could be deformed by the metal substrate. This could lead to a lower barrier and therefore a smaller tunneling time towards dissociation. This shortens the excited state lifetime of the S_1 state but keeps the quantum yield for dissociation close to unity as observed in the gas phase[79]. And last, it is known that the lifetime of a p-orbital near a substrate depends on whether it is a p$_x$, p$_y$ or p$_z$ orbital[97]. For

hydrogen the life time of a p_x and p_y orbital is an order of magnitude larger than the p_z orbital. Similar phenomena have been observed in negative ion formation at surfaces[98]. This phenomenon can also contribute to a longer excited state lifetime in the dissociation of tert-butyl nitrite.

Also gas phase cross section measurements support the direct excitation mechanism on silver. We measured a cross section for direct excitation of 3×10^{-20} cm^2 for 355 nm photons. The gas phase cross section at this wavelength is 6×10^{-20} cm^2[95]. These two values agrees very nicely, certainly if one realizes that values may range from 10^{-16} to 10^{-22} and that accurate absolute cross section measurements are difficult. The cross section values for methyl nitrite found by Pressley and coworkers agree with the gas phase values as well (2.6×10^{-19} cm^2 at 365 nm compared to 1.8×10^{-19} cm^2 in the gas phase). Pressley and coworkers also proposed a direct excitation mechanism on the basis of the correlation between photon and translational energy. Because of the uncertainties of the measurements Pressley and coworkers infer that a substrate mediated process is also active. Our measurements showing the same cross section for both the thermal and hyperthermal NO component and for both the monolayer and multilayer regime demonstrate that the majority of the desorbing NO is due to a direct excitation. Simpson and coworkers proposed a direct excitation on the basis of the similarity in the vibrational distributions compared to the distributions found in gas phase.

5.4.4   Saturation of hyperthermal component

In section 5.4.1 and 5.4.2 is discussed that the hyperthermal component is formed in the top of the film and the thermal component near the substrate. The question arises what causes the other layers not to produce any NO. It is evident that photons can reach these layers, because thermal NO is still produced at the surface and the extinction coefficient of tert-butyl nitrite is not that large. The RAIRS spectrum of 15 ML of tert-butyl nitrite shows very little change in the remaining layers after irradiation. So, the possibility that the inner multilayers undergo some kind of reaction and therefore become incapable in producing NO can be ruled out. The little change in the RAIRS spectrum does indicate that the inner multilayers molecules do not produce NO because they are surrounded by other adsorbates. This effect is generally known as caging[99–102]. Tert-butyl nitrite molecules in the multilayer are likely to be part of a weak hydrogen bonded network. This network is the reason why a tert-butyl nitrite molecule in an inner multilayer experiences to be in a cage that prevents dissociation of the molecule. That surrounding molecules can have a pronounced effect on the photodissociation is already shown by matrix isolation and cluster studies[46,47,83–85,99,100].

Now we have explained why the majority of the inner multilayers do not dissociate, we still need to discuss the origin of the new feature observed in RAIRS at 1586 cm^{-1} for a coverage of 15 ML. Barnes and coworkers[46] have shown that tert-butyl nitrite trapped in solid argon reacts to $(CH_3)_2CO$ (acetone) and CH_3NO (nitrosomethane). The new feature in figure 5.11 at 1586 cm^{-1} can not

Table 5.2: *Peak positions and peak differences of the NO stretch of both* cis- *and* trans-*tert-butyl nitrite. Values are quoted for gas phase[44], argon matrix isolation[46], liquid[103] and multilayer adsorption (this work)*

Environment	*trans* NO-stretch (cm^{-1})	*cis* NO-stretch (cm^{-1})	difference (cm^{-1})
Gas phase	1655	1610	45
Argon matrix	1638	1598	40
Liquid	1628		
Multilayer	1622	1586	36

be associated with the formation of acetone or nitrosomethane. Acetone has a very strong adsorption between 1700 and 1750 cm^{-1} and nitrosomethane has a strong adsorption around 1550 cm^{-1} and there are no peaks observed at these positions. The new feature at 1586 cm^{-1} is due to isomerization of *trans*-tert-butyl nitrite to *cis*-tert-butyl nitrite. Isomerization is a well known phenomena for alkyl nitrites[44–47,84]. The two geometries (*cis* and *trans*) exist due to the rotation of the N=O group around the O–N axis. The liquid and adsorbed tert-butyl nitrite consists basically out of the *trans* form. Identification of the geometry can be performed by IR spectroscopy due to the different positions of the ONO related bands. The difference between the *cis* and *trans* N=O stretch peak measured in this study is 36 cm^{-1}. This is close to the difference measured in an Argon matrix (40 cm^{-1}[46]) and in gas phase (45 cm^{-1}[44]). A comparison of the peak positions and differences can be found in table 5.2. As can be seen from this table, the difference between the two peaks is more constant then the actual positions. This is also what one intuitively would expect, the positions are dominated by the complete environment (vacuum, argon or tert-butyl nitrite) whereas the difference mainly by the change in geometry between *cis* and *trans*. The N=O stretch position of adsorbed *trans*-tert-butyl nitrite (1622 cm^{-1}) resembles very much the position found in the liquid[103] (1628 cm^{-1}) and differs considerably from the gas phase (1655 cm^{-1}). This indicates that nearest neighbor interactions play a dominant role in the adsorbed film. The assignment of the peak at 1586 cm^{-1} is also supported by the observation that this peak disappears at the same temperature as the *trans* N=O stretch upon heating the irradiated multilayer.

Caging effects in the photodissociation of alkyl nitrites have been observed before, both for clusters and matrix isolation studies[46,47,83–85]. The degree of caging at a certain wavelength can be divided in three levels as we will explain below. For weak caging photodissociation does occur but the photoproducts are not allowed to leave the cage. The photoproducts will therefore react with each other. In this disproportionation reaction NO will capture either a hydrogen or a methyl from the alkoxy photoproduct. A hydrogen is captured in the case of methyl nitrite as a parent molecule and a methyl is captured for the tert-butyl nitrites[46,47,83–85]. For intermediate caging movement along the reaction

coordinate is hindered even more by the cage. At this level of caging only iso-merization is allowed. The strongest caging occurs if the alkyl nitrite is totally unperturbed by a photon (even no isomerization).

For convenience we will enumerate the systems for which caging of alkyl nitrites have been observed.

1. Methyl nitrite in large gas phase clusters[83].

2. Ethyl nitrite in large gas phase clusters (preliminary results in reference [83]).

3. Methyl nitrite in an argon matrix at 14-16 K[47,85].

4. Methyl, ethyl, iso-propyl nitrite in perfluordimethylcyclohexane at 77 K[84].

5. Tert-butyl nitrite in an argon matrix at 20 K[46].

6. Tert-butyl nitrite in perfluordimethylcyclohexane at 77 K[84].

Weak caging occurs in most systems (system 1,2,3,4,5). Intermediate caging (isomerization) occurs in system 3,4,5,6. From system 1 and 2 it is unknown if isomerization occurs since only gas phase products were measured. So only in system 6 intermediate caging occurs without weak caging. Therefore system 6 and this study show the strongest caging observed so far for alkyl nitrites in the 300–400 nm wavelength range. Our findings that no disproportionation occurs agrees with the trend observed by Barnes and coworkers[46]: an increase of the tert-butyl nitrite to argon ratio caused isomerization to dominate over disproportionation. It must be noted that the disproportionation reactions of ethyl nitrite in system 2 and 4 are claimed to be different. For system 2 abstraction of a hydrogen by the NO radical is claimed and for system 4 abstraction of a methyl is concluded.

The reason for the strong caging observed in this study is two fold. First the cage formed by the tert-butyl nitrite molecules is stronger than the cage formed by methyl nitrite or solid argon. This can be concluded from the fact that tert-butyl nitrite forms gas phase clusters more readily than methyl nitrite[81]. This is likely due to the difference in the permanent electric dipole moment, which was calculated to be 60% larger for tert-butyl nitrite compared to methyl nitrite[81]. The second reason is that for tert-butyl nitrite no disproportionation reaction involving an α-hydrogen abstraction is possible because of the absent of such a hydrogen. Only disproportionation via the abstraction of a methyl is possible, but this requires more atomic rearrangement in the cage and is therefore less probable.

In spite of the caging in the multilayers, no caging is present in the monolayer as is apparent by the existence of a thermal component at a coverage of 50 ML (figure 5.2). Because tert-butyl nitrite molecules in the monolayer are bonded to the substrate, the difference in geometry with respect to the multilayer will prevent caging. Even in the case of weak caging in the monolayer, the reaction will be driven towards dissociation because of the strong bonding of the tert-butoxy to the substrate.

5.5 Conclusions

The surface photochemistry of tert-butyl nitrite on Ag(111) by 355 nm light is investigated by TOF and RAIRS measurements for coverages ranging from 0.1 to 50 ML. In addition, experiments with 20 methanol spacer layers have been performed. The conclusions from these experiments are listed below.

Tert-butyl nitrite adsorbed on Ag(111) at 85 K photodissociates under 355 nm irradiation to form desorbing NO. In TOF a thermal and a hyperthermal NO desorption component is observed throughout the investigated coverage regime. The thermal component is due to trapping of photochemically formed hyperthermal NO molecules by the substrate. Only hyperthermal NO molecules produced near the substrate contribute to the thermal component. Because the thermal NO is formed from the hyperthermal NO, cross section measurements yielded the same value for both components $(3 \times 10^{-20}$ cm$^2)$. Thermalization of photochemically formed NO from alkyl nitrites is also observed for gas phase clusters and MgF$_2$ surfaces, but for a silver substrate the degree of thermalization is the largest.

For coverages larger than 5 layers saturation of the hyperthermal component is observed. This is due to caging in the inner multilayers. The caging prevents complete dissociation and even disproportionation of the photoproducts towards CH$_3$NO and (CH$_3$)$_2$CO. Due to the caging of the surrounding tert-butyl nitrite molecules only isomerization is allowed. The degree of caging found in this study is high compared to caging of alkyl nitrites trapped in solid argon and even large clusters of methyl nitrite. For large exposures no caging is found in the monolayer. Summarizing the conclusion above, three distinct regions can be assigned in the film for coverages larger then 5 ML (figure 5.12): the outermost layers of the film that produce hyperthermal NO, the inner layers were caging is present and the monolayer were the thermal NO is produced.

The photodissociation is caused by a direct excitation of the molecule, presumably into the S_1 state. The measured dissociation cross section on Ag(111) $(3 \times 10^{-20}$ cm$^2)$ corresponds very nicely with the gas phase cross section $(6 \times 10^{-20}$ cm$^2)$. For dissociation to occur via the S_1 state, the excited state has to be long lived. The cross section measurements show that close to the substrate the cross section is not reduced by quenching of the excited state. For a substrate mediated mechanism is very weak evidence.

20 ML tert-butyl nitrite / Ag(111)
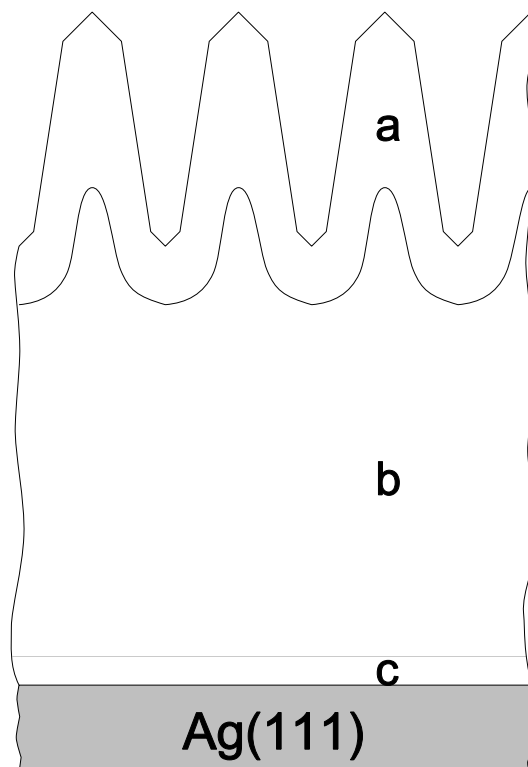
Figure 5.12: *Schematic representation of photochemical processes in the film. For coverages larger than 5 ML three regions can be assigned in the film. In the figure an example is given for a coverage of 20 ML. Region a: the top part of the rough multilayer. Due to an inelastic mean free path of several layers and due to the roughness of the multilayer a equivalent of 5 layers can be dissociated to form hyperthermal NO. Region b: inner multilayers. In this region caging is preventing dissociation of the molecule. Due to caging only isomerization is allowed. Region c: the monolayer. In the monolayer caging is not present and dissociation does occur. NO formed in the monolayer leaves the film with thermal velocities.*

Appendix

The velocity distribution of molecules exiting a thermal source is described by a
flux-weighted Maxwell-Boltzmann distribution of the following form.

$$f(v) = av^3 \exp\left(-\left(\frac{v}{v_\alpha}\right)^2\right) \tag{5.6}$$

The velocity of the molecule is denoted by v, a is a normalization constant
and v_α is equal to $\sqrt{2kT/m}$ (m is the mass of the molecule, k is the Boltzmann's
constant and T is the temperature of the source). In most cases this velocity
distribution can also be applied to molecules desorbing from a surface due to a
photochemical reaction. If these molecules would desorb in a sufficiently small
time interval around $t = 0$ and their time of flight, t, to a point at distance l from
this surface would be measured, then formula 5.6 can be expressed in the time
domain as follows.

$$\left.\begin{array}{l} f(t) = f(v)\frac{dv}{dt} \\ v = \frac{l}{t} \end{array}\right\} \Rightarrow f(t) = \frac{lc^4}{t^5} \exp\left(-\left(\frac{t_\alpha}{t}\right)^2\right) \tag{5.7}$$

Parameter c is a normalization constant derived from parameter a in such a
way that the final fitting formula (equation 5.9) has a simple form. Parameter t_α
is related to v_α by:

$$t_\alpha = \frac{l}{v_\alpha} = l\sqrt{\frac{m}{2kT}} \tag{5.8}$$

The formula for $f(t)$ above is in a flux-weighted form (number of molecules
arriving per unit of time), but since we use a density detector (the QMS) the for-
mula has to be converted to a density-weighted distribution $d(t)$ in the following
way.

$$d(t) = \frac{f(t)}{v} = \left(\frac{c}{t}\right)^4 \exp\left(-\left(\frac{t_\alpha}{t}\right)^2\right) \tag{5.9}$$

This formula is used to describe a single desorption distribution as measured
by the mass spectrometer. Via formula 5.8 the fit parameter t_α can be converted
to T which is the translational temperature of the distribution ($\langle E_{\text{trans}}/2k\rangle$).
A measure of the total number of molecules in the fitted Maxwell-Boltzmann
distribution can be obtained in the following manner. By integrating the flux-
weighted velocity distribution, $f(t)$ from equation 5.7, over time a measure of
the yield is obtained. This yield measure Y is proportional to the number of
molecules desorbing into the direction of the mass spectrometer and does only
depend on the experimental geometry.

$$\int_0^\infty f(t)\,dt = \frac{l}{2}\left(\frac{c}{t_\alpha}\right)^4 \implies Y \stackrel{\text{def}}{=} \left(\frac{c}{t_\alpha}\right)^4 \tag{5.10}$$

In the definition of Y the factor $l/2$ is omitted for simplicity, since Y is geom-
etry dependent anyway.

Generally a TOF trace can contain more than one desorption distribution, so a sum over the individual desorption components is taken. In a TOF trace there is also a constant offset y_0 present due to the presence of residual gas. Furthermore a pump tail due to trapping of some of the desorbing molecules on the walls of the ionizer and other parts of the system can be observed resulting in a time dependent background $BG(t)$. Therefore the total TOF trace as measured by the multi channel scaler $s(t_{\mathrm{MCS}})$ can be described by the following formula.

$$
\begin{aligned}
s(t_{\mathrm{MCS}}) \quad &= y_0 \quad + \sum_{i=1}^{N} d_i(t_{\mathrm{MCS}} - t_0) + BG(t_{\mathrm{MCS}} - t_0) \\
&= y_0 \quad + \sum_{i=1}^{N} \left(\frac{c_i}{t_{\mathrm{MCS}} - t_0} \right)^4 \exp\left(- \left(\frac{t_i}{t_{\mathrm{MCS}} - t_0} \right)^2 \right) \\
&\quad + BG(t_{\mathrm{MCS}} - t_0)
\end{aligned} \tag{5.11}
$$

In this formula t_0 is used to correct the time of flight measured by the MCS (t_{MCS}) for the time of flight of the ion through the mass spectrometer. This time t_0 is calculated by composing the quadrupole mass spectrometer out of acceleration, deacceleration and drift sections. By calculating the total sum of the time of flights for each section, the time of flight t_0 of the ion through the mass spectrometer is obtained. For mass 30 (NO) a time of 17 μs was calculated. The parameter c and t_α of the individual velocity distribution in formula 5.9 are labeled as c_i and t_i in formula 5.11 for distribution number i. Formulas 5.8 and 5.10 that determine the translational temperature and the yield of the individual distribution are still valid. The functional form of the time dependent background contribution $BG(t)$ (without the correction t_0) is derived below.

In order to take the pump tail of the desorbing molecules into account a approximation for this background contribution is made. The goal was to find a functional form for this background that started at zero for $t = 0$ (since then no molecule has yet desorbed to contribute to this background) and that could account for the elevated background at larger times were the Maxwell-Boltzmann distributions gave no signal anymore. In between these two extreme positions the background should have a form which is intuitively right: the maximum of the background signal should not be earlier than the maximum desorption signal as measured by the QMS and at larger time the background should be represented by an exponentially decaying form. The approximation that satisfies these criteria is explained below.

Molecules that desorb at a certain time are assumed to contribute to an exponentially decaying background. This background is said to be proportional to the amount of desorbing molecules that enter the mass spectrometer at time $\tilde{t}$. This amount is given by the sum of all individual desorption distributions $f_i(\tilde{t})$. The proportionallity factor is defined to be c_{BG}. The time constant of the exponential decay is defined to be t_{BG}. As a formula the background at time t due to molecules arriving at the mass spectrometer at time $\tilde{t}$ is give by.

$$
BG(t, \tilde{t}) = \begin{cases} c_{\mathrm{BG}} \sum_{i=1}^{N} f_i(\tilde{t}) \exp\left(- \left(\frac{t - \tilde{t}}{t_{\mathrm{BG}}} \right) \right) & t \geq \tilde{t} \\ 0 & t < \tilde{t} \end{cases} \tag{5.12}
$$

To get the total background contribution $BG(t)$ due to all molecules in the

desorption distribution and due to all distributions, $f_i(t)$, formula 5.12 has to be integrated over $\tilde{t}$.

$$BG(t) = \int_0^t BG(t, \tilde{t}) \, d\tilde{t} \qquad (5.13)$$

This integration cannot be solved analytically so a numerical approach must be followed.

Chapter 6

The wavelength dependence of tert-butyl nitrite surface photochemistry

Abstract *The surface photochemistry of tert-butyl nitrite adsorbed on Ag(111) was investigated at 532 and 266 nm. The desorbing molecules were detected in time of flight (TOF) mode by a mass spectrometer. Irradiation of the adsorbates leads to desorption of NO at both wavelengths. At all wavelengths caging and bimodal NO TOF distributions, consisting of a hyperthermal and a thermal component, are observed. At 532 nm dissociation is governed by a direct excitation with a cross section of 2×10^{-21} cm^2. This is contradicting the general belief in gas phase photochemistry that alkyl nitrites do not dissociate at this wavelength. The small cross section for dissociation at 532 nm is likely the reason of this belief. The observed TOF distributions at 266 nm are very similar to the 355 nm results, although generally higher translational energies and cross section values were measured. At 266 nm dissociation proceeds via a direct excitation. The results are consistent with an excitation into the S$_1$ state at 355 nm and excitation into the S$_2$ state at 266 nm.*

6.1 Introduction

Recently we have investigated the surface photochemistry of tert-butyl nitrite adsorbed on Ag(111) at 355 nm[26,43]. As one of the conclusions we proposed that dissociation proceeded via the same excitation mechanism as in the gas phase. In this article we will report on the photochemistry at other wavelengths (532 and 266 nm) in order to investigate whether the similarity in the excitation mechanism persists.

The coverage dependence of the surface photochemistry yields important in-

formation on the excitation mechanism[104,105]. This information was used to determine the dissociation mechanism at 355 nm[26,43]. But beside the coverage dependence, also the wavelength dependence yields important information. If dissociation is governed by a direct excitation, a photon resonance will be observed as is shown for $Mo(CO)_6$ adsorbed on $Ag(111)$[94]. A substrate mediated dissociation process will show as a function of photon energy a monotonically increasing cross section and a fairly constant energy distribution of the photoproducts[11,13,106]. Since we use the harmonics of a Nd:YAG laser to induce photochemistry, the wavelength dependence is only studied at 532, 355 and 266 nm. Despite of the fact that a continuous scan of wavelength is preferred, we will show that this limited set of wavelengths already reveals interesting phenomena.

The gas phase dissociation of alkyl nitrites (RONO) is investigated in the visible and UV range[67–83]. These studies show a minor importance of the R-group in alkyl nitrites (RONO). Between 300 and 400 nm dissociation into NO and an alkoxy proceeds via the predissociative S_1 state, which has a life time of 125 fs[79]. At wavelengths shorter than 300 nm, dissociation via a direct dissociative S_2 state results in the same dissociation products[72,75]. The cross sections for dissociation via the S_2 state are typically one order of magnitude larger as for dissociation via the S_1 state[95]. The energy content of the NO photoproduct is larger for dissociation via the S_2 state compared to dissociation via the predissociative S_1 state (1.0 eV compared to 0.5 eV)[69,81]. The cross sections in the 300 to 400 nm region show a vibrational progression due to the simultaneous excitation of the N=O stretch in the alkyl nitrite[79]. At wavelengths longer than 400 nm most papers report that no dissociation is present. This conclusion is based upon the sharp decrease in optical absorption of the gas phase molecule going from the S_1 excitation region to longer wavelengths. However, no systematic study on the upper limit of a possible dissociation cross section in the visible has been performed. One article does report a preliminary observation of dissociation of tert-butyl nitrite down to 500 nm[107].

Tert-butyl nitrite adsorbs without any appreciable dissociation on $Ag(111)$ and forms a monolayer and multilayer structure for temperatures lower than 110 K[86]. The monolayer desorbs at 160 K and the multilayer at 120 K. The sticking coefficient is coverage independent. A coverage scale in terms of monolayers adsorbed could be extracted from the observed saturation of the monolayer TDS peak. This saturation occurred for an exposure of 8×10^{-6} mbar s. Upon irradiation with 355 nm photons adsorbed tert-butyl nitrite photodissociates and yields NO molecules[26,43]. In TOF measurements two NO desorption distributions are observed. Cross section measurements reveal that both distributions are formed by the same dissociation process and that the slow NO distribution consists of molecules from the fast NO component that were thermalized by the silver substrate. This thermalization of NO photoproducts by the substrate is only possible if the NO molecule is produced in either the first or second adsorbed layer. Therefore the thermal component saturates at a coverage of 2 ML. The hyperthermal component also saturates, but this occurs at a coverage of 5 ML. Caging in the film causes this saturation. For larger coverages only the

top five layers produce hyperthermal NO, more inward layers are incapable in producing photoproducts due to caging of the surrounding molecules[43]. In the first adsorbed layer at the surface caging is not preventing dissociation. Caging does allow for isomerization from *trans* tert-butyl nitrite to *cis* tert-butyl nitrite as is observed in RAIRS. For coverages as large as 50 ML the outermost layers still photodissociate. A direct excitation mechanism is responsible for dissociation in the multilayer regime. In the monolayer the cross section is the same as in the multilayer and therefore dissociation is believed to proceed in the monolayer via the same direct excitation mechanism. At 351 nm photodissociation of tert-butyl nitrite at MgF_2 has been studied, both with rotational resolution of the NO and TOF analysis of the NO photoproduct[61,62]. Although the former experiment suggest that two desorption channels were active, this could not be seen in the TOF measurements. The wavelength depandence of methyl nitrite, CH_3ONO, at Ag(111) has been studied by Pressley and coworkers in the 400-254 nm range[19]. These authors found that photodissociation was mainly a direct process and that roughly the wavelength dependence of the gas phase cross section was found for the photodissociation. Bimodal velocity distributions with a thermal and hyperthermal component were observed. The thermal component was more pronounced for longer wavelengths.

6.2   Experimental

The experiments are performed in an ultra-high vacuum (UHV) system with the following analytical tools: thermal desorption spectroscopy (TDS), low energy electron diffraction (LEED), X-ray photoelectron spectroscopy (XPS), Auger electron spectroscopy, reflection absorption infrared spectroscopy (RAIRS) and quadrupole mass spectrometry with time of flight (TOF) detection. The system has a base pressure of 2×10^{-10} mbar and is described in more detail elsewere[39,25].

The Ag(111) crystal was polished to give a misalignment of less than 0.1° and has a diameter of 10 mm. The crystal can be cooled to 85 K by using liquid nitrogen and heated to 1000 K by electron bombardment. The electrons have an energy of 400 eV and originate from a hot filament behind the crystal. The temperature is measured by a chromel alumel thermocouple inserted in a hole in the side of the crystal. The crystal is cleaned by cycles of sputtering with 800 eV argon ions at 650 K and annealing at 800 K. Crystal cleanliness was checked by XPS and LEED.

The tert-butyl nitrite, $(CH_3)_3CONO$ was supplied by Aldrich with a specified purity of 96%. The nitrite was stored in a stainless steel container and freeze-pump-thawed several times before introduction into the vacuum system. The crystal was exposed at 85 K to tert-butyl nitrite by backfilling the chamber for typically a few minutes. From the mass spectrometer signal during dosing, an accurate exposure is calculated by a method described elsewere[25]. After dosing the crystal, the base pressure was allowed to return to its normal value.

A picosecond Nd:YAG laser from Quantel was used to irradiate the sample. The laser produced pulses with a wavelength of 1064 nm at a repetition rate of 10 Hz. The pulses had a maximum energy of 55 mJ and a temporal width of 30 ps (full width at half maximum, FWHM). Using a BBO crystal the fundamental (1064 nm, 1.17 eV) was doubled to give 2.3 eV photons (532 nm). Subsequent doubling in a KDP crystal yielded 4.7 eV photons (266 nm). Before the laser beam entered the vacuum system, a 4 mm pinhole was used to transmit the central part of the beam in order to get a uniform beam profile. For the experiments at 532 nm 5 mJ pulses were used and at 266 nm 0.8 mJ. Due to the positioning of the UV grade fused quarts viewports and the quadrupole mass spectrometer (QMS), light was incident on the crystal at an angle of 52.5°with the surface normal and was reflected out of the vacuum system through another viewport. The molecules detected by the QMS leave the surface with an angle of 7.5° from the normal. Light impinging on the surface was composed out of equal amounts of S and P polarized light.

The QMS was a Balzers 420 quadrupole mass spectrometer with a 90°off axis channeltron and a crossed beam ionizer. The channeltron was connected to a fast current amplifier that fed the pulses to a multi channel scaler (EG&G, turbo MCS). The spectra were recorded with a 15 μs resolution. The flight distance of the molecules from the surface to the ionizer of the QMS was 13.5 cm. After dosing, 6 TOF spectra were recorded in succession for respectively 400, 400, 400, 800, 1600, 3200 laser shots. In this way the exponentially decaying yield can be monitored and the cross section can be extracted. No significant changes were observed in the individual TOF spectra. By summing all the 6 spectra an accurate determination of the peak positions and peak areas is possible.

The TOF spectra are described by Maxwell-Boltzmann velocity distributions. The fit procedure will be described below, but for a more complete description see reference [43]. The equation used to fit the spectra is given by equation 6.1 and consists of a sum over N Maxwell-Boltzmann distributions, an offset and a time dependent background term.

$$ s(t_{\mathrm{MCS}}) = y_0 + \sum_{i=1}^{N} \left(\frac{c_i}{t_{\mathrm{MCS}} - t_0} \right)^4 \exp \left(- \left(\frac{t_i}{t_{\mathrm{MCS}} - t_0} \right)^2 \right) + BG(t_{\mathrm{MCS}} - t_0) \quad (6.1) $$

In this equation t_{MCS} is the time between the laser shot and the detection of a pulse by the MCS. Parameter y_0 is the offset of the spectrum due to residual gas in the chamber. Parameter c_i is a normalization parameter for peak i and t_i determines the position of peak i. Time t_0 is the time between ionization of the molecule in the QMS and detection by the MCS. This is to correct t_{MCS} to yield the true time of flight from the crystal to the ionizer of the QMS. For NO t_0 was calculated to be 17 μs and was kept constant in the fitting procedure. The time dependent background term BG describes the pump tail caused by molecules that are trapped on the walls of the ionizer and other parts of the system. This background term was introduced because the TOF signal only returned to the normal background level after a few ms, whereas all the peaks occurred in the first half ms. For more detail on this topic see reference [26,43].

The flux-weighted mean translational energy $\langle E_{\text{trans}} \rangle$ and the characteristic translational temperature $\langle E_{\text{trans}}/2k \rangle$ can be calculated from the parameter t_i by equation 6.2.

$$\langle E_{\text{trans}}/2k \rangle = \frac{\langle E_{\text{trans}} \rangle}{2k} = \frac{ml^2}{2kt_i^2} \tag{6.2}$$

In this equation k is Boltzmann's constant, m the mass of the desorbing molecule and l the distance from the crystal to the ionizer of the QMS.

From the parameters c_i and t_i a quantity Y can be extracted that is proportional to the total amount of molecules desorbing into the direction of the mass spectrometer (equation 6.3). This quantity will be referred to as the yield. This yield takes the velocity dependent detection probability of the QMS into account and does only depend on the experimental geometry used. But since the experimental geometry is not changed in the experiment Y is a very suitable measure for the yield of molecules desorbing into the direction of the QMS. Note that this yield is not angle integrated, so that a change in the angular desorption distribution leads to a different value of this yield. However, we believe that this effect is of minor importance in this study.

$$Y = \left(\frac{c_i}{t_i} \right)^4 \tag{6.3}$$

The cross section can be determined by calculating the yield of each of the six TOF spectra obtained from one dose by using equation 6.3. The cross section determination is based on the principle that the desorption rate of the molecule observed in TOF decays as a single exponential decay as a function of photon dose. By plotting the integrated yield versus the accumulated photon dose in cm^{-2} the cross section can by extracted by fitting the plot to equation 6.4.

$$\int_0^F Ae^{-\sigma\tilde{F}} \, d\tilde{F} = \frac{A}{\sigma} \left(1 - e^{-\sigma F} \right) \tag{6.4}$$

For a more elaborate explanation of the cross section determination see reference [43].

6.3   Results

At a wavelength of 532 nm in the gas phase generally dissociation is said to be absent, but when we performed TOF measurements at 532 nm, to our surprise, we measured a signal for mass 30. By performing TOF measurements at other masses we concluded that NO was the only desorbing species. Decreasing the laser intensity by a factor two did not result in a different TOF spectrum and the yield appeared to be linear with intensity. The TOF spectra are bimodal and consist of a thermal and hyperthermal component. The spectra integrated over 6800 shots for a variety of coverages ranging from 0.3 to 8 ML due to 532 nm photons are plotted in the lower panel of figure 6.1. For all coverages two velocity

components are present. The peak position of the fast component remains more or less the same with coverage, whereas the position of the slow component seems to shift to larger times with increasing dose. However, the apparent shift of the slow component is partially due to the superposition of a fast and slow peak with changing relative areas. The relative ratios of the two components show a clear change with coverage. For a coverage of 0.3 ML there is more fast than slow, whereas this ratio is the opposite for higher coverages. For coverages of 2 ML and higher the spectra do not seem to change much, although a slight increase in the amount of slow NO might be present.

At 266 nm (the fourth harmonic of the laser) also TOF spectra were measured. The TOF spectra integrated over 6800 laser shots for several coverages are plotted in the upper panel of figure 6.1. The spectra and trends are very similar to the 355 nm results[26]. Two components are present in the TOF spectra for all coverages. For high coverages the fast peak dominates over the slow. In the monolayer regime the ratio between the fast and slow component does not change, only for coverages higher than 1 ML does the fast peak increase more than the slow. The spectra do not seem to change for coverages higher than 4 ML, nor in yield nor in peak positions.

The TOF spectra for 532 nm and 266 nm are both bimodal for all coverages and the peak positions of the distributions are also very similar. However, the relative ratios between the two components and the trend with coverage are completely different. Whereas for submonolayer coverages the spectra do resemble each other, for increasing coverage they show the opposite trend. For high coverages at 266 nm the fast component dominates and at 532 nm the slow component dominates.

To deduce any trends with coverage it is better to decompose the two components by fitting. Because of the overlap of the two components and due to the velocity dependent detection probability of the mass spectrometer, trends could be misinterpreted. Fitting all TOF spectra after 6800 laser shots for different coverages with equation 6.1 yielded the parameters c_i and t_i. From these parameters the average translational energy $\langle E_{\text{trans}}/2k \rangle$ and the yield Y are deduced by using equation 6.2 and 6.3. The uncertainties in the yield and in the translational energy are given by standard errors derived from the standard errors of the fit parameters c_i and t_i.

The average translational energy expressed in K for coverages up to 10 ML are plotted in figure 6.2 for both the fast and slow component. In the upper panel the 266 nm results are shown and in the lower panel the 532 nm results. The slow component at 532 nm shows a slight decrease in the monolayer regime from 150 K to 100 K. For larger coverages the energy remains about 100 K. This energy is very comparable to the substrate temperature of 85 K and therefore, similar to the 355 nm, we assume that at 532 nm some of the NO photoproducts get thermalized. The fast component shows a slight decrease in average translational energy in the monolayer regime as well. Generally the energy is about 800–900 K and shows no significant change with coverage.

For the slow component at 266 nm a translational temperature is measured
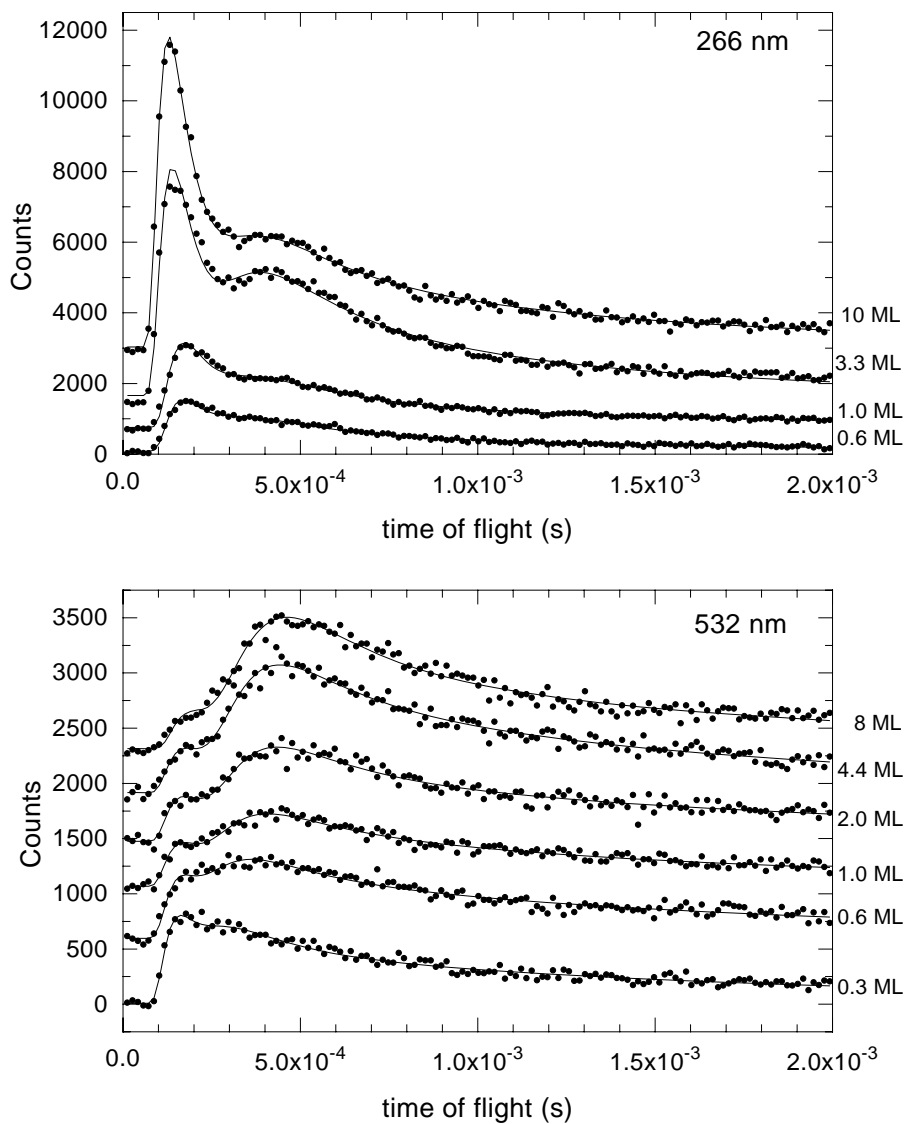
Figure 6.1: *TOF spectra of desorbing NO due to photodissociation of tert-butyl nitrite adsorbed on Ag(111) for various coverages. The upper panel shows the results for dissociation at 266 nm and the lower panel shows the results for 532 nm. For both wavelengths bimodal distributions are observed, but the trends are very different.*
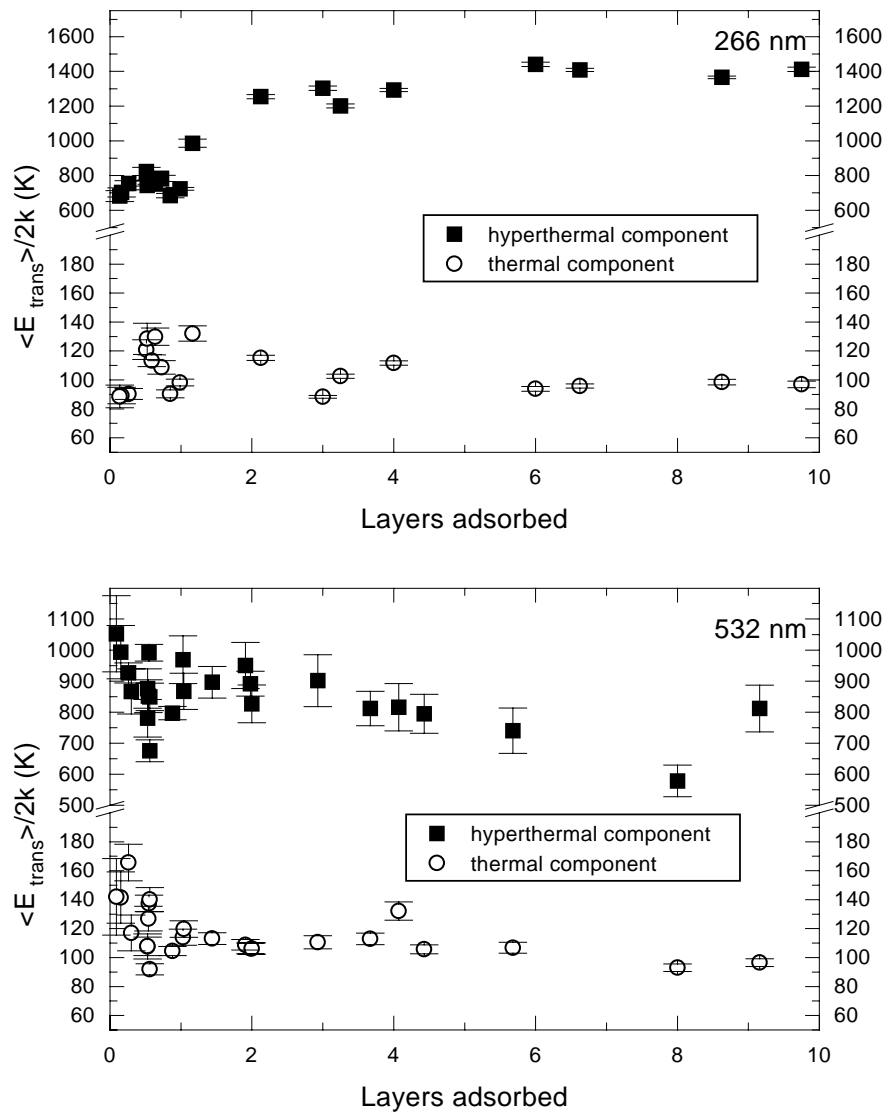
Figure 6.2: *Mean translational energy expressed in K of the desorbing NO distributions as a function of coverage due to 532 and 266 nm irradiation from a 85 K silver substrate. At 532 nm a slight decrease in energy can be observed in the monolayer regime, but at higher coverages not dependence is present. At 266 nm the slow component shows no dependence with coverages. The fast component has a constant energy in the monolayer of about 750 K that increases to 1450 K for a coverage of 5 ML.*

that matches the substrate temperature. So, similar to the results at 532 and 355 nm, also at 266 nm an efficient thermalization process exists. If, similar to the 355 nm results, the cross sections for the slow and fast distribution are the same, a single dissociation mechanism is present. That this is the case will be shown below. The hyperthermal component has a constant energy of about 750 K in the monolayer regime. Between 1 and 5 ML the energy increases to 1450 K and above 5 ML the energy is constant again. This behavior is also observed at 355 nm, although there the energy in the monolayer was 600 K and above 5 ML it was 1000 K. An intriguing observation is that although the excess energy (photon energy minus dissociation energy) of the photons at 532 and 266 nm differ by a factor 6 (0.5 and 2.9) the translational energies are very comparable in the monolayer regime.

The yield at 532 nm between a coverage of 0 and 1 ML shows a linear increase with coverage for both components (lower panel of figure 6.3). Within the monolayer the yields of the thermal and hyperthermal component are comparable. At a coverage of 1 ML the hyperthermal component saturates and the thermal component increases only slightly. At a coverage of 5 ML also the thermal component seems to have saturated, however the large uncertainty in the data precludes a firmer conclusion. The slight increase of the slow component above 1 ML coverage could originate from a conversion of fast NO to slow NO. But certainly, the increase in yield observed in the monolayer does not persist beyond 1 ML.

The yield at 266 nm of both components is plotted in the upper panel of figure 6.3. Just as with the behavior of the translational energy, also the behavior of the yield is very similar to the 355 nm results. The thermal component saturates around 2 layers and the hyperthermal component saturates at approximately 5 ML.

Using the procedure described in the experimental section, the cross section for both velocity components was measured as a function of coverage (figure 6.4). The cross section is determined by modeling the decaying desorption rate with a single exponential decay. Therefore this photodissociation cross section is actually an average over all tert-butyl nitrite molecules leading to NO desorption. This means that molecules that are not photoactive, for instance due to caging, do not influence this average cross section. The cross section at 532 nm shows no noticeable change with coverage for both components. The average cross section measures 5×10^{-21} cm^2 for the thermal component and 2×10^{-21} cm^2 for the hyperthermal component. However, this difference in cross section is not significant as becomes apparent if the ratio of the thermal and hyperthermal cross section is calculated. This ratio measures 1.5 ± 0.5 (value$\pm$standard deviation). Therefore, similar to the 355 nm results, the conclusion is made that the cross sections for the thermal and hyperthermal component are indistinguishable. This results in an average value of about 3×10^{-21} cm^2 (for comparison: at 355 nm a cross section of 3×10^{-20} cm^2 was found). The error bars in the plot are somewhat larger than those at 355 nm, because the small value of the cross section induces a larger uncertainty.

The cross sections for both the thermal and hyperthermal component at
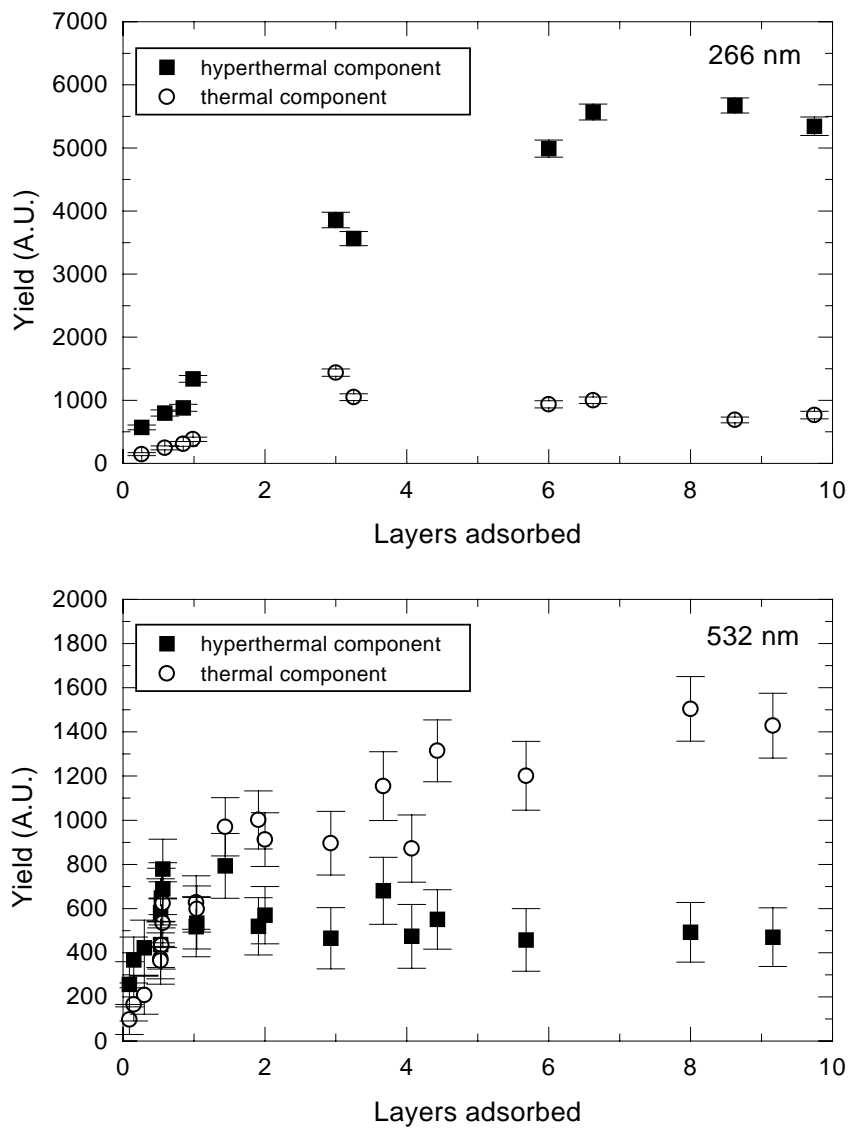
Figure 6.3: *Desorption yield of NO at 532 nm and 266 nm as a function of coverage for both components. The behavior at 266 nm is very similar to the 355 nm results. At 532 nm the fast component saturates at 1ML. The slow component increase only slightly above 1ML and saturates around 5 ML.*
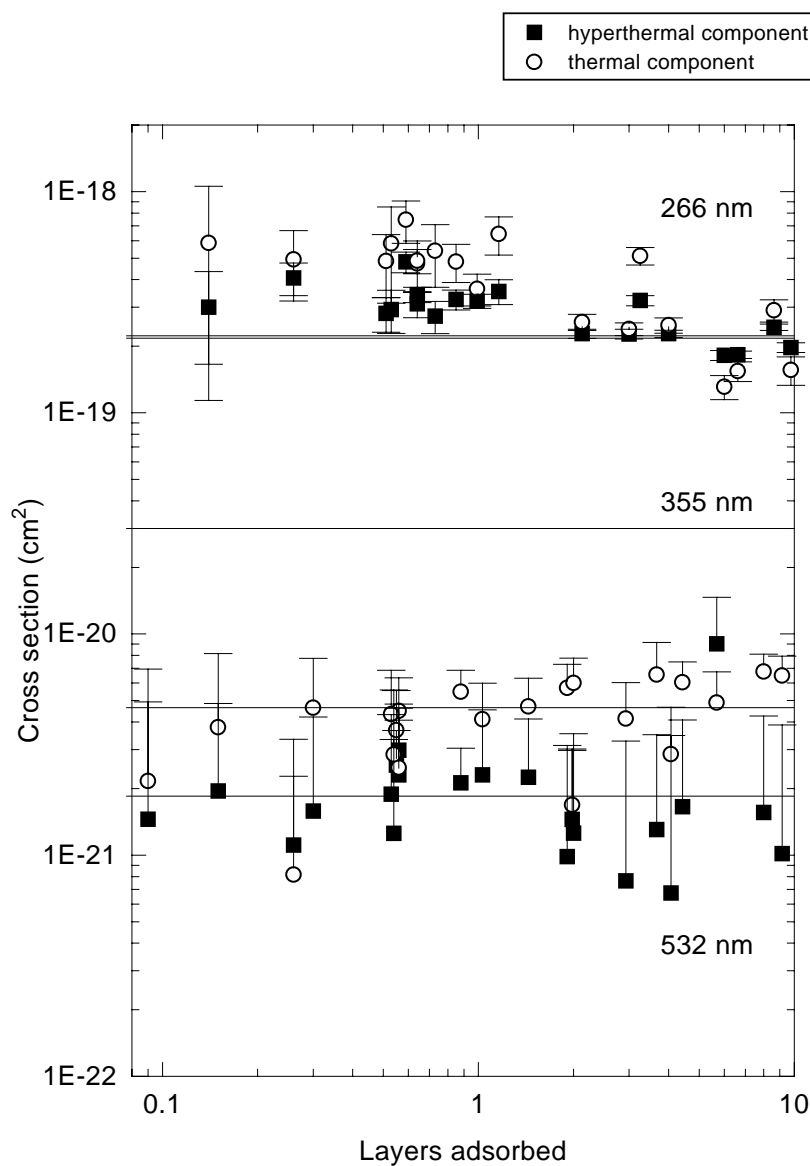
Figure 6.4: *Cross sections for both the thermal and hyperthermal component at 532 and 266 nm. At 532 nm the cross section is independent of coverage. Although the cross section for the thermal component appears to be higher than the hyperthermal cross section, this difference is not significant. At 266 nm the cross sections at low coverage have the tendency to be higher, but since the difference compared to the experimental uncertainty is small, a coverage independent cross section is assumed. For comparison the coverage independent cross section at 355 nm is show (3×10^{-20} cm^2). For clarity, at 532 nm only the upper part of the error bars are shown.*

266 nm are in the 10^{-19} range. For submonolayer coverages the cross sections have the tendency to be slightly higher than in the multilayer regime, but the standard deviations are also larger. If, analogues to previous results, a coverage independent cross section is assumed, a value of 2×10^{-19} cm^2 is obtained. This value is an order of magnitude larger than the cross section at 355 nm. The ratio between the cross sections for the hyperthermal and thermal component is 1.04 ± 0.04. This proves that the slow and fast component are produced by the same dissociation process.

Since the photochemistry at 532 nm has different characteristics than the photochemistry at 355 and 266 nm, a spacer layer experiment was conducted. As spacer layer methanol was used. Methanol adsorbed on Ag(111) experience no photochemistry up to wavelengths far into the UV[66]. Methanol multilayers desorb at 145 K[25]. These two features make that methanol can be used as spacer layer molecule. Another characteristic of methanol multilayers is that there are two phases, an amorphous and a crystalline phase[25]. Adsorption of methanol at temperatures lower than 100–110 K results in an amorphous overlayer. Annealing of this layer for 2 minutes at 120 K causes the conversion into a crystalline phase. The crystalline phase of methanol has been used in the spacer layer experiments, because diffusion of tert-butyl nitrite into the spacer layer is believed to be smaller for this phase.

We have performed spacer layer experiments with 10, 20 and 50 ML of crystalline methanol and 1 ML of tert-butyl nitrite adsorbed on top. For all spacer layer thicknesses identical TOF curves were measured. The result for a 20 ML thick methanol spacer layer is shown in figure 6.5. The TOF curves obtained from the spacer layer experiment resemble the TOF trace without spacer layer (figure 6.1) both in yield, peak position and ratio of the two components. A detailed analysis shows that the spacer layer experiment systematically results in 20% less NO relative to the 1 ML experiment without spacer layer. Also the slow component of the spacer layer experiment is somewhat faster. These two small differences with the 1 ML coverage without spacer layer causes the spacer layer experiment to match even better with a 0.8 ML coverage without spacer layer. Thus, although one monolayer is adsorbed, effectively 20% less seems to be adsorbed.

6.4 Discussion

6.4.1 Photochemistry at 266 nm

The cross section of the slow and fast component at 266 nm are indistinguishable, therefore we believe that the two components are formed by the same dissociation mechanism. After dissociation of the tert-butyl nitrite some NO molecules leave the surface with hyperthermal speed and some NO molecules are thermalized before they can desorb and leave the surface with thermal speed. That the slow component consists of thermalized molecules has been shown for dissociation
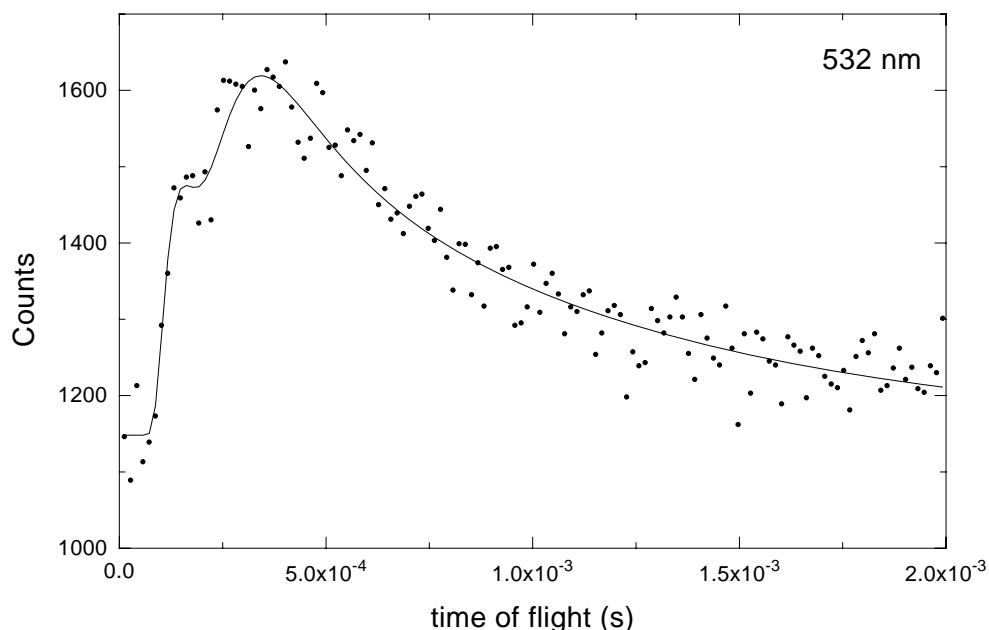
Figure 6.5: *TOF spectrum of 1 ML of tert-butyl nitrite on a 20 ML thick methanol spacer layer upon irradiation with 532 nm. The presence of a TOF signal shows that the silver substrate does not participate in the dissociation mechanism. The TOF trace resembles the spectrum obtained from 1 ML of tert-butyl nitrite without spacer layer.*

with 355 nm photons[26]: at this wavelength a correlation between the substrate temperature and the translational temperature of the slow component was measured. The absence of complete translational equilibration for the low rotational NO molecules from MgF_2[61,62] suggests that the metal is needed for complete thermalization. The stronger interaction of NO molecules with the metal compared to MgF_2 is believed to be the cause of this effect.

The yield of both components at 266 nm exhibit the same features as the yield at 355 nm[43]: the thermal component saturates at 1–2 ML and the hyperthermal component saturates at approximately 5 ML. At 266 nm at high coverage the hyperthermal component dominates the thermal component similar to the 355 nm results. Because of all these similarities we conclude that the observed saturation at 266 nm are there for the same reasons as at 355 nm. The thermal component saturates because only a dissociation event near the substrate can lead to subsequent trapping and thermalization by the substrate. Dissociation in the third layer and higher will not lead to subsequent thermalization by the substrate and therefore saturation of the thermal component at 1–2 ML is measured. The saturation of the hyperthermal component at 5 ML is caused by caging in the tert-butyl nitrite film. Only the five outermost layers are not caged strongly enough to inhibit dissociation. The fact that for large coverages still hyperthermal NO

is detected supports the conclusion that tert-butyl nitrite can dissociate in the outermost layers. This implies that hyperthermal NO is able to scatter through several layers without loosing most of its translational energy. For ions with a translational energy of a few electronvolts it is shown by the group of Madey that transmission through several layers of rare gasses or water is possible without significant loss of translational energy[88–90]. Therefore, the conclusion that NO photoproducts from a few layers deep can contribute to the hyperthermal component seems justified. Some loss of kinetic energy may be present, because the average translational energy of NO molecules from the top of the film is 0.25 eV compared to 1.0 eV in the gas phase at the same wavelength[69]. This also reveals that dissociation is caused by a direct excitation, because no substrate-mediated mechanism is able to dissociate molecules far away from the substrate. At 355 nm isomerization of the tert-butyl nitrite was observed by RAIRS and we infer that isomerization will also be present at 266 nm. For 355 nm complete conversion of all tert-butyl nitrite was observed in RAIRS up to the point were saturation of the fast component occurred (5 ML). Complete conversion is expected to be present at 266 nm for coverage up to 5 ML, but the RAIRS has not been carried out.

Above we have mentioned many similarities between the 355 and 266 nm results, but there are also differences. The translational energies at 266 nm are substantially higher. In the monolayer at 266 nm a translational temperature of 750 K was measured compared to 600 K at 355 nm. The multilayer results differ even more: 1450 K for 266 nm compared to 1000 K for 355 nm. Another difference is the magnitude of the cross sections. The cross section at 266 nm is an order of magnitude higher. This indicates that at 355 and 266 nm excitation into different excited states occurs. Also the difference in translational energy supports this. Dissociation at 355 nm in the gas phase and at the surface was believed to proceed via the S_1 state[43,79]. At 266 nm the present data is consistent with excitation into the direct dissociative S_2 state. This is also supported by the amount by which the cross section does increase going from 355 to 266 nm. In this study we measured an increase by a factor 7 going from 355 to 266 nm (increase from 3×10^{-20} to 2×10^{-19} cm^2). In the gas phase a increase of the same magnitude is measured (from 6×10^{-20} to 5×10^{-19} cm^2)[95]. This implies that if dissociation on silver at 266 nm proceeds via the S_2 state, the excited state is not quenched sufficiently to lower the cross section.

6.4.2   Photochemistry at 532 nm

The TOF spectrum observed at 532 nm for a coverage of one monolayer is not due to a minority of the adsorbed molecules, but is likely due to the entire adsorbed layer. This is apparent from a comparison of the TOF yields at 532 and 266 nm. The cross section measurements show that after 6800 shots of 24 mJcm^{-2} and 3.9 mJcm^{-2} for 532 and 266 nm respectively, the majority of the photoactive molecules have dissociated. For a coverage of 1 ML at 266 nm we concluded above that one complete monolayer could be converted. Comparing the yields at

1 ML for both wavelengths and realizing that in both cases the majority of the photoactive molecules have dissociated, it is concluded that also at 532 nm for a coverage of 1 ML a complete layer can be converted.

The observed TOF traces at 532 nm are not caused by substrate heating by the laser for the following reasons. At heating rates of 1 Ks^{-1} in TDS no thermal dissociation is observed, only desorption is present. At the much higher heating rates induced by the picosecond laser, desorption is generally favored over dissociation[108]. Since no laser-induced thermal desorption is observed, the observed dissociation is likely not to have a thermal origin. Besides this qualitative approach also a quantitative argument can be made. At the lowest intensity used only 0.5 mJcm^{-2} of energy is absorbed by the substrate. Calculations show that the temperature rise induced by these pulses is insufficient to desorb the tert-butyl nitrite molecule[109,110]. Thermal dissociation is even more improbable because the fast heating induced by the picosecond laser favors desorption.

From the linearity in the yield with intensity (not shown) we can conclude that dissociation at 532 nm is caused by a single photon excitation. The quantitatively different results for 532 nm and 266 nm excluded the possibility that at 532 nm dissociation is caused by minute amounts of fourth harmonic in the beam. The spacer layer experiments exclude a substrate-mediated mechanism. So, the conclusion must be that at 532 nm tert-butyl nitrite dissociation is caused by a direct excitation mechanism. This is in contrast to what is commonly assumed in the gas phase papers where generally dissociation in the visible is believed to be absent. A direct excitation mechanism at 532 nm is conceivable. Gas phase studies never investigated the upper limit of a possible dissociation cross section in the visible. If an estimation is made of this upper limit from available absorption spectra[76,111], a value low into the 10^{-21} decade is obtained. The value of 3×10^{-21} cm^2 found in this study is consistent with this upper limit. For HONO, a molecule with the same functional group and a very similar absorption structure in the 300–400 nm regime, dissociation into NO and HO was found down to 585 nm[112,113]. This finding also indicates that a direct channel at 532 nm is conceivable. Dissociation at 532 nm is also possible from an energetic point of view. At 532 nm the 2.3 eV photons exceed the dissociation energy of 1.8 eV. The remaining 0.5 eV is more than sufficient to provide 0.15 eV translational energy to the NO photoproduct.

The spacer layer experiment and the yield measurement (figure 6.3 and 6.5) show that for high coverages, dissociation mainly occurs in the top layer of the film. More inward layers are incapable in producing NO. That hyperthermal NO is still observed at high coverages also shows that only in the outermost layer dissociation is possible. Caging is very likely the cause of the absence of dissociation in the inner multilayers.

In the monolayer regime the ratio between hyperthermal and thermal NO at 532 nm is very similar to the ratio at 355 nm (see for example the TOF spectra). This indicates that at both wavelengths thermalization by the substrate occurs. The translational energy of the thermal component in the submonolayer regime is not completely thermal as is apparent by the elevated values compared to the sub-

strate temperature (figure 6.2). With completion of the monolayer the degree of thermalization increases. This suggests that scattering of NO molecules with adsorbates also increases the degree of thermalization. Comparison with the results obtained at MgF_2 shows that the Ag(111) substrate is instrumental in separating the two contributions. For higher coverages things appear to be different. At 532 nm the spacer layer experiments prove that NO is also thermalized in the top of the tert-butyl nitrite film. Also the ratio between hyperthermal and thermal NO changes drastically with coverage. This all points towards another thermalization mechanism in the film. The question arises why this thermalization mechanism is not present at 355 nm. A possible explanation is that dissociation at 355 nm proceeds via a different state and that therefore thermalization in the top of the film is absent. Another explanation is that, although a molecule in the outermost layer is not completely surrounded by other molecules, weak caging is already present and that therefore mainly thermal NO is formed.

6.5   Conclusions

Dissociation of tert-butyl nitrite at 266 nm results in higher translational energies, compared to dissociation at 355 nm. The cross section at 266 nm is an order of magnitude higher than at 355 nm and a direct excitation mechanism is responsible for dissociation. This is consistent with an excitation into the direct dissociative S_2 state at 266 nm. But although dissociation at 355 and 266 nm proceed via different states, the characteristics are very similar. In both cases NO is the only desorbing product and part of the NO is trapped and thermalized by the substrate. Caging is preventing dissociation in the multilayer for both wavelengths.

At 532 nm dissociation via a direct excitation is observed with a cross section of 3×10^{-21} cm^2. Because of this conclusion, the presence of dissociation in the gas phase at this wavelength should be reinvestigated. At 532 nm on Ag(111) also a hyperthermal and a thermal NO desorption distribution are measured. In addition to thermalization by the substrate, also another thermalization mechanism is present in the top of the film.

References

[1] P. Ball, *Windows, clean thyself*, Science 377 (1995), page 290.

[2] R. Wang, K. Hashimoto, A. Fujishima, M. Chikuni, E. Kojima, A. Kitamura, M. Shimohigoshi and T. Watanabe, *Light-induced amphiphilic surfaces*, Science 388 (1997), pages 431–432.

[3] I. E. Wachs and R. J. Madix, *The oxidation of methanol on a silver (110) catalyst*, Surf. Sci. 76 (1978), pages 531–558.

[4] T. E. Felter, W. H. Weinberg, G. Ya. Lastushkina, P. A. Zhdan and G. K. Boreskov, *The adsorption of methanol on Ag(111) and its reaction with preadsorbed oxygen*, Appl. of Surf. Sci. 16 (1983), pages 351–365.

[5] W. S. Sim, P. Gardner and D. A. King, *Structure and reactivity of the surface methoxy species on Ag(111)*, J. Phys. Chem. 99 (1995), pages 16002–16010.

[6] B. A. Sexton, *Methanol decomposition on platinum (111)*, Surf. Sci. 102 (1981), pages 271–281.

[7] J. C. Polanyi and A. H. Zewail, *Direct observation of the transition state*, Acc. Chem. Res. 28 (1995), pages 119–132.

[8] S. Ogawa and H. Petek, *Femtosecond dynamics of hot-electron relaxation in Cu(111) and Cu(100)*, Surf. Sci. 357–358 (1996), pages 585–594.

[9] P. Avouris and R. E. Walkup, *Fundamental mechanisms of desorption and fragmentation induced by electronic transitions at surfaces*, Annu. Rev. Phys. Chem. 40 (1989), pages 173–206.

[10] E. Hasselbrink, *Mechanisms in photochemistry on metal surfaces*, Appl. Surf. Sci. 80 (1994), pages 34–40.

[11] X.-Y. Zhu, *Surface photochemistry*, Annu. Rev. Phys. Chem. 45 (1994), pages 113–144.

[12] W. Ho, *Surface photochemistry*, Surf. Sci. 299 (1994), pages 996–1007.

[13] W. Ho, *Femtosecond laser-induced dynamical quantum processes on solid surfaces (DQPSS)*, Surf. Sci. 363 (1996), pages 166–178.

[14] S. A. Buntin, L. J. Richter, D. S. King and R. R. Canvanagh, *State resolved evidence for hot carrier driven surface reactions: Laser-induced desorption of NO from Pt(111)*, J. Chem. Phys. 91 (1989), pages 6429–6446.

[15] E. Hasselbrink, S. Jakubith, S. Nettesheim, X. Y. Zhu, M. Wolf and A. Cassuto, *Cross sections and NO product state distributions resulting from substrate mediated photodissociation of NO_2 adsorbed on Pd(111)*, J. Chem. Phys. 92 (1990), pages 3154–3169.

[16] Z. J. Sun, S. Gravelle, R. S. Mackay, X. Y. Zhu and J. M. White, *Hot carrier induced photodesorption dynamics of SO_2 from Ag(111)*, J. Chem. Phys. 99 (1993), pages 10021–10033.

[17] K. Fukutani, Y. Murata, R. Schwarzwald and T. J. Chuang, *UV-laser-induced desorption of NO from Pt(111)*, Surf. Sci. 311 (1994), pages 247–256.

[18] W. Nessler, K. H. Bornscheuer, M. Binetti and E. Hasselbrink, *Quantum-state-resolved investigation of the UV photodesorption of NH_3*, Surf. Sci. 352 (1996), pages 189–194.

[19] L. A. Pressley, E. D. Pylant and J. M. White, *Surface chemistry of methyl nitrite on Ag(111): Thermal and non-thermal processes*, Surf. Sci. 367 (1996), pages 1–19.

[20] T. Yamada, T. Misono, K. I. Tanaka and Y. Murata, *A new type of experimentation designed for the study of chemical reactions on single-crystal surfaces*, J. Vac. Sci. Techn. A 7 (1989), pages 2808–2812.

[21] P. H. F. Reijnen, U. van Slooten, A. P. de Jongh, J. H. M. Kuijper and A. W. Kleyn, *A system for high pressure preparation and UHV characterization of surface reactions*, Meas. Sci. Technol. 1 (1990), pages 1244–1246.

[22] K. E. Keck and B. Kasemo, *UHV-compatible reaction cell for combined high and low-pressure studies of surface reactions*, Rev. Sci. Instrum. 54 (1983), pages 574–578.

[23] R. Ravel, M. A. Harrison and D. A. King, *A new ultrahigh vacuum single crystal sample transfer system with direct temperature control and measurement*, J. Vac. Sci. Techn. A 9 (1991), pages 345–349.

[24] A. Raukema, A. P. de Jongh, H. P. Alberda, R. Boddenberg, F. G. Giskes, E. de Haas, A. W. Kleyn, H. Neerings, R. Schaafsma and H. Veerman, *A three axis goniometer in an UHV molecular beam experiment*, Meas. Sci. Technol. 8 (1997), pages 253–261.

[25] H. G. Jenniskens, P. W. F. Dorlandt, M. F. Kadodwala and A. W. Kleyn, *The adsorption of methanol on Ag(111) studied with TDS and XPS*, Surf. Sci. 357–358 (1996), pages 624–628.

[26] H. G. Jenniskens, W. van Essenberg, M. Kadodwala and A. W. Kleyn, *The photodissociation of tert-butyl nitrite adsorbed on Ag(111): Bimodal velocity distributions of the photoproducts*, Chem. Phys. Lett. 268 (1997), pages 7–12.

[27] R. Zhang and A. J. Gellman, *Straight-chain alcohol adsorption on the Ag(110) surface*, J. Phys. Chem. 95 (1991), pages 7433–7437.

[28] Q. Dai and A. J. Gellman, *A HREELS study of $C_1 - C_5$ straight-chain alcohols on clean and pre-oxydized Ag(111) surfaces*, Surf. Sci. 257 (1991), pages 103–112.

[29] B. A. Sexton and A. E. Hughes, *A comparison of weak molecular adsorption of organic molecules on clean copper and platinum surfaces*, Surf. Sci. 140 (1984), pages 227–248.

[30] M. Bowker and R. J. Madix, *XPS, UPS and thermal desorption studies of alcohol adsorption on Cu(110)*, Surf. Sci. 95 (1980), pages 190–206.

[31] A. Peremans, F. Maseri, J. Darville and J. -M. Gilles, *Infrared characterization of methanol adsorbed on Cu(110)*, J. Vac. Sci. Techn. A 8 (1990), pages 3224–3228.

[32] J. N. Russel, Jr., S. M. Gates and J. T. Yates, Jr., *Reaction of methanol with Cu(111)+O(ads)*, Surf. Sci. 163 (1985), pages 516–540.

[33] B. A. Sexton, K. D. Rendulic and A. E. Hughes, *Decomposition pathways of $C_1 - C_4$ alcohols adsorbed on platinum (111)*, Surf. Sci. 121 (1982), pages 181–198.

[34] K. D. Rendulic and B.A. Sexton, *Adsorption and dehydrogenation of alcohols and ethers in platinum (111)*, J. Cat. 78 (1982), pages 126–135.

[35] G. A. Attard, K. Chibane, H. D. Ebert and R. Parsons, *The adsorption and decomposition of methanol on Pt(110)*, Surf. Sci. 224 (1989), pages 311–326.

[36] K. Christmann and J. E. Demuth, *The adsorption and reaction of methanol on Pd(100). I. chemisorption and condensation*, J. Chem. Phys. 76 (1982), pages 6308–6317.

[37] S. R. Bare, J. A. Stroscio and W. Ho, *Characterization of the adsorption and decomposition of methanol on Ni(110)*, Surf. Sci. 150 (1985), pages 399–418.

[38] A. A. Deckert, J. L. Brand, C. H. Mak, B. G. Koehler and S. M. George, *The decomposition of methanol on Ru(100) studied using laser induced thermal desorption*, J. Chem. Phys. 87 (1987), pages 1936–1947.

[39] H. G. Jenniskens, A. Bot, P. W. F. Dorlandt, W. van Essenberg, E. de Haas and A. W. Kleyn, *An ultra-high vacuum (UHV) apparatus to study the interaction between adsorbates and photons*, Meas. Sci. Technol. 8 (1997), pages 1313–1322.

[40] D. H. Ehlers, A. Spitzer and H. Lüth, *The adsorption of methanol on Pt(111), An IR reflection and UV photoemission study*, Surf. Sci. 160 (1985), pages 57–69.

[41] A. Peremans, F. Maseri, J. Darville and J. -M. Gilles, *Interaction of methanol with a polycrystaline platinum surface studied by infrared reflextion absorbtion spectroscopy*, Surf. Sci. 227 (1990), pages 73–78.

[42] P. Redhead, Vacuum 12 (1962), page 203.

[43] H. G. Jenniskens, L. Philippe, W. van Essenberg, M. Kadodwala and A. W. Kleyn, *Tert-butyl nitrite surface photochemistry on Ag(111), The transition from submonolayer to multilayer behavior*, Submitted to J. Chem. Phys.

[44] P. Tarte, *Rotational isomerism as a general property of alkyl nitrites*, J. Chem. Phys. 20 (1952), pages 1570–1575.

[45] M. Bodenbinder, S. E. Ulic and H. Willner, *A gas-phase and matrix isolation study of the equilibrium CH_3ONO (Cis) $\rightleftharpoons CH_3ONO$ (Trans) by FTIR spectroscopy*, J. Phys. Chem. 98 (1994), pages 6441–6444.

[46] A. J. Barnes, H. E. Hallam, S. Waring and J. R. Armstrong, *Cryogenic photolysis studies, part 2.-infrared spectrum of nitrosomethane monomer*, Faraday Trans. II 72 (1976), pages 1–10.

[47] M. E. Jacox and F. L. Rook, *Photodecomposition of methyl nitrite trapped in solid argon*, J. Phys. Chem. 86 (1982), pages 2899–2904.

[48] B. A. Sexton and A. E. Hughes, *A comparison of weak molecular adsorption of organic molecules on clean copper and platinum surfaces*, Surf. Sci. 140 (1984), pages 227–248.

[49] R. J. Speedy, P. G. Debenedetti, R. S. Smith, C. Huang and B. D. Kay, *The evaporation rate, free energy, and entropy of amorphous water at 150 k*, J. Chem. Phys. 105 (1996), pages 240–244.

[50] L. Q. Jiang and B. E. Koel, *Hydrocarbon trapping and condensation on Pt(111)*, J. Phys. Chem. 96 (1992), pages 8694–8697.

[51] J. Pawela-Crew and R. J. Madix, *Lateral interactions in the desorption kinetics of weakly adsorbed species: Unexpected differences in the desorption of C_4 alkenes and alkanes from Ag(110) due to oriented π-bonding of the alkenes*, Surf. Sci. 339 (1995), pages 8–22.

[52] D. E. Brown, S. M. George, C. Huang, E. K. L. Wong, K. B. Rider, R. S. Smith and B. D. Kay, *H_2O condensation coefficient and refractive index for vapor-deposited ice from molecular beam and optical interference measurements*, J. Phys. Chem. 100 (1996), pages 4988–4995.

[53] F. Budde, T. F. Heinz, M. M. T. Loy, J. A. Misewich, F. de Rougemont and H. Zacharias, *Femtosecond time-resolved measurement of desorption*, Phys. Rev. Lett. 66 (1991), pages 3024–3027.

[54] W. D. Mieher and W. Ho, *Bimolecular surface photochemistry - mechanisms of CO oxidation on Pt(111) at 85 k*, J. Chem. Phys. 99 (1993), pages 9279–9295.

[55] A. Peremans, K. Fukutani, K. Mase and Y. Murata, *CO and CO^+ photodesorption from Pt(111) at 193 nm*, Phys. Rev. B 47 (1993), pages 4135–4138.

[56] P. M. Chu, S. A. Buntin, L. J. Richter and R. R. Cavanagh, *Photodesorption dynamics of CO from Si(111): The role of surface defects*, Surf. Sci. 321 (1994), pages 127–132.

[57] M. Wolf, E. Hasselbrink, J. M. White and G. Ertl, *The adsorbate state specific photochemsitry of dioxygen on Pd(111)*, J. Chem. Phys. 93 (1990), pages 5327–5336.

[58] I. Kusunoki, M. Sakashita, T. Takaoka and H. Range, *Photodissociation and desorption of multilayer acetone on a Si(100) surface by 193 nm laser irradiation*, Surf. Sci. 357–358 (1996), pages 693–697.

[59] Z. J. Sun, A. L. Schwaner and J. M. White, *Charge transfer reaction at surfaces: CF_3I on Ag(111)*, J. Chem. Phys. 103 (1995), pages 4279–4291.

[60] L. C. Giancarlo, B. C. Haynie, K. M. Miller, J. M. Reynolds, J. M. Rusnock and C. A. Baumann, *Spectra and photochemistry of trifluornitrosomethane adsorbed on alkali halide films*, J. Phys. Chem. 100 (1996), pages 15539–15550.

[61] C. J. S. M. Simpson, P. T. Griffiths and M. Towrie, *The dynamics of the photolysis of alkyl nitrites from a dielectric surface. A comparison with gas phase results*, Chem. Phys. Lett. 234 (1995), pages 203–208.

[62] C. J. S. M. Simpson, P. T. Griffiths, H. L. Wallaart and M. Towrie, *Photodissociation of alkyl nitrites adsorbed on a MgF_2 surface. Rotational and translational energy distributions of product $NO(\nu, j)$ molecules*, Chem. Phys. Lett. 263 (1996), pages 19–24.

[63] K. H. Junker and J. M. White, *Adsorption of NF_3 on Pt(111): Interactions with electrons and photons*, Surf. Sci. 382 (1997), pages 67–78.

[64] E. D. Pylant, K. H. Junker, G. Szulczewski, M. J. Hubbard and J. M. White, *Photon-driven chemistry of biacetyl on ag(111)*, J. Phys. Chem. B 101 (1997), pages 4803–4809.

[65] G. J. Szulczewski and J. M. White, *Thermal and photon-induced desorption of NH_3 and ND_3 from Ag(111)*, J. Vac. Sci. Techn. A 15 (1997), pages 1526–1530.

[66] X. L. Zhou, X. Y. Zhu and J. M. White, *Photochemistry at adsorbate/metal interfaces*, Surf. Sci. Report 13 (1991), pages 73–220.

[67] D. Schwartz-Lavi, I. Bar and S. Rosenwaks, *Rotational alignment and non-statistical λ doublet population in NO following $(CH_3)_3CONO$ photodissociation*, Surf. Sci. 76 (1978), pages 531–558.

[68] G. Inoue, M. Kawasaki, H. Sato, T. Kikuchi, S. Kobayashi and T. Arikawa, *Photodissociation of methyl nitrite : Angular distributions in one- and two-photon dissociations*, J. Chem. Phys. 87 (1987), pages 5722–5727.

[69] B. A. Keller, P. Felder and J. R. Huber, *Molecular beam photodissociation study of methyl nitrite in the near-ultraviolet region*, J. Phys. Chem. 91 (1987), pages 1114–1120.

[70] R. Lavi, D. Schwartz-Lavi, I. Bar and S. Rosenwaks, *Directional properties in photodissociation: A probe for the symmetry and geometry of excited states of dimethylnitrosamine and tert-butyl nitrite*, J. Phys. Chem. 91 (1987), pages 5398–5402.

[71] J. August, M. Brouard, M. P. Docker, C. J. Milne, J. P. Simons, R. Lavi, S. Rosenwaks and D. Schwartz-Lavi, *Photodissociation dynamics of tert-butyl nitrite S_2 and tert-butyl hydroperoxide at 248-250 nm*, J. Phys. Chem. 92 (1988), pages 5485–5491.

[72] D. Schwartz-Lavi and S. Rosenwaks, *Scalar and vectorial properties in the photodissociation of tert-butyl nitrite from the S_1 and S_2 states*, J. Chem. Phys. 88 (1988), pages 6922–6930.

[73] J. W. Winniczek, R. L. Dubs, J. R. Appling, V. McKoy and M. G. White, *A multiphoton ionization study of the photodissociation dynamics of the S_2 state of CH_3ONO*, J. Chem. Phys. 90 (1989), pages 949–963.

[74] C. S. Effenhauser, P. Felder and J. R. Huber, *Photodissociation of alkyl nitrites in a molecular beam. Primary and secondary reactions*, J. Phys. Chem. 94 (1990), pages 296–302.

[75] H. U. Sutter, U. Brühlmann and J. R. Huber, *Photodissociation of CH_3ONO by a direct and indirect mechanism*, Chem. Phys. Lett. 171 (1990), pages 63–67.

[76] M. Hippler, M. R. S. McCoustra and J. Pfab, *Structured absorption spectrum and vibrational state-selectivity in the photodissociation of methyl nitrite in the near-UV*, Chem. Phys. Lett. 198 (1992), pages 168–176.

[77] M. Hippler, F. A. H. Al-Janabi and J. Pfab, *Photodissociation of jet-cooled methyl and t-butyl nitrite near 380 nm*, Chem. Phys. Lett. 192 (1992), pages 173–178.

[78] E. Kades, M. Rösslein and J. R. Huber, *Photofragment yield spectra of methyl nitrite in a supersonic jet*, Chem. Phys. Lett. 209 (1993), pages 275–280.

[79] J. M. Mestdagh, M. Berdah, I. Dimicoli, M. Mons, P. Meynadier, P. d'Oliveira, F. Piuzzi, J. P. Visticot, C. Jouvet, C. Lardeux-Dedonder, S. Martrenchard-Barra, B. Soep and D. Solgadi, *Observation of an indirect pathway in the femtosecond study of alkyl nitrite photodissociation in the S_1 state*, J. Chem. Phys. 103 (1995), pages 1013–1023.

[80] M. Rösslein, E. Kades, K. Bergmann and J. R. Huber, *Alignment detected photofragment yield spectroscopy demonstrated by photodissociation of t-butyl nitrite on a supersonic jet*, Chem. Phys. Lett. 235 (1995), pages 242–246.

[81] E. Kades, M. Rösslein, U. Brühlmann and J. R. Huber, *Photodissociation of methyl nitrite CH_3ONO, butyl nitrite $(CH_3)_3CONO$, and the clusters $[CH_3ONO]_n$ and $[(CH_3)_3CONO]_n$*, J. Phys. Chem. 97 (1993), pages 989–996.

[82] E. Kades, M. Rösslein and J. R. Huber, *From monomers to clusters. photodissociation of tert-butyl nitrite $(CH_3)_3CONO$ and homogeneous $[(CH_3)_3CONO]_n$ clusters*, J. Phys. Chem. 98 (1994), pages 13556–13562.

[83] K. Bergmann and J. R. Huber, *Photoinduced bimolecular reactions in homogeneous $[CH_3ONO]_n$ clusters*, J. Phys. Chem. A 101 (1997), pages 259–267.

[84] T. K. Polovintsyna and V. S. Gurman, *Photolysis of alkyl nitrites in a solid phase. isomerisation and formation of molecular products*, High Energy Chem. 15 (1981), pages 349–355.

[85] R. P. Müller, P. Russegger and J. R. Huber, *Hydrogen-bonded complex between HNO and formaldehyde. Photolysis of methyl nitrite in an argon matrix*, Chem. Phys. 70 (1982), pages 281–290.

[86] H. G. Jenniskens, W. van Essenberg, M. Kadodwala and A. W. Kleyn, *The adsorption of tert-butyl nitrite on Ag(111)*, Submitted to Surf. Sci.

[87] F. M. Zimmermann and W. Ho, *Velocity distributions of photochemically desorbed molecules*, J. Chem. Phys. 100 (1994), pages 7700–7706.

[88] N. J. Sack, M. Akbulut and T. E. Madey, *Transmission of low energy (<10 eV) O^+ ions through several monolayer thick rare gas films*, Phys. Rev. Lett. 73 (1994), pages 794–797.

[89] M. Akbulut, N. J. Sack and T. E. Madey, *Low energy (<5 eV) F^+ and F^- ions transmission through condensed layers of water: Enhancement and attenuation processes*, Phys. Rev. Lett. 75 (1995), pages 3414–3417.

[90] M. Akbulut, N. J. Sack and T. E. Madey, *Elastic and inelastic processes in the interaction of 1-10 eV ions with solids: Ion transport through surface layers*, Surf. Sci. Report 28 (1997), pages 177–246.

[91] E. Kuipers, M. G. Tenner, M. E. M. Spruit and A. W. Kleyn, *Differential trapping probabilities and desorption of physisorbed molecules: Application to NO / Ag(111)*, Surf. Sci. 205 (1988), pages 241–268.

[92] R. S. Smith, C. Huang, E. K. L. Wong and B. D. Kay, *Desorption and crystallization kinetics in nanoscale thin films of amorphous water ice*, Surf. Sci. 267 (1996), pages L13–L18.

[93] P. Löfgren, P. Ahlström, D. V. Chakarov, J. Lausmaa and B. Kasemo, *Substrate dependent sublimation kinetics of mesoscopic ice films*, Surf. Sci. 267 (1996), pages L19–L25.

[94] S. K. So and W. Ho, *Resonant photodissociation of $Mo(CO)_6$ adsorbed on graphite and Ag(111)*, J. Chem. Phys. 95 (1991), pages 656–671.

[95] J. G. Calvert and J. M. Pitts, *Photochemistry*, Wiley, New York, 1966.

[96] K-H. Bornscheuer, W. Nessler, M. Binetti and E. Hasselbrink, *Isotope and quantum effects in vibrational state distributions of photodesorbed ammonia*, Phys. Rev. Lett. 78 (1997), pages 1174–1177.

[97] P. Norlander and J. C. Tully, *Energy shifts and broadening of excited hydrogen-atom levels in the vinicity of a metal surface*, Phys. Rev. Lett. 61 (1988), pages 990–993.

[98] H. M. van Pinxteren, C. F. A. van Os, R. M. A. Heeren, R. Rodink, J. J. C. Geerlings and J. Los, *Angular ≪selection rules≫ for the resonent population of $O^-(^2P)$ and $C^-(^4S)$ in grazing ion-surface collisions*, Europhys. Lett. 10 (1989), pages 715–719.

[99] Q. Liu, J. K. Wang and A. H. Zewail, *Femtosecond dynamics of dissociation and recombination in solvent cages*, Nature 346 (1993), pages 427–430.

[100] J. M. Papanikolas, V. Vorsa, M. E. Nadal, P. J. Campagnola, H. K. Buchenau and W. C. Lineberger, *I_2^- photodissociation and recombination dynamics in size-selected $I_2^-(CO_2)_n$ cluster ions*, J. Chem. Phys. 99 (1993), pages 8733–8750.

[101] R. Parson and J. Faeder, *Ultrafast reaction dynamics in molecular cluster ions*, Science 276 (1997), pages 1660–1661.

[102] B. Jefferys Greenblatt, M. T. Zanni and D. M. Neumark, *Photodissociation of $I_2^-(Ar)_n$ clusters studied with anion femtosecond photoelectron spectroscopy*, Science 276 (1997), pages 1675–1678.

[103] C. J. Pouchert, *The Aldrich Library of FT-IR Spectra*, Aldrich Chemical Company, INC., Milwaukee, Wisconsin, 1985.

[104] E. P. Marsh, M. R. Schneider, T. L. Gilton, F. L. Tabares, W. Meier and J. P. Cowin, *Photofragmentation of CH_3Br on $Br/Ni(111)$: Cross section and competive processes*, Phys. Rev. Lett. 60 (1988), pages 2551–2554.

[105] E. P. Marsh, T. L. Gilton, W. Meier, M. R. Schneider and J. P. Cowin, *Electron-transfer-medaited and direct surface photochemistry: CH_3Cl on $Ni(111)$*, Phys. Rev. Lett. 61 (1988), pages 2725–2728.

[106] F. Weik, A. de Meijere and E. Hasselbrink, *Wavelength dependence of the photochemistry of O_2 on $Pd(111)$ and the role of hot electron cascades*, J. Chem. Phys. 99 (1993), pages 682–694.

[107] D. Schwartz-Lavi, I. Bar and S. Rosenwaks, *Photodissociation of t-butyl nitrite by UV and blue photons*, Chem. Phys. Lett. 109 (1984), pages 296–300.

[108] R. B. Hall, *Pulsed-laser-induced desorption studies of the kinetics of surface reactions*, J. Phys. Chem. 91 (1988), pages 1007–1015.

[109] J. H. Bechtel, *Heating of solid targets with laser pulses*, J. Appl. Phys. 46 (1975), pages 1585–1593.

[110] D. Burgess, Jr., P. C. Stair and E. Weitz, *Calculations of the surface temperature rise and desorption temperature in laser-induced thermal desorption*, J. Vac. Sci. Techn. A 4 (1986), pages 1362–1366.

[111] D. J. Fitzmaurice and H. Frei, *Electronic adsorption of alkyl nitrite radicals in the 300-700 nm region*, Chem. Phys. Lett. 192 (1992), pages 166–172.

[112] R. A. Cox, *The photolysis of gaseous nitrous acid*, J. Photochem. 3 (1974), pages 175–188.

[113] R. A. Cox, *The photolysis of nitrous acid in the presence of carbon monoxide and sulphur dioxide*, J. Photochem. 3 (1974), pages 291–304.

Summary

This thesis deals with the surface photochemistry of physisorbed molecules. The investigation of surface photochemistry under clean and well defined conditions (i.e. in ultra high vacuum) began about one decade ago and over the last years more and more groups around the world started research in this field. Due to the increasing knowledge in surface photochemistry of diatomic molecules, the study of polyatomic molecules became possible. This triggered our interest in the photochemistry of physisorbed polyatomic molecules. The advantage of physisorbed molecules is that the electronic structure in the monolayer and multilayer are very comparable. This allows for a comparison of the photochemistry in the monolayer and ultra thin film regime and hence conclusion about the photochemical mechanism can be made. Physisorbed molecules also have the advantage that usually the gas phase photochemistry is known. This facilitates the interpretation. We have chosen a molecule, tert-butyl nitrite $(CH_3)_3CONO$, of which the photochemistry in the gas, cluster and diluted condensed phase is well documented.

Before any research could be started an ultra high vacuum (UHV) system needed to be built. This system is described in **chapter 2**. The following analytical tools are available on this apparatus: thermal desorption spectroscopy (TDS), time of flight (TOF) detection with the quadrupole mass spectrometer, X-ray photoelectron spectroscopy (XPS), Auger electron spectroscopy (AES), low energy electron diffraction (LEED) and reflection absorption infrared spectroscopy (RAIRS). Other features are: liquid nitrogen cooled sample, storage of three samples in vacuum, exchangeability of these samples under UHV conditions, large manipulator with five degrees of freedom and an exchangeable high pressure/infrared cell. The system is designed such that transportation to other photon sources is relative facile.

In **chapter 3** the adsorption of methanol on Ag(111) is investigated with TDS and XPS. This study revealed that methanol does not dissociate on Ag(111) and that in the multilayer two phases are present (an amorphous and a crystalline phase). The knowledge obtained from this study is used in chapter 5 and 6, where methanol is used as spacer layer molecule. **Chapter 4** is concerned with the adsorption behavior of tert-butyl nitrite on Ag(111). Molecular adsorption and desorption was found in agreement other studies on similar molecules. With increasing exposure first completion of the monolayer and subsequent formation of multilayers occurred. The sticking coefficient was independent of coverage.

Chapter 5 reports the surface photochemistry of tert-butyl nitrite adsorbed

on Ag(111) at 355 nm and compares it to the gas phase results. Similar to the observations in the gas phase, dissociation into a NO and tert-butoxy was found to proceed via a direct excitation mechanism. This is consistent with an excitation into the S_1 state, which is responsible for dissociation in the gas phase. In addition to these similarities with the gas phase photochemistry, also two new phenomena were observed. The NO photoproduct, which desorbs from the surface, had a bimodal velocity distribution instead of the single distribution observed in the gas phase. The bimodal distribution consists of a thermal and hyperthermal part. The thermal part is due to hyperthermal NO photoproducts that were trapped and thermalized by the silver substrate. This thermalization only occurred if the NO was formed near the substrate. The hyperthermal component had a translational temperature of 1000 K, which is lower than the expected value from gas and cluster phase data. The second phenomenon was the existence of caging for film thicknesses in excess of five layers of tert-butyl nitrite. For these thick films the top five layers still produced hyperthermal NO, but in the more inward layers caging was inhibiting dissociation. Caging did allow for a photoinduced *trans* to *cis* conversion of tert-butyl nitrite, where the *cis* form was stabilized by the cage.

The surface photochemistry of tert-butyl nitrite at 266 and 532 nm is discussed in **chapter 6**. At 266 nm the results are similar to the results at 355 nm. Irradiation also led to the formation of thermal and hyperthermal NO and caging was observed as well. The cross section for dissociation was an order of magnitude higher than at 355 nm and the translational energy of the hyperthermal component was higher as well. This is all consistent with a direct excitation into the S_2 state rather than excitation into the S_1 state. At 532 nm caging and formation of a thermal and hyperthermal NO desorption component was observed. In the ultra thin film regime caging already occurred in the layer directly below the top layer. This is clearly different from the photochemistry at 355 and 266 nm. Beside thermalization of NO photoproducts by the substrate also thermalization in the top of the film was observed. Dissociation at this wavelength was found to proceed via a direct excitation mechanism. This is in contrast to the gas phase photochemistry, where dissociation at this wavelength is believed to be absent. The small cross section at this wavelength (3×10^{-21} cm^2) could be the reason for this contrast. Additional experiments should be performed to clarify the contrast between the two fields.

Samenvatting voor iedereen

.1 Inleiding

In dit stukje wil ik zonder wetenschappelijke termen uitleggen wat ik tijdens mijn promotieonderzoek heb onderzocht. Tevens zal ik proberen een beeld te geven van de dagelijkse bezigheden en van de experimenten zelf. Omdat dit een samenvatting is, kan ik niet op de details en uitzonderingen ingaan. Wetenschappelijk gezien zijn deze details en uitzonderingen natuurlijk wel interessant. Het is namelijk even belangrijk te weten waarom iets niet gebeurt als waarom iets wel gebeurt.

In de hoofdstukken van dit proefschrift heb ik mijn onderzoek met wetenschappelijke termen in het engels beschreven, omdat je dan met één woord een heel proces of begrip kunt aanduiden. Om deze reden praten artsen ook in medische termen, zoals narcose, IVF, bronchitis, angina pectoris en paracetamol. In deze samenvatting zal ik zo min mogelijk wetenschappelijke termen gebruiken, maar zonder de begrippen molecuul en atoom kan dat moeilijk, vandaar dat ik die verderop uitgebreid zal uitleggen.

Onderzoek doen wil niet zeggen dat je continu achter de computer zit en aan knoppen draait om gegevens te verzamelen. Het grootste gedeelte van de tijd ben ik juist met andere dingen bezig geweest om er voor te zorgen dat die metingen konden worden gedaan. De eerste twee jaar bestonden voornamelijk uit het opbouwen van een groot roestvrijstalen vat met luchtpompen en veel meetinstrumenten. De meeste instrumenten zijn gekocht van fabrikanten, maar moesten nog wel op de juiste manier op het vacuümvat worden bevestigd. Vooral het op elkaar afstemmen van alle instrumenten, het testen en de problemen oplossen kost veel tijd. En als elk apparaat dan goed is aangesloten moeten ze ook nog allemaal tegelijk werken. Als er ook maar een gloeidraadje doorbrandde of er een klein lekje ontstond dan was er weer snel een week voorbij voordat het euvel gerepareerd was en het vat weer goed vacuüm was gepompt (maar daarover later wat meer).

Het AMOLF instituut waar ik heb gewerkt (AMOLF staat voor Atoom en MOLecuul Fysica, fysica is een ander woord voor natuurkunde) is onderdeel van de FOM. FOM is een stichting voor Fundamenteel Onderzoek der Materie en zoals de eerste letter van FOM al zegt gaat het om fundamenteel onderzoek. Men doet onderzoek niet om een beter apparaat te maken of om een nieuw proces te ontwikkelen, maar om te onderzoeken waarom bepaalde dingen gebeuren zoals ze

gebeuren. Met die kennis van het waarom kunnen anderen dan nieuwe apparaten en processen ontwikkelen.

Voordat ik op mijn onderzoek in ga, zal ik eerst vertellen wat een molecuul en een atoom is. Als een zuivere stof zoals water, terpentine, aardgas (methaan) of suiker wordt gedeeld in twee delen, dan is elk deel nog steeds dezelfde stof. Als je nu door gaat met delen totdat verder delen niet meer twee delen van dezelfde stof oplevert, dan wordt dat kleinste deel een molecuul genoemd. Zo'n molecuul is erg klein, want er zijn ongeveer een miljoen moleculen nodig om een rij te maken van een millimeter lang. Voor een klein molecuul zoals water zijn er zelfs een paar miljoen nodig en voor een wat groter molecuul zoals suiker wat minder dan een miljoen. Een miljoen lijkt misschien nog niet zoveel maar als men realiseert hoeveel suikermoleculen er in een enkel suikerkorreltje zitten, dan pas wordt duidelijk hoe klein een molecuul is. Als de moleculen in een suikerkorrel geteld konden worden en een persoon zou er honderd per seconde kunnen tellen, dan heeft hij net zoveel tijd nodig als de aarde oud is (ongeveer 5 miljard jaar) om alle moleculen in dat ene korreltje te tellen.

Een zuivere stof is dus opgebouwd uit ontelbaar veel identieke deeltjes die moleculen worden genoemd. Een molecuul zelf is weer opgebouwd uit atomen. Van moleculen zijn er ontelbaar veel soorten, maar van atomen zijn er maar iets meer dan honderd soorten. De atomen worden vaak voorgesteld als bolletjes waarvan de grootte de soort bepaald. Zo bestaat een water molecuul uit twee waterstof atomen en één zuurstof atoom. Rietsuiker bestaat uit 12 koolstof atomen, 22 waterstof atomen en 11 zuurstof atomen. Niet alleen het aantal en de soorten atomen bepalen het molecuul maar ook de manier waarop de atomen gerangschikt zijn bepalen wat voor soort molecuul het is. In figuur I is als voorbeeld een watermolecuul en een rietsuikermolecuul getekend. Duidelijk is te zien hoe de moleculen uit de verschillende atomen zijn opgebouwd.

Door de atomen anders te rangschikken of door een molecuul te splitsen wordt een ander molecuul verkregen en dus ook een ander stof. Het omvormen van een molecuul in de andere heet een chemische reactie. Dit omvormen vindt soms vanzelf plaats (roesten van ijzer), soms moet het alleen opgang worden gebracht (bijvoorbeeld door het aansteken van een kaars) en soms moet het blijvend geholpen worden (stollen van een ei door koken). Reacties die niet vanzelf lopen, moeten dus geholpen worden. Vaak gebeurt dit door verwarmen. Een andere manier is het gebruik van metaaloppervlakken. Vaak blijkt dat een reactie veel beter aan een metaaloppervlak verloopt. Door de juiste keuze van het metaal kan een reactie schoner, sneller en dus goedkoper plaats vinden. Ook kan de reactie een bepaalde kant worden opgestuurd, dat wil zeggen dat uit verschillende mogelijke reacties er maar één plaats vindt. Om deze redenen worden voor veel reacties metaaloppervlakken gebruikt. Die metaaloppervlakken worden verkregen door heel veel, hele kleine metaalbolletjes in een poreus materiaal aan te brengen. Het poreuze materiaal wordt dan alleen als drager gebruikt en het geheel wordt een katalysator genoemd. Het bekende voorbeeld van een katalysator is natuurlijk de autokatalysator waarin twee verschillende soorten metaaldeeltjes de schadelijke uitlaatgassen in veel minder schadelijke gassen omzetten. Maar
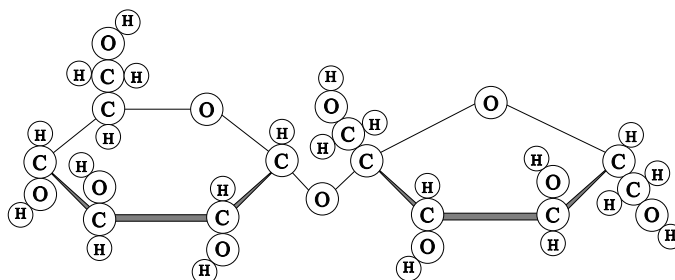
Rietsuiker

Water

Figure I: *Voorbeeld van een water- en een rietsuikermolecuul. Duidelijk is te zien hoe een molecuul opgebouwd is uit bolvormige atomen. Water is klein molecuul en rietsuiker is duidelijk groter. Een bolletje met een C is een koolstof atoom, H is een waterstof atoom en O is een zuurstof atoom. Op sommige plaatsen in de rietsuiker molecuul zijn stokjes getekend om wat ruimte te scheppen, zodat het geheel wat duidelijker is. In werkelijkheid is die ruimte er niet.*

ook in de chemische industrie worden veel katalysatoren gebruikt. Brandspiritus wordt met een katalysator gemaakt en waspoeder bestaat voor een groot deel uit katalysator (zeoliet).

Behalve warmte en metaaloppervlakken kan ook licht een reactie in gang zetten. Voorbeelden van reacties door licht zijn het uitbleken van kleuren, bruin worden van de huid, maar ook de afbraak van ozon op grote hoogte in de atmosfeer (20-50 km hoog) en het ontstaan van smog op lage hoogte. Het groeien van planten wordt ook door licht geactiveerd. Er is al veel bekend hoe licht een reactie in gang zet voor gassen. Op veel plaatsen in de wereld wordt en is dit in detail onderzocht. Over de combinatie van licht en metaaloppervlakken is veel minder bekend. Voor kleine moleculen is al het een en ander onderzocht, maar over de verschijnselen die optreden bij door licht geactiveerde reacties van grote moleculen aan metaaloppervlakken was nog niet veel bekend. Mijn onderzoek, dat beschreven is in dit proefschrift, gaat over dit onderwerp. Met dit onderzoek hoop ik bij te dragen aan het begrijpen van door licht geactiveerde reacties aan oppervlakken, zodat door licht geactiveerde processen in de natuur verklaard kunnen worden of dat deze processen toegepast kunnen worden. Een toepassing

ligt bijvoorbeeld in de chipindustrie. Hier wordt licht gebruikt om hele kleine draadjes en transistors op een chip te schrijven. Door nog meer gebruik te maken van door licht geactiveerde reacties, kan misschien de chip nog kleiner en sneller gemaakt worden.

.2   Het onderzoek

Door het gebruik van warmte, licht en metaaloppervlakken kunnen chemische reacties sneller plaats vinden en kan een reactie gestuurd worden. Door een combinatie deze drie is in principe nog meer mogelijk. Maar voordat deze combinatie kan worden benut, zal eerst onderzocht moeten worden of en waarom een door licht geactiveerd reactie plaats heeft aan een metaaloppervlak. Uit eerder onderzoek was bekend dat kleine moleculen op metaaloppervlakken reacties vertonen als ze met licht worden beschenen. Voor enkele grotere moleculen waren ook al experimenten gedaan maar een algemeen beeld was er nog niet. Dit was de reden dat wij en enkele andere onderzoeksgroepen in de wereld onderzoeken begonnen naar de fotochemie (reacties door licht) van grotere moleculen op een metaaloppervlak. Het verschil met de kleine moleculen is dat grote moleculen veel meer verschillende reacties kunnen vertonen, wat het onderzoek compliceert. Ook "plakken" kleine moleculen anders aan een metaaloppervlak dan grote moleculen. Kleine moleculen "plakken" meestal wel aan het metaal maar moeilijker aan elkaar, waardoor er maar één laag moleculen op het metaal zit. Voor grote moleculen ligt dit anders. Als grote moleculen aan het metaal kleven dan kleven ze meestal ook aan elkaar, daarom zitten er meestal ook meerder lagen moleculen op het metaal. En omdat elke laag op een andere afstand van het metaaloppervlak zit, kan elke laag andere verschijnselen vertonen. Dit maakt het onderzoek complexer, maar daardoor kom je ook meer te weten. In figuur II is het verschil tussen grote en kleine moleculen op een metaaloppervlak getekend. Wat het onderzoek van grote moleculen op metaaloppervlakken iets makkelijker maakt is dat de door licht geactiveerde reacties van die moleculen als gas vaak wel onderzocht zijn. Door overeenkomsten in de resultaten kunnen ook conclusies getrokken worden zonder dat uitgebreide experimenten nodig zijn.

Als metaaloppervlak is in mijn onderzoek een zilveren schijfje gebruikt zo groot als een dik dubbeltje (1 cm doorsnede en 3 mm dik). Omdat tijdens de experimenten het oppervlak niet met andere moleculen bevuild mocht worden, zijn alle experimenten in vacuüm gedaan. Dit vacuüm is zo goed dat het ultra hoog vacuüm wordt genoemd. Dit vacuüm is triljoen (een één met twaalf nullen) keer beter dan het vacuüm in een pak koffie en nog is het maar net goed genoeg voor mijn onderzoek. Het duurt daarom ook enkele dagen voordat het gehele vacuümvat tot die lage druk is afgepompt. Het vacuümvat is iets meer dan een meter groot en het hele apparaat met elektronica is bijna vier meter lang. Dit apparaat staat beschreven in **hoofdstuk 2**. Door het zilver te koelen met vloeibaar stikstof (-196° C) en een heel klein beetje gas van het te onderzoeken molecuul in het vacuümsysteem te laten, vriest het molecuul goed vast aan het zilver. Met
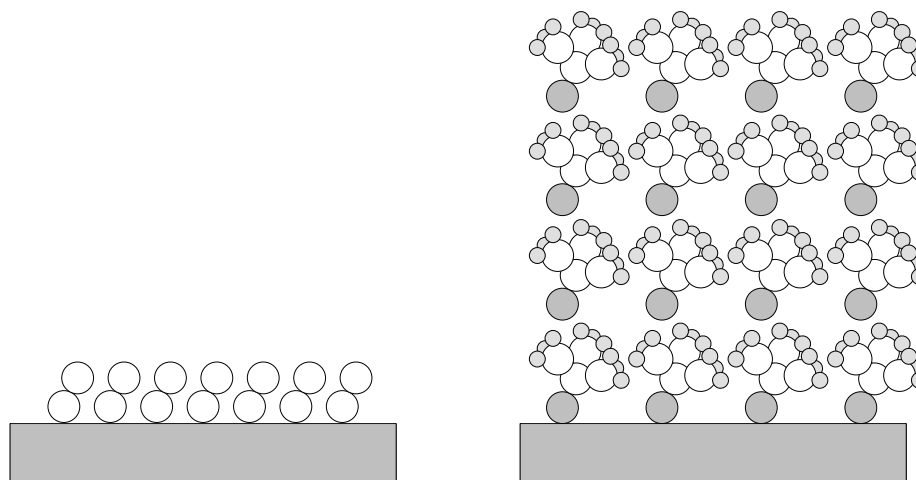
Figure II: *Links is getekend hoe kleine moleculen in het algemeen aan opper-
vlak zitten en rechts is dit voor een groot molecuul gedaan. Kleine moleculen
vormen vaak maar een laag, terwijl een groot molecuul makkelijk meerdere
lagen vormt. Door deze meerdere lagen kan een molecuul boven in een laag
oftewel ver van het metaal zich anders gedragen dan een molecuul onder in
de laag oftewel dicht bij het oppervlak. Dit bemoeilijkt het onderzoek naar
door licht geactiveerde reacties aan grote moleculen. Tevens is te zien dat een
molecuul uit atomen is opgebouwd.*

hele gevoelige instrumenten kan nu bepaald worden hoeveel lagen moleculen er
op het zilver zitten en of er verontreinigingen in zitten. Dit onderzoek is voor
twee verschillende moleculen gedaan en beschreven in **hoofdstuk 3 en 4**. Als
alles zuiver is, dan wordt het zilver en dus ook de moleculen met laser pulsen
bestraald. Met de instrumenten op het vacuümsysteem kan dan gemeten worden
of de moleculen een reactie ondergaan en ook welke. Door metingen te doen
voor verschillende laagdikten en voor verschillende kleuren licht kun je conclusies
trekken over waar en waarom er een reactie plaats heeft (**hoofdstuk 5 en 6**).

Het molecuul dat onderzocht is heet tert-butyl nitriet. De fotochemie van dit
molecuul als gas is uitgebreid onderzocht door anderen. Uit mijn onderzoek bleek
dat de fotochemie van dit groot molecuul op een zelfde manier wordt geactiveerd
door ultra-violet (UV) licht op een zilveroppervlak als in de gasvorm. De reactie
levert dezelfde moleculen op en ook verloopt de reactie even gemakkelijk. Naast
deze overeenkomen zijn er ook verschillen, want vaak zijn er twee nieuwe pro-
cessen aanwezig. Ten eerste blijkt dat een gedeelte van de in de reactie gemaakte
moleculen veel minder heet is. Dit komt omdat een gedeelte van de door licht

gemaakte moleculen met het zilveroppervlak botsen en daardoor warmte (energie) verliezen. Dit gebeurd alleen maar in de onderste twee lagen moleculen, omdat moleculen die verder van het oppervlak uiteenvallen te ver van het oppervlak zijn om ermee te botsen. Ten tweede blijkt dat voor een dikke laag moleculen, alleen de moleculen in de bovenste vijf lagen een reactie vertonen. Dit komt doordat moleculen die zich dieper in de film bevinden omringd worden door veel andere moleculen en niet genoeg de ruimte hebben om uiteen te vallen. Dit wordt ook wel het kooi effect genoemd.

Ook is onderzocht of dit grote molecuul op een zilveroppervlak uiteenvalt als het met groen licht wordt beschenen. Van dit molecuul als gas werd gezegd dat het niet uiteen valt als het met groen licht wordt bestraald. We wilden kijken of de overeenkomsten in het ultra-violet ook in het groene gebied van het spectrum bestaan. Tot onze verbazing viel het molecuul op het zilveroppervlak wel uit elkaar als het met groen licht werd beschenen. Ook blijkt dat het mechanisme waardoor het molecuul uit elkaar valt heel veel op het mechanisme in een gas lijkt. De verklaring waarom wij zien dat een molecuul op een zilveroppervlak wel uit elkaar valt en dat dat niet gezien wordt in een gas, is waarschijnlijk dat onze instrumenten gevoeliger zijn. In een gas valt het molecuul waarschijnlijk wel uit elkaar, maar omdat het proces erg moeizaam verloopt is het moeilijk om dat te meten.

Nawoord

In het laatste gedeelte van dit proefschrift wil ik even stilstaan bij alle mensen die, op welke manier dan ook, hebben meegeholpen aan het totstandkomen van dit proefschrift. Promoveren doe je niet alleen, juist door discussies met mensen en door de hulp van anderen is het mogelijk een promotieonderzoek te doen. Daarom zou eigelijk dit nawoord op de eerste pagina horen te staan. Maar omdat na het bekijken van de omslag en de inhoudsopgave, mensen meestal meteen naar de laatste pagina's doorbladeren staat dit dankwoord toch op de goede plaats.

Als eerste wil ik mijn promotor Aart Kleyn bedanken dat hij jaren geleden mij de mogelijkheid gaf zelfstandig onderzoek te doen. Hierdoor kon ik als onderzoeker in opleiding (OIO) aan de slag op het AMOLF instituut, waar ik een zeer leerzame en plezierige tijd heb gehad. Door zijn colleges en vele discussies werd ik bekend met de oppervlakte fysica. Ook de gezamenlijke conferenties (Engeland, Japan, Amerika en Oostenrijk) waren erg plezierig. Naast wetenschapper is Aart ook een gezellige reisgenoot en gids.

Arjen Bot en Evert de Haas wil ik bedanken voor het ontwerpen van het apparaat Potvis, waar ik al mijn metingen op heb gedaan. Paul Dorlandt heeft als student mij ingewerkt en samen hebben we Potvis in elkaar gesleuteld. Malcolm Kadodwala, who worked with me as a post-doc for two years, proposed to work on tert-butyl nitrite. This choice turned out to be very successful (chapter 4,5 and 6). Unfortunately, the work on the photochemistry of methanol we performed together was less successful. After months of technical problems and hours of experiments the results turned out to be unpublishable. It was pure bad luck and one those things a Phd-student apparently has to go through. Wouter van Essenberg heeft als student de zeer succesvolle infrarood spectrometer aan het apparaat toegevoegd. Ook hebben we samen veel metingen gedaan voor hoofdstuk 4 en 5. Laurent Philippe, a post-doc during my last year, contributed to chapter 5 and 6 and refreshed my French. Merci beaucoupe pour tout cela. Craig Taatjes en Kees Bol, die kortstondig als post-docs met mij hebben samengewerkt omdat ze al snel ander werk vonden, wil ik bedanken voor de discussies van de metingen.

Na dit wetenschappelijke lijstje wil ik de technische ondersteuning bedanken voor hun hulp. Deze ondersteuning is onontbeerlijk voor een complex apparaat zoals een ultra hoog vacuüm systeem. Frans Giskes en Richard Schaafsma stonden immer klaar om technische problemen op te lossen. Frans Giskes, met wie ik twee jaar een kamer heb gedeeld, heeft mij veel tips gegeven op technisch gebied die

ik dankbaar heb toegepast bij het opknappen van mijn oude MG B en bij het afbouwen van het nieuwe huis. Verder wil ik de hele werkplaats bedanken voor het vervaardigen van vrijwel heel het apparaat. Met name Henk Neerings en Wim Barsinghorn, die veelvuldig "haastklusjes" voor mij hebben opgeknapt, ben ik erg dankbaar. De afdeling Elektronica en Informatica, met in het bijzonder Hans Alberda, Idsard Attema, Henk Dekker en Hans ter Horst, hebben ook menig onderdeel van het apparaat gezien of gemaakt. René Koper heeft altijd mooie gepolijste kristallen afgeleverd waarop het goed experimenteren was.

Natuurlijk wil ik ook verschillende mensen bedanken dat ze er voor gezorgd hebben dat ik een plezierige tijd heb gehad op het AMOLF. Wim Koppers, Age Raukema en Laurent Philippe waren gezellige kamergenoten. Anderen, zoals Bart Berenbak, Michael Gleeson, Eric Kirchner, Rob Lahaye, Bert van Lierop, René Maatman, Dimitros Papageorgopoulos, Bernd Riedmüller, Gerard van Rooij, Udo van Slooten, Katsuyoshi Tsumori en Arjan Wiskerke zorgden altijd voor een geanimeerde lunch of een gezellig kopje koffie of thee. Bij de receptie zorgden Trees, Els, Magda en Marian vaak voor een vriendelijk goede morgen of een geïnteresseerd gesprek tijdens het faxen.

Mijn ouders en schoonouders wil ik bedanken dat ze mij gestimuleerd hebben tijdens mijn studie en promotieonderzoek. Mijn vrouw Natasha ben ik heel dankbaar. Hoewel ze zelf vaak heeft gezegd dat ze zelf geen onderzoek zou kunnen doen vanwege de onontkoombare tegenslagen en problemen, was ze altijd een grote steun en een luisterend oor. Ik hoop dat de toekomst minder woelig zal zijn en dat we samen met onze baby veel plezier zullen hebben.